Università degli Studi di Catania

Dipartimento di Fisica e Astronomia

Dottorato di Ricerca in Fisica - XXIII Ciclo

AN OBSERVATIONAL AND THEORETICAL STUDY OF THE MAGNETIC HELICITY FLUX

Author
Aimilia Smyrli

Coordinator:

Prof. Francesco Riggi

Supervisors:

Prof. Francesca Zuccarello

Dr. Duncan Mackay

Co-supervisor:

Dr. Daniele Spadaro

ANNO ACCADEMICO 2009-2010

To my grandfather

Abstract

The study of magnetic helicity started in 1969 when Moffatt (Moffatt 1969) emphasized the necessity of introducing an invariant into Euler's equations, that can provide a bridge between topology and fluid dynamics. This quantity was determined to be magnetic helicity, that can measure the complex geometry and the mixing properties of a magnetic field such as *the twist, braiding or linkage of the field lines* during different phases of its evolution.

Not surprisingly, the solar physicists community is attracted by this physical parameter, that amongst others has the remarkable property to remain *approximately* conserved in a perfectly conducting plasma (with high magnetic Reynolds number, as proposed by Taylor (1974) or Berger & Field (1984)). For example, the conservation of magnetic helicity in the solar convective zone can provide significant information on the alpha effect in solar dynamo theory. Nevertheless, what is actually interesting is that helicity may be used to understand dynamic processes such as Coronal Mass Ejections (CMEs), flares and filament eruption, that lead to the large amounts of energy release and so avoid an endless storage of magnetic helicity in the solar corona. Hence, the observational study of magnetic helicity has received considerable attention since it carries information about the structure of the magnetic field configuration and the conditions under which this structure can lead to an instability that acts as a precursor for an eruptive event.

In this thesis, magnetic helicity is investigated both observationally and theoretically.

In the first Chapter we introduce some important concepts used in our investigations, such as the basic characteristics of CME events and the magnetic helicity definition and its application to solar phenomena.

In the second Chapter, we present our observational studies aimed at investigating the relationship between the evolution of magnetic helicity in active regions and the occurrence of halo CMEs. This is a first step aimed at providing a solution to some hotly debated questions related to CMEs, such as **"Which, when, how and why?"** an active region can reach the configuration necessary to trigger the explosion of a CME. Initially, we focus on identifying the active regions (ARs) that are suspected to be probable CME initiation sites. This is achieved by making use of sequential full-disk solar images from the Extreme Ultraviolet Imaging Telescope (EIT) onboard the space-borne Solar and Heliospheric Observatory (SOHO) and by computing the difference between successive images in all the wavelengths, with the pivot image the one being closest to the occurrence of the CME. An important difference in brightness together with the indication of a flare or a filament eruption allows us to select the AR where the CME was initiated.

In this way we limit our analysis to 10 ARs. The only chance to investigate the evolution of magnetic helicity, can be provided by the analysis of magnetic fields. Thus, we work with data obtained from the Michelson Doppler Imager (MDI) magnetograph onboard the SOHO satellite. The Local Correlation Tracking (LCT) method is applied in order to obtain the horizontal velocities and a Fast Fourier Transform (FFT) method is used in order to get the vector potential.

We find that the magnetic helicity injection does not have a unique trend in the events analyzed: in 40 % of the cases it shows a large sudden and abrupt change that is temporally correlated with a CME occurrence, while in the other cases it shows a steady monotonic trend, with a slight change in magnetic helicity at CME occurrence (Smyrli et al., 2010).

However, a key result concerns the active regions where both X-class flares and CMEs occur. In these cases major changes in the magnetic helicity flux take place prior to the CME detection and are connected to an increase in the magnetic flux. This means that the emergence of magnetic flux from subphotospheric layers can change significantly the active region magnetic configuration, by shearing or twisting, and so trigger instabilities that will eventually lead to eruptive events. **Consequently, the study of the motion of magnetic concentrations occurring in the convective supergranular cells, their**

influence on the build-up of magnetic helicity and their coupling to coronal eruptions, inspired our theoretical work.

In the third Chapter, we consider the small scale build up of magnetic helicity in a convective supergranular cell. We study the motion of magnetic features (bipoles) in a convective cell that is simplified into the form of a hexagonal cell, with a diameter of ~ 40 arcsec, or $\sim 30,000$ km. As a first step, we work with one bipole and then with more to a maximum number of five. Different processes are studied between polarities of opposite sign such as cancellation, emergence, advection ('fly-by'), coalescence or fragmentation, depending on the initial tilt angle of the inserted bipole. In order to study the effects of different magnetic fragment motions in the supergranular cell into the magnetic helicity accumulation, we apply the same code that we have already used in the Chapter 2 for the observational data analysis.

Our results show that a short distance between magnetic fragments, and thus strong relative motions, can be a key element in the accumulation of large amounts of magnetic helicity. This can be the case of new emergence of new polarities or the case where two polarities are passing by each other ("fly-by"), but without any interaction. More importantly, we notice the highest production of magnetic helicity in neighboring borders of the supergranular cell, something that can indicate the occurrence of eruptive events in the corona above these "junction" points. In contrast, when no shearing is observed, i.e when the initial tilt angle is $\pm 90°$, the accumulated helicity is very small.

The results obtained in this research, using both the observational and the theoretical approach, motivate future investigations that are briefly described in the last Chapter.

Contents

List of Figures

Chapter 1

Introduction

"Always keep Ithaca in your mind.
To arrive there is your ultimate goal..."
Konstantinos P. Kavafis, **"Ithaca"** (1911)

The actual heart of the solar system that sustains the necessary energy for the existence of life on Earth is the Sun. Thus, is not surprising that the study of our closest star has attracted the interest of hundreds of scientists. Moreover, the Sun is interesting as an astrophysical laboratory and since it is the nearest star and can be studied in much greater detail than others, we can use the obtained information to explain many astrophysical processes that occur in other stars, or planets or in general in the Universe.

The Sun is classified as a $G2\ V$ star. The mass of the Sun is composed of about 70% hydrogen, 28% helium and the rest of other heavier elements (such as oxygen, carbon, neon, magnesium etc.). It has a mass of 1.99×10^{30} kg, luminosity 3.85×10^{26} W, and radius 6.96×10^{8} m. The Sun and its extended atmosphere can be divided in a number of layers, as shown in Figure 1.1, according to the physical processes that are responsible for the generation and transport of energy in each region. The solar interior whose main characteristics have been confirmed by **helioseismology** can be divided as follows:

- **The Core** is the central region in the solar interior that covers $\sim 20 - 25\%$ of the solar radius. Here, thermo-nuclear reactions take place from which the solar energy

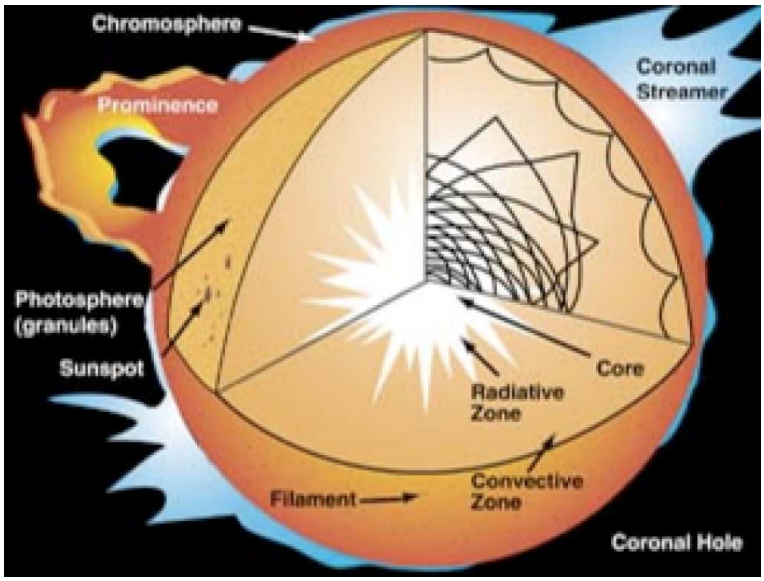

Figure 1.1: *Schematic drawing of the structure of the Sun illustrating the different internal and atmospheric layers.Image courtesy from McREL (http : //genesismission.jpl.nasa.gov/science/mod3$_S$unlightSolarHeat/SolarStructure/index.html).*

flux is generated

- **The Radiative Zone** covers the region between 0.25 and 0.7 $R_\odot$. The transfer of energy, that is generated in the core, through the radiative zone can be approximated by a process of interaction between radiation and matter.
- **The Tachocline** is the thin layer between the radiative and the convective zone where the fluid flow velocities change, i.e from almost rigid to differential rotation.
- **The Convective Zone** extends from 0.7 $R_\odot$ up to the visible surface. Convective motions transfer heat rapidly to the surface

The dividing layer between the solar interior and the solar atmosphere is the **photosphere**, the visible surface. Above the photosphere lies the solar atmosphere that consists of **the chromosphere, the transition region, the corona and the heliosphere**.

In this thesis we focus on processes that take place both in the solar interior (more specifically in the convective zone) and in the solar atmosphere (more specifically dynamic

phenomena such as CMEs, flares and filament eruptions). Our aim is to understand how the interactions between fluid flows and magnetic fields can lead to complex magnetic configurations that can trigger eruptive events.

1.1 The Butterfly Diagram and the Solar Activity

In 1609 Galileo Galilei constructed the first telescope, he turned it to the Sun and charted the location and number of sunspots. Historically, the sunspot observation has provided the most important constraint of the solar activity: a continuously changing magnetic field which however shows periodicity: *Plotting the location of sunspots versus the time reveals the so-called butterfly diagram, where two latitude bands on either side of the solar equator appear and first form at mid-latitudes and then move towards the equator as each cycle evolves (see Figure 1.2).* Each cycle lasts around 11 years. Since sunspots are manifestations of strong magnetic fields (that can reach up to ± 3000 G), this cycle provides information about the solar magnetic activity. Moreover, sunspots occur in bipolar pairs consisting of a leading and a trailing spot of opposite polarity and according to **Hale's Law** the polarities are reversed in the two hemispheres and reverse in successive solar cycles. This means that every 22 years a hemisphere will be characterised by sunspot pairs of the same sign. Hence, the period of the Sun's magnetic cycle is about 22 years. Additionally, the line joining the leading and the trailing spots is inclined at an angle of $\sim 4^{\circ}$ to the equator with the leading polarity being close to the equator and the trailing one close to the poles (**Joy's Law**). For a detailed study of the solar activity see the review of Usoskin (2008) and references therein.

The 22-year activity is considered to be a manifestation of the dynamo action that takes place in the solar interior, in the tachocline. There are two main driver mechanisms for the solar dynamo :

1. **the solar differential rotation** that produces a toroidal magnetic field from an already existing poloidal field

2. **the α-effect**, a term that is used to describe the cyclonic motions that take place

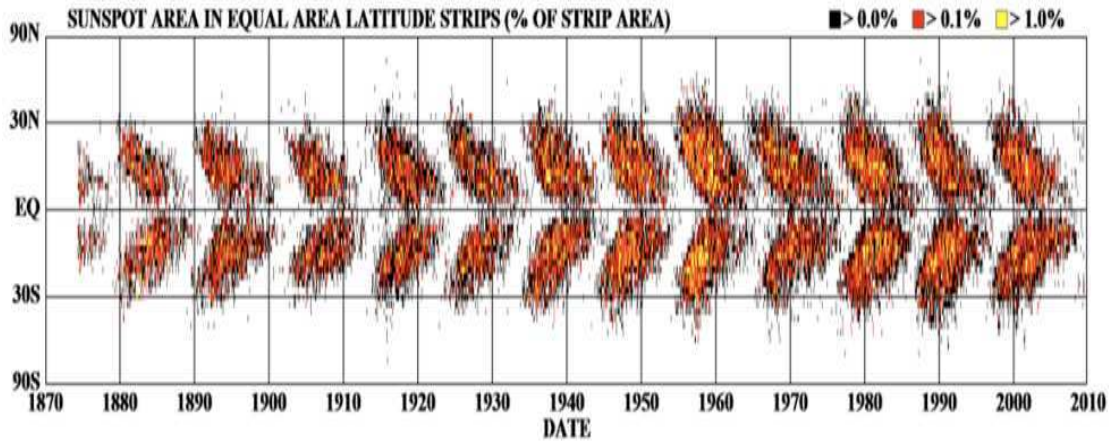

Figure 1.2: *The Sunspot Butterfly Diagram derived by the solar group at NASA Marshall Space Flight Centre.*

in the convective zone and lead to the production of a large-scale poloidal field from a mean toroidal field. The action of the Coriolis force on the convective vortices results in right-handed vortices in the Northern solar hemisphere and left-handed vortices in the South. Thus, right and left helicities in each hemisphere give rise to the conversion of a toroidal field to a poloidal.

The solar magnetic field is considered to be the source of most solar active phenomena such as the **three large-scale manifestations of the solar activity: the Coronal Mass Ejections (CMEs), the flares and the filament eruptions.**

In the following, we will describe the main characteristics of CMEs, because most of the research carried out in this thesis deals with these phenomena.

1.2 Coronal Mass Ejections

Coronal Mass Ejections (CMEs) are sudden explosions of magnetized plasma clouds from the solar atmosphere into the interplanetary medium. These violent manifestations of the solar activity are considered to be responsible for Space Weather disturbances and when directed towards the Earth, also for geomagnetic storms (as discussed for example in Koskinen & Huttunen (2006)). In that case, we have to face major damages such as the failure

(temporal or even worse, permanent) of satellites, the exposure of astronauts to radiation or the disruption of communication and navigation power systems (e.g on 13/03/1989 the city of Quebec lost half of its electrical power generation due to a large CME eruption). That is the reason why the study and prediction of CME events is considered as essential by the solar physicists community. Since the detection of the first CME on 14/12/1971 (Tousey (1973)) by the space based coronograph on board the Orbiting Solar Observatory 7 (OSO-7), million of CME events have been detected, studied and carefully analyzed.

1.2.1 Observing Techniques

CMEs are mainly observed with the help of coronographs. Coronographs observe the Thomson-scattered light by electrons and so CMEs appear as two-dimensional white-light features projected on the plane of the sky. Nevertheless, we know that most of the production and development of a CME takes place lower in the corona, below the occulting disk of a coronograph. Observations in different wavelenghts have revealed the coronal restructuring that underlies a CME event and various phenomena that can be connected to them, i.e. the coronal or EUV dimmings (Sterling & Hudson (1997)), soft X-ray sigmoid structures (Canfield et al. (1999)), EIT waves (Thompson et al. (1998)), filaments observed in H_a, or type II radio bursts (Wild & McCready (1950)) that reveal MHD shock waves propagating away from coronal disturbances such as CMEs and flares. In Figure 1.3 we present the eruptive event of 12/05/1997 where a CME, a flare, dimming and associated EIT wave where observed (the event is presented in Attrill et al. (2006)).

1.2.2 CME basic characteristic properties

The basic features of the CMEs that have been obtained through statistical studies of various datasets can be summarized as follows:

* **Morphology.** Traditionally, observers with the help of coronograph white-light images have defined a CME as a three-part structure that consists of a **bright front loop** overlying a **coronal dark cavity** that includes a **bright core** comprising prominence material (as was firstly detected in the prototypical CME event of

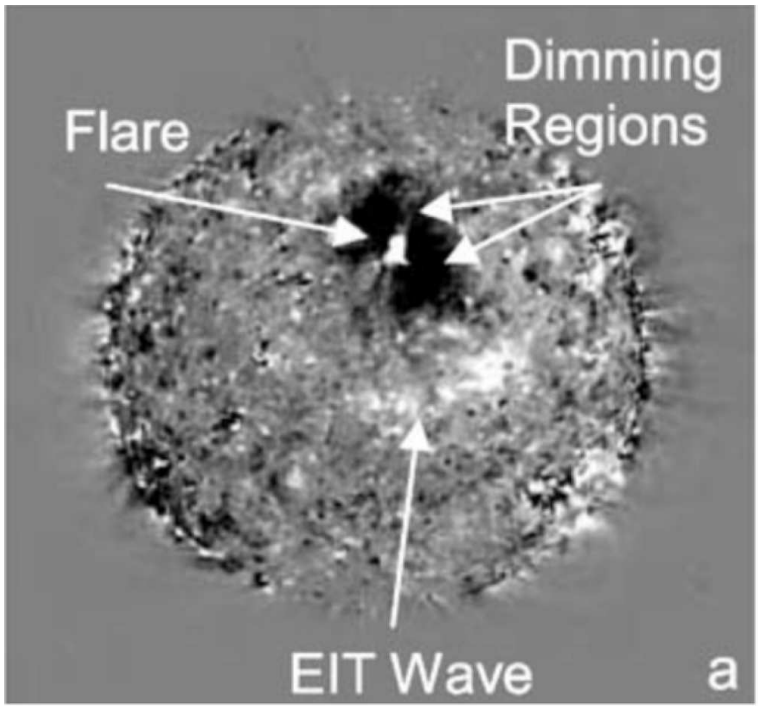

Figure 1.3: *a) An EIT difference image showning the flare site, twin dimming regions and a propagating wave. The event was examined by Attrill et al. (2006) and the image is taken from van Driel-Gesztelyi & Culhane (2009).*

18/08/1980 by Illing & Hundhausen (1985)) . Figure 1.4 shows an example of the three-part morphology of a CME as presented in Riley et al. (2008). Within the dark cavity there is a helical magnetic field structure that is connected to the presence of an expanding flux rope (as suggested for example from Cremades & Bothmer (2004) and Krall (2007) and was confirmed by stereoscopic observations from Thernisien et al. (2009) or Wood & Howard (2009)). The outermost bright leading edge is a dense plasma shell that is regarded as the material that has been swept up by the erupting flux rope and interacted with the ambient coronal plasma, i.e it is considered to be a shock driven by the flux rope ahead of the CME.

Since the inner bright core is observed to be emitting in the H_a line, it is composed of much cooler plasma which is assumed to originate from a prominence eruption that occurred below the field of view of the coronograph.

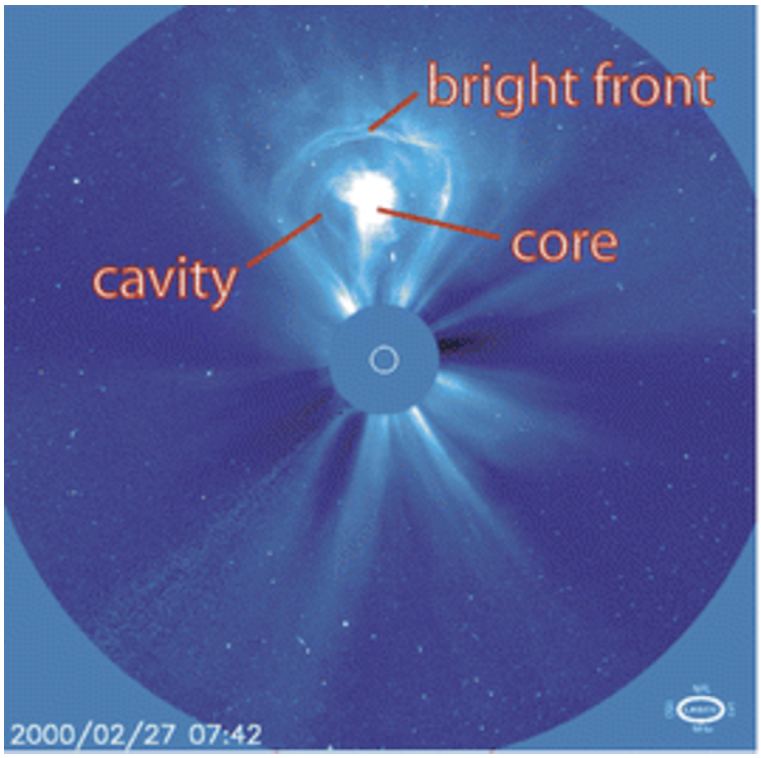

Figure 1.4: *Three-part structure of a CME: bright leading edge, dark cavity and a bright central region that is called the core. The event was observed by LASCO on 27/02/200 at 07:42UT and is presented in Riley et al. (2008).*

* **Occurrence Rate.** During the solar maximum we can observe daily around six (or even more) CMEs, whereas during the solar minimum the number of observed CMEs falls down to $0.5/day$. Gopalswamy et al. (2003a) have studied the 23rd solar cycle and discovered individual cases where more than a dozen CMEs occurred in a day.

* **Position Angle- Latitude Distribution.** The projected angular centroid of a CME defines its apparent latitude and is strongly connected to the CME source region(Hundhausen (1993)). During the solar minimum the CMEs cluster at low latitudes ($\pm 10^{\circ}$ around the equator), whereas during the solar maximum they appear at all latitudes(St. Cyr et al. (2000); Gopalswamy (2003)). However, we should note that there is no equatorward drift observed at low latitudes (Li et al. (2009)), and that the apparent latitudes of CMEs are more connected with the latitudes of helmet

streamers (St. Cyr et al. (2000)) than with the latitudes of active regions that the butterfly diagram reveals.

* **Angular Width** The angular width of a CME is measured as the position angle extent in the plane of the sky. According to their angular size the CMEs can be grouped in four classes (following the work presented by Mishra & Tripathi (2006) and Howard et al. (1982)) :

  - narrow CMEs with an angular width smaller than 20°.
  - normal CMEs with angular width in the range between 20° and 120°.
  - wide CMEs with angular width higher than 120°.
  - partial halo CMEs with 120° $\leq$ angular width *leq* 360°.
  - halo CMEs with angular size equal to 360°. We note that there can be different definitions of halo CMEs: for example Kim et al. (2005) defined as halo CMEs the events with angular width larger than 120°.

    Halo CMEs are interpreted as the result of the Thompson scattering of Sun's white light along the line-of-sight caused by a wide bubble (i.e shell) of dense plasma that is ejected in the frontside or backside of the Sun (Howard et al. (1982)). Halo CMEs are considered to be more geoeffective (i.e able to cause geomagnetic storms with intensity $\leq$ -50 nT) than the other CME events (studies carried out on this topic can be found for example in Zhao & Webb (2003) and Gopalswamy et al. (2007))

As far as the solar cycle dependence is concerned, it has been detected an increase in the percentage of narrow and normal CMEs during the solar maximum(Mishra & Tripathi (2006)), and a decrease in the percentage of wide CMEs during the minimum phases of the solar cycle(St. Cyr et al. (2000)). It is possible that the angular width is subject to projection effect errors and for CMEs that are away from the solar limb, is overestimated. Interestingly, Moore et al. (2007) studied three CMEs originating from flare regions and showed that the final angular width that a CME has in the

outer corona can be directly connected to the average magnetic field strength and to the angular width of the flaring source region.

* **Speed** The speed of CMEs is defined by tracking their coronographig images in the plane of sky and so even in this case errors due to projection effects can occur. The speed of a CME can change within the coronographic field of view because it can be subject to propelling and retarding forces. CME speeds range from less than 20 km/s up to 3000 km/s. Halo CMEs are more energetic, their average speed is around 1000 km/s in comparison with the ordinary CMEs having velocities around 470 km/s. Moreover, CMEs related to active regions have higher average speeds than those connected to eruptive prominences located far from active regions (Gosling et al. (1976)).

* **Acceleration** The CME acceleration within the coronographic field of view is speed-dependent. Yashiro et al. (2004) found that the majority of the slow CMEs (i.e with velocities $\leq$ 250 km/s) show acceleration, indicating a continuous energy release, whereas the fast ones (with a speed higher than 900 km/s) show deceleration. Moreover, CMEs that are moving at the solar wind speed show little acceleration. MacQueen & Fisher (1983) showed that CME events that are associated to flares have more rapid accelerations. On this basis, in Chapter 2 we will divide our sample of CME events into two categories : gradual and impulsive.

* **Mass** During a CME event between 10^{12}g and 10^{16}g of coronal material is ejected. This mass is estimated from coronographic images taking into account the excess of brightness of a CME image relative to an image taken before the event. Hence, the mass that the occulting disk is covering cannot be included and the CME masses are in general underestimated due to the assumption that all of the CME material is located in the plane of the sky (Vourlidas et al. (2000)). The kinetic energy of a CME can be determined through the obtained masses and speeds and is between 10^{27} erg and 10^{33} erg. Vourlidas et al. (2002) proposed a power-law distribution to describe the masses and the kinetic energies of CMEs, in contrast with Jackson &

Howard (1993), who presented an exponential distribution.

1.2.3 CME Theoretical Models

Even though many of the properties of the CMEs are well known, their initiation remains still an unresolved problem (Forbes et al. (2006)). On the one hand, the current observations do not always provide us information about the magnetic field configuration in the low corona, where the initial stages of the CME evolution occur. On the other hand, even though there is a variety of theoretical models that have been developed to explain the triggering mechanism and observed properties of CMEs, surprisingly, it has not yet been developed a single model that can describe all of the observational data and observed processes (in the lower levels of the atmosphere or in the solar wind) related even to a single CME event.

In the breakout model (Antiochos et al. (1999)) a quadrupolar flux distribution is considered consisting of an overlying arcade whose flux is oppositely directed with respect to the underlying central arcade and two lateral flux systems. In this scenario the emergence of new magnetic flux (Zuccarello et al. (2008)) and/or the shearing motions along the magnetic inversion line eventually result in a CME. Priest & Forbes (1990) and Forbes & Priest (1995) showed that within a bipolar topology, converging motions can result in the loss of equilibrium of a magnetic flux-rope leading to a catastrophic eruption. Chen & Shibata (2000) showed that the injection of new magnetic flux from below the photosphere can be responsible for the eruption of a pre-existing flux-rope. More recent MHD simulations of the emergence of a twisted flux tube have been carried out by Archontis & Török (2008). These authors found that a flux rope is formed within the expanding field due to shearing and reconnection of field lines at low atmospheric heights. Depending on if the corona is magnetized or not, the expanding flux rope experiences a full eruption or remains confined.

1.2.4 Mini-CMEs

CMEs may also occur in the Quiet Sun. In that case many of the models described above cannot be applied. Here we are dealing with the photospheric flows of the Quiet Sun and a magnetic carpet configuration that consists of small-scale randomly oriented magnetic loops whose footpoints are moving along the supergranular boundaries of convective cells. Eruptions with the characteristics of CMEs but in a much smaller scale are observed to occur at the junctions of the supergranular cells and they can be correlated with mini-filament eruption and microflare brightening or sometimes with wave-like features as observed from Extreme Ultraviolet images. For a detailed study on these events, see Innes et al. (2008), where it is estimated that around 1400 of these mini-CME events are occurring per day in the whole Sun! That is the reason why researchers consider them as events responsible for the coronal heating.

Clearly, it is necessary to combine the knowledge on how the magnetic field evolves through different layers of the Sun (starting from the convection zone up to the solar corona) with the processes that lead to CME events. A useful quantity to investigate this issue is the magnetic helicity.

1.3 Magnetic Helicity

It was firstly the need to provide a bridge between the area of fluid dynamics and the topology that has made the scientists to turn into the quantity of helicity. It has been proven that when a fluid evolves under the ideal Euler evolution, the helicity **H** shows topological invariance (e.g. Moffatt (1969); Moffatt (1978); Moffatt & Proctor (1982); Moffatt & Ricca (1992);Arnold (1974)), related to the fact that the vortex lines are frozen in the fluid.

$$\frac{\partial \omega}{\partial \mathbf{t}} = \nabla \times (\mathbf{u} \times \omega) \tag{1.1}$$

$$\mathbf{H} = \int_V (\mathbf{u} \cdot \omega)\, dV \tag{1.2}$$

where $\mathbf{u}(\mathbf{x}, \mathbf{t})$ is the velocity field of an inviscid incompressible fluid , $\omega = \nabla \times \mathbf{u}$ is the vorticity field, and V is the volume inside a closed surface S that is moving with the fluid, and so $(\mathbf{u} \cdot \mathbf{n})\, \mathbf{v} = \mathbf{0}$. This type of integral was first introduced by Gauss during his study of asteroid orbits related with the Earth's orbit.

As we can see, helicity is a pseudoscalar quantity, i.e its sign depends on the frame of reference (Moffatt & Tsinober (1992)). This property simply represents the lack of reflectional symmetry in the velocity field of a fluid, which is a necessary condition for the dynamo action and so for the existence of large scale magnetic fields in astrophysical systems (Moffatt (1976); Steenbeck & Krause (1966);Brandenburg (2009)). However, we should mention that recently, scientists are investigating the possibility of generating large scale magnetic fields without the existence of helicity (Vishniac & Brandenburg (1997)). Nevertheless, yet no strong evidence has been found to support such a possibility and helicity is a main topic in solar physics, being regarded as a tool that can describe the evolution of a magnetic field showing its complex geometry and mixing properties such as the twist, linkage and braiding of the magnetic field lines (Zeldovich (1983); Arnold (1985); Berger & Field (1986), as well as providing information on the dynamo mechanism and mainly on the α-effect (Pevtsov et al. (1995); Brandenburg (2001); Seehafer et al. (2003); Brandenburg (2005)). Magnetic helicity, $\mathbf{H_m}$, is defined similar to helicity as the integrated scalar product of the magnetic field and its vector potential and can also be considered as a topological invariant taking into account the fact that magnetic field lines are frozen in the fluid (Elsasser (1956); Woltjer (1958))

$$\mathbf{H_m} = \int_{\mathbf{V}} (\mathbf{A} \cdot\ \mathbf{B})\, \mathbf{dV} \tag{1.3}$$

where $\mathbf{A}$ is the vector potential of the magnetic field $\mathbf{B} = \nabla \times \mathbf{A}$.

Similarly, it is possible to define the current helicity as : $\mathbf{H_c} = \int_{\mathbf{V}} (\mathbf{B} \cdot\ \nabla \times \mathbf{B})\, \mathbf{dV}$ and the kinetic helicity as $\mathbf{H_c} = \int_{\mathbf{V}} (\mathbf{v} \cdot\ \nabla \times \mathbf{v})\, \mathbf{dV}$, where $\mathbf{v}$ is the velocity of the flow.

There have been many observations concerning magnetic helicity in the Sun. Reviews and relative references can be found in, for example, Chandra et al. (2010). Some important aspects of those studies is the correlation of magnetic helicity behaviour with eruptive event such as flares (Moon et al. (2002); LaBonte et al. (2007); Park et al. (2010)), filaments

(Mackay & Gaizauskas (2003), Romano et al. (2003), Romano et al. (2005), Romano et al. (2009); Jeong et al. (2009)), CMEs (Démoulin et al. (2002); Nindos et al. (2003); Phillips et al. (2005); Smyrli et al. (2010)) or Magnetic Clouds (Chandra et al. (2010). All of those cases include observational data concerning evolving magnetic features in the solar atmosphere and more interestingly are connected to a common tendency that became known as the **helicity hemispheric rule** :

Solar magnetic fields in the North Solar Hemisphere have negative helicity, in contrast to the fields in the South Hemisphere that are governed by a positive helicity. **Around 70-80% of the solar features follows this rule** (see for example Pevtsov & Balasubramaniam (2003)). In Figure 1.5 we show some characteristic patterns observed in the solar atmosphere that show positive magnetic helicity, as presented by Démoulin (2008).

When the magnetic field is closed in the integration volume (i.e it does not cross the boundary), the magnetic helicity is a gauge-invariant quantity (Berger (1999)), even though the magnetic helicity density $\mathbf{A} \cdot \mathbf{B}$ is a gauge-dependent quantity. However, when we want to study the magnetic helicity in the solar corona, we have to deal with a magnetic field that penetrates the boundaries, since magnetic flux emerges from below through the photosphere. That is the reason why Berger & Field (1984) developed the concept of relative magnetic helicity :

$$H_{rel} = \int (\mathbf{A} + \mathbf{A}_p) \cdot (\mathbf{B} - \mathbf{B}_p) dV, \tag{1.4}$$

where $\mathbf{B}$ is the magnetic field, $\mathbf{A}$ is the magnetic vector potential, $\mathbf{B}_p$ is the potential magnetic field that has the same distribution as $\mathbf{B}$ at the boundary, and finally, $\mathbf{A}_p$ is its corresponding vector potential, uniquely specified by the observed flux distribution on the surface with the equations

$$\nabla \times \mathbf{A}_p \cdot \hat{\mathbf{n}} = B_n, \qquad \nabla \cdot \mathbf{A}_p = 0, \qquad \mathbf{A}_p \cdot \hat{\mathbf{n}} = 0. \tag{1.5}$$

In Chapter 2 we calculate the helicity accumulation in a sample of active regions using the above described relative magnetic helicity.

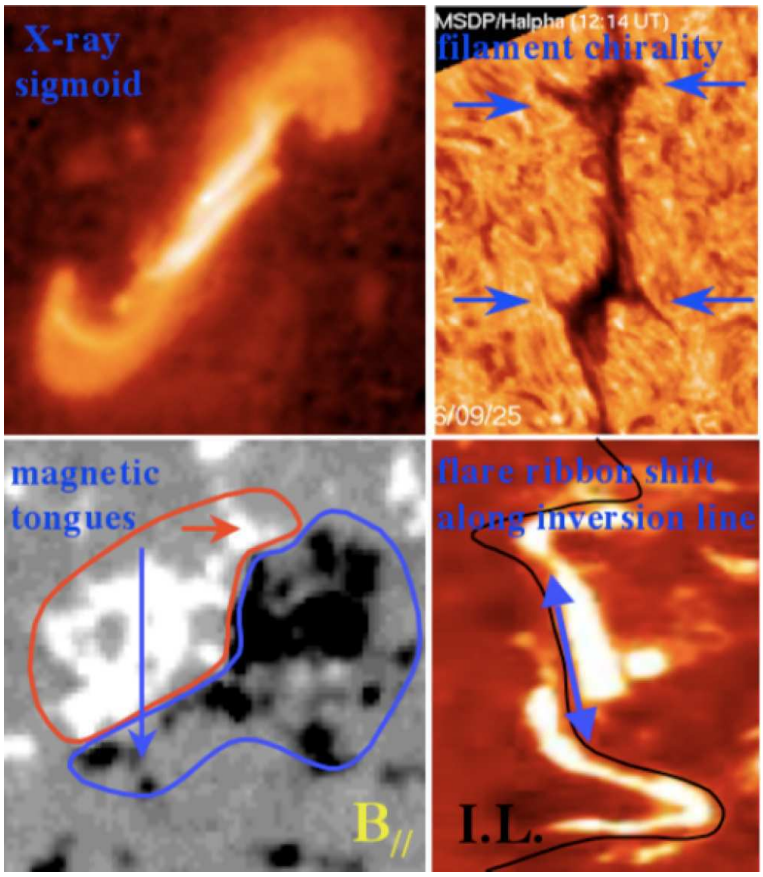

Figure 1.5: *Some characteristic features in the solar atmosphere characterized by positive helicity: X-ray sigmoids, fibrils, magnetic tongues and flare ribbons (Démoulin 2008)*

1.4 Thesis Outline

In this thesis we investigate the trend of magnetic helicity both theoretically and observationally and in different layers of the Sun. Some dynamic eruptive events observed in the corona, i.e coronal mass ejections (and more specifically halo CMEs), flares and filament eruptions for a period of two years (February 2000- June 2003) are investigated in **Chapter 2**. We use EIT/SOHO images in order to identify active regions that are possible initiation sites of CMEs. Then we use MDI/SOHO line-of-sight magnetograms that can provide us information on the photospheric magnetic field and on the velocity components of the footpoints. We then calculate the magnetic helicity injection in 10 active regions of

our sample.

The aim of the study based on observational data is to investigate the behavior of magnetic helicity accumulation in sites where the initiation of CMEs occurred, to determine whether and how changes in magnetic helicity accumulation are temporally correlated with CME occurrence. The results obtained from the sample of events analyzed indicate that major changes in magnetic helicity flux are observed in active regions characterized by emergence of new magnetic flux and/or generating halo CMEs associated with X-class flares or filament eruptions. In some of the analyzed cases the changes in magnetic helicity flux follow the CME events and can be attributed to a process of restoring a torque balance between the subphotospheric and the coronal domain of the flux tubes

In **Chapter 3** we investigate the magnetic helicity injection inside a supergranular convective cell by means of simulations. Taking into account the importance of supergranular cells in convection theories, we study the motion of magnetic features into such a geometrical element simplified as hexagonal cell and we analyse the results in terms of the accumulated magnetic helicity. We compute the emergence of a bipole inside the hexagonal cell and its motion from the centre of the cell towards its sides and its vertices, where the magnetic elements are considered to be sinking down. Multiple bipoles are also considered and phenomena such as cancellation, coalescence and fragmentation are also investigated. We find that the most important process for the accumulation of magnetic helicity is the shear motion between the polarities. Moreover, when magnetic bipoles move in neighboring boundaries, there is more interaction between their magnetic fields and thus a resultant higher complexity in the magnetic field configuration that leads to large amount of magnetic helicity. The closer two or more polarities are to each other, and the soonest in terms of computational run (i.e at the beginning and not at the end of the computation), the higher is their influence on the initial trend of magnetic helicity flux.

More research has to take place in both areas as described in **Chapter 4**. A combination of observational data for longer periods with a higher angular resolution, together with a theoretical study that includes more than one hexagonal cell, able to describe the magnetic carpet configuration, can offer another piece of information in the puzzle of

the triggering mechanisms of CMEs and in their relation to other eruptive phenomena, providing more accurate predictive models.

Chapter 2

Observational Study on Active Regions that generate Halo CMEs

"When you set out on your journey to Ithaca,
pray that the road is long,
that the summer mornings are many, when,
with such pleasure, with such joy
you will enter ports seen for the first time;
stop at Phoenician markets,
and purchase fine merchandise,..
visit many Egyptian cities,
to learn as much from scholars."
Konstantinos P. Kavafis, **"Ithaca"** (1911)

In this chapter we describe a study on the evolution of magnetic helicity in active regions (ARs) generating **halo** Coronal Mass Ejections (CMEs). This study can be considered an attempt to give a contribution to find solutions to some hotly debated questions related with CMEs, such as to identify which, when, how and why a magnetized region can provide the necessary triggering mechanisms for the occurrence of a CME, and the connection, if any, with the eruption of flares. A further motivation to carry on this research

is that eruptive events such as CMEs and flares have been proposed to be primary candidates for explaining the fact that there is not endless accumulation of magnetic helicity on the Sun (see for example Heyvaerts & Priest (1984)).

We used two types of data :

1. **EIT images.** Initially, we selected a sample of ARs that could be the most probable initiation sites, by working with EIT/SOHO images and by making the difference between successive images, with the pivot image being the closer to the time occurrence of the CME. A difference in brightness above a certain threshold together with the indication of a flare event were the fundamental information that allowed us to select the ARs.

2. **MDI images.** The parameters used in the calculation of magnetic helicity are the magnetic field, the velocity and the vector potential (see also Chapter 1). This information can be obtained using the MDI/SOHO data that provide the line-of-sight component of the magnetic field. The horizontal displacement of magnetic structures can be estimated by applying a Local Correlation Technique (LCT), (November & Simon 1988).

The results obtained demonstrate that there is not a unique behaviour which can characterize the magnetic helicity injection in the ARs generating the halo CMEs and that we can distinguish between two cases. In the first case, the magnetic helicity flux shows an abrupt change **before the CME** occurrence pointing out the important role played by magnetic flux emergence. The second case is dealing with major changes in the helicity injection rate **after the CME** and the relevant physical mechanism can be rooted in the absence of a torque balance between the subphotospheric and the coronal magnetic domain.

2.1 Motivation

Two of the most controversial topics that are frequently discussed in the solar physicists community are related with the violent manifestations of the solar activity that can be

responsible for Space Weather disturbances and, when directed towards the Earth, also for geomagnetic storms. These are namely:

I) The origin site of CMEs.

II) The relationship between CMEs and flares.

Uncovering the origin of CMEs from observational data is not an easy task. Firstly, the CMEs, that are three-dimensional structures, when observed in white-light images by coronographs (either space-based such as the Large Angle Spectrometric COronograph on board SOHO or ground-based such as the Mark IV coronographs on the High Altitude Observatory that is located on top of Mauna Loa) above the occulting disk are two-dimensional projections on the plane of the sky. Therefore, not only the values of the speed and size that describe an observed CME are underestimated (since we are "missing' one direction) but also the linkage of any CME event with the underlying magnetic feature that is responsible for its generation, is not straightforward. Only recently, with the advent of STEREO, it has become possible to obtain more realistic information on the 3-D structure and the velocity values of CMEs (Srivastava (2010); Simon et al. (2001a)). However, the problem related to the source region of the CME, is still open. Additionally, even though it is accepted that the driving mechanism of a CME is connected to the coronal magnetic field configuration and not to the gas pressure or to the force of gravity, our knowledge on the magnetic configuration that can produce highly dynamic eruptions (such as CMEs and flares) is limited. Up to now, the development of diagnostic tools of the coronal magnetic field is quite restricted and the main observational technique for measuring the magnetic field in this outer part of the solar atmosphere, is related with radio data which can provide information on the magnetic field strength but not on the full magnetic vector. Various other methods have been developed, related with the Hanle effect in EUV lines and with the Zeeman effect in the HeI 10830 Å triplet (as discussed in Trujillo Bueno (2010)), but all of them are facing difficulties in providing a completely realistic picture of the coronal field. Otherwise, extrapolations methods of the photospheric magnetic field are used as proxies for the coronal magnetic field study.

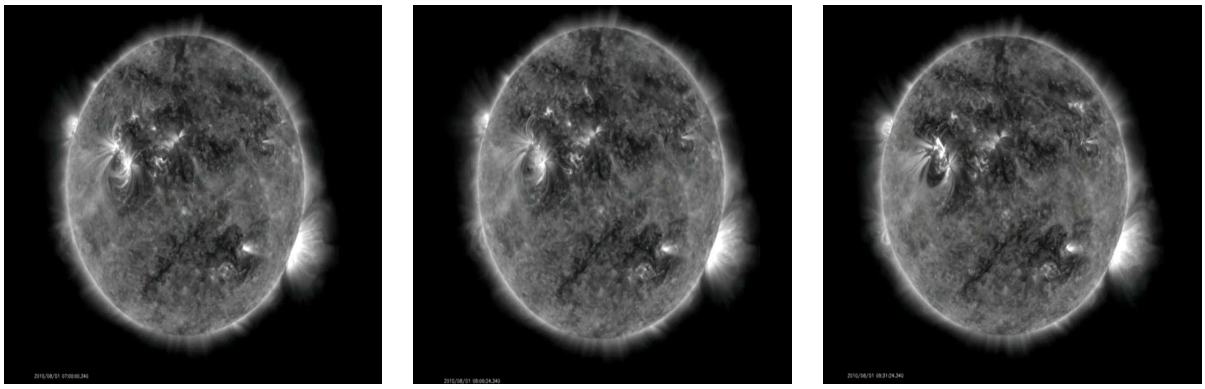

Figure 2.1: *From left to right: successive snapshots of full-disk AIA/SDO images acquired at 171 Å, obtained at 07:00 UT, 08:06 UT and 10:16 UT*: 'At approximately 08:55 UT on August 1, 2010, a C3.2 flare erupted from NOAA 1092. At nearly the same time, a filament eruption occurred, sending out a huge plasma cloud (i.e a CME) directed towards the Earth'.

Nevertheless, we also mention that our understanding of the early stages of the evolution of a dynamic CME event has improved in the last decade due to the combination of a large range of high quality data (such as those obtained by the Soft X-Ray Telescope on board Hinode, the Extreme UltraViolet Imaging Telescope on board SOHO, the Extreme Ultraviolet Imager on board the STEREO Spacecraft or the Atmospheric Imaging Assembly on board the recently launched SDO that has detected for example on 01/08/2010 a C3.2 flare accompanied by a large filament eruption, as shown in Figure 2.1) and the application of strong theoretical MHD codes (as discussed in Chapter 1).

This huge effort invested on the research on CMEs, has revealed an important aspect of their occurrence: sometimes their appearance is coincident with other dynamic events, i.e flares and filament eruptions. There is an extensive study on this topic by Khan & Hudson (2000) who showed that when a flare occurs, it can destabilize an adjacent transequatorial loop structure and thus lead to the launch of a CME. Temmer et al. (2008) have shown that there is a close relationship between the initial acceleration phase of two Halo CMEs and the impulsive phase of soft X-ray flares; Jing et al. (2004) through a statistical study,

found that 50 % of events of filament eruption are associated with the CME occurrence, whereas Gopalswamy et al. (2003b) obtained a 84 % connection between the observed filament eruptions and the CMEs; Qiu & Yurchyshyn (2005) found that the velocity of a flare- associated CME is proportional to the magnetic flux that is swept away from flare ribbons; Moon et al. (2003) found a strong connection between the kinetic energy of CME/flare limb events and the GOES X-ray peak fluxes; Chen et al. (2006) found that for CMEs that are connected to filament eruption, their velocity is roughly linearly correlated with the total magnetic flux in the filament channel.

Of course, the above mentioned studies represent just a small portion of the large literature that concerns the connection between these dynamic events, but yet a clear answer is not given.

We believe that in order to demonstrate the existence (or not) of a possible connection between solar surface phenomena such as CMEs, flares and filament eruptions, it is crucial to recognize the sequence of processes, the actual conditions and the properties of the magnetic field that characterize their early manifestations. Only when a complete knowledge of this phase will be obtained, the strong basis of a CME and flare forecasting system will be constructed.

A useful tool in this respect is the magnetic helicity. As already mentioned in Chapter 1 and in accordance with Berger & Field (1984)), magnetic helicity is one of the few global quantities that remains conserved even in resistive MHD, on a timescale much smaller than the global diffusion timescale. Nevertheless, what is actually interesting is that this conservation law can break down under the occurrence of dynamic processes such as CMEs, flares and filament eruptions, that lead to large energy releases and so avoid an endless storage of magnetic helicity in the solar corona. More specifically, when a CME occurs, it releases the magnetic energy that is stored over a large volume and leads to the partial opening of the magnetic field lines. As a result, the helicity does not remain conserved in a volume on the active region scale. Moreover, the amount of magnetic helicity that can be expelled during a CME can be estimated by the variation of coronal helicity in the active

region that generates the CME (Low (1996); Green et al. (2002); Zhang et al. (2006); van Driel-Gesztelyi et al. (2002a)).

In the recent simulations of Yeates & Mackay (2009), the authors carried out global simulations of the solar corona based on photospheric observations for a period of six months in 1999. The model included the effects of flux emergence, shearing by surface motions and cancellation along with the formation and ejection of flux ropes due to loss of equilibrium. By varying the rate at which magnetic helicity was injected, the model produced 50 % of the observed CME rate over the simulated period (see also Mackay & van Ballegooijen (2006)). In contrast to this model, Cook et al. (2009) studied the number and locations of coronal null points, a key element in the magnetic breakout model, over two solar cycles. They found that the number of nulls followed a cycle variation, peaking at maximum of 15 - 17 per rotation. The vast majority of null points were located above active latitudes and lay at low heights in the corona.

Similar studies have been carried out in order to investigate how the occurrence and intensity of a flare eruption in an active region can affect the build up of magnetic helicity in this region and the circumstances under which a CME event will be provoked. For instance, Moon et al. (2002) examined the impulsive variations that characterize the magnetic helicity when major flares associated with halo CMEs, occur. Nindos & Andrews (2004) performed a statistical study of 133 big flares of M and X class and found that in the pre-flare phase the coronal magnetic helicity of active regions producing big flares not correlated with CMEs is smaller than the coronal magnetic helicity of active regions producing CME-associated big flares. Furthermore, LaBonte et al. (2007) perfomed a survey of 393 active regions (48 X-flare producing and 345 non-X-flaring regions) and concluded that when the peak helicity flux in an active region has magnitude $> 6 \times 10^{36}$ $\mathrm{Mx^2 sec^{-1}}$ an X-class flare can take place and it will be accompanied in a few hours to few days by a CME. Work done by Hartkorn & Wang (2004) has revealed that the rapid fluctuations observed in the helicity change rate during a flare eruption, can be artifacts due to the influence of the flare emission on the spectral line during the analysis of MDI data. Thus, it is essential to focus on the long-term (i.e some days) variation of magnetic helicity in an

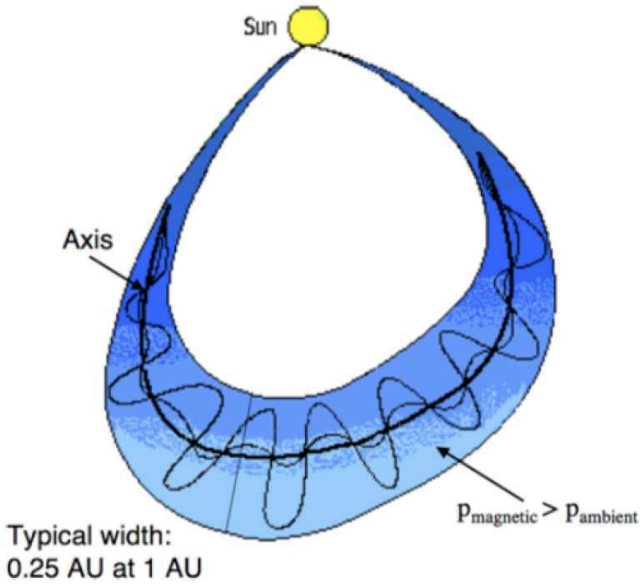

Figure 2.2: *Schematic diagram of a magnetic cloud presented in Webb et al. (2000). The cloud field configuration is that of a flux rope with helical field lines. Since magnetic helicity is a conserved quantity, we can calculate and compare its value in a magnetic cloud with the amount of helicity of an active region in the corona where a CME event occurred.*

active region in order to obtain accurate conclusions related to its connection to dynamic events, such as flares.

In many cases, a twisted flux tube ejected in a CME appears in the interplanetary space at a distance of 1 AU as a magnetic cloud (MC) in which the twisted nature remains well observable (Chen (1989); Forbes & Priest (1995); Qiu et al. 2007, Longcope et al. (2007)) and thus is expected to be characterized by a large amount of magnetic helicity. In this case the quantity of magnetic helicity and its conservation property can be used in order to connect a coronal surface event with its interplanetary counterpart: the magnetic helicity of a CME is expected to be very close to the amount obtained for the associated magnetic cloud (Mandrini et al. (2005); Luoni et al. (2005); Dasso et al. (2006)). In Figure 2.2 we present a schematic diagram of a magnetic cloud as given by Webb et al. (2000) were the helical field lines of the flux rope can be seen.

On the basis of these results it is clear that the study of the magnetic helicity evolution in active regions can provide a useful tool to gain important information about the mechanisms able to produce instabilities in the magnetic configuration. Moreover, the investigation of the magnetic helicity trend, before and after a CME occurrence, might contribute to our understanding of the role effectively played by these events in any eventual change in the magnetic helicity accumulation process (see, e.g., Nindos et al. 2003).

In this regard it is important to make a distinction between two cases. The former is related with the change in magnetic helicity prior to the CME occurrence, which should be further related with phenomena able to destabilize the coronal configuration, like new flux emergence or shearing/twisting of the magnetic field lines. The latter is related with changes in magnetic helicity occurring after the CME that, as suggested by Longcope & Welsch (2000) and Chae et al. (2003), might be due to the unbalance of torque between the sub-photospheric part of the flux rope and the coronal field which just lost some stress via the CME launch.

In this chapter we determine the evolution of both magnetic flux and magnetic helicity flux in active regions where a flare or a filament eruption occurred close in time with a halo CME in order to investigate the above mentioned scenarios. **The choice to select halo CMEs is related to the fact that these events are generally initiated in areas located in the central part of the solar disk and this aspect is quite important when an analysis of line-of-sight magnetograms (that can provide the line-of-sight component of the photospheric magnetic field) is carried out, because in this situation possible problems related to projection effects can be avoided.** We describe in Section 2.2 the selection of our sample of halo CME events and the analysis of EIT images. We first select an active region for each halo CME event accompanied by a flare or filament eruption. At a second step, we analyze the MDI magnetograms of these active regions as described in Section 1.4. The resultant magnetic helicity flux for the selected sample of active regions is given in the Section 2.4. Section 2.5 is a discussion of the significance of the results obtained. Finally, suggestions for future work are given in

Section 2.6.

2.2 Data selection and analysis of EIT images for the identification of the initiation sites of CMEs

Our aim is to study the trend of the photospheric magnetic helicity flux in active regions that generate halo CMEs.

To do this, we first selected a sample of halo CMEs from the SOHO/LASCO on-line catalog (http://cdaw.gsfc.nasa.gov/CME_list/). We decided to work with events occurred close to the maximum of the 23rd Solar Cycle (when the possibility of an eruptive event occurrence is high) and we selected a total of 38 halo CME events in the time interval 2000 February 1st - 2003 June 30. We successively compared the time inferred by a back-extrapolation in time of the CME height-time trajectory with the time of a flare or filament eruption recorded in a time interval between one hour before and one hour after the CME, using the NOAA flare catalog (http://www.solarmonitor.org/index.php), in an attempt to obtain a first association between each CME and the corresponding flare or filament eruption. We choosed this time interval because it takes approximately 2 hr for a CME to cover the distance of $2R_{\odot}$ needed to reach the LASCO C2 FOV, when traveling with a speed of 200 km/sec. This means that the reported time of the CME in the LASCO catalogue can be associated with a flare or prominence that has been detected about two hours earlier.

We used images acquired by the Extra-Ultraviolet Imaging Telescope (EIT) on board the Solar and Heliospheric Observatory (SOHO) as the primary data set to detect the active regions that were most probable connected to the occurrence of the dynamic eruptions. In Figure 2.3a we show an example of a halo CME and the associated flare observed by SOHO/EIT in Figure 2.3b. The EIT instrument (see Delaboudinière et al. 1995 for a detailed description of the instrument), a normal-incidence telescope with multilayer-coated mirrors shown in Figure 2.4, is able to image the solar transition region and the inner corona in four narrow extreme ultraviolet (EUV) channels,as shown in Figure 2.5,

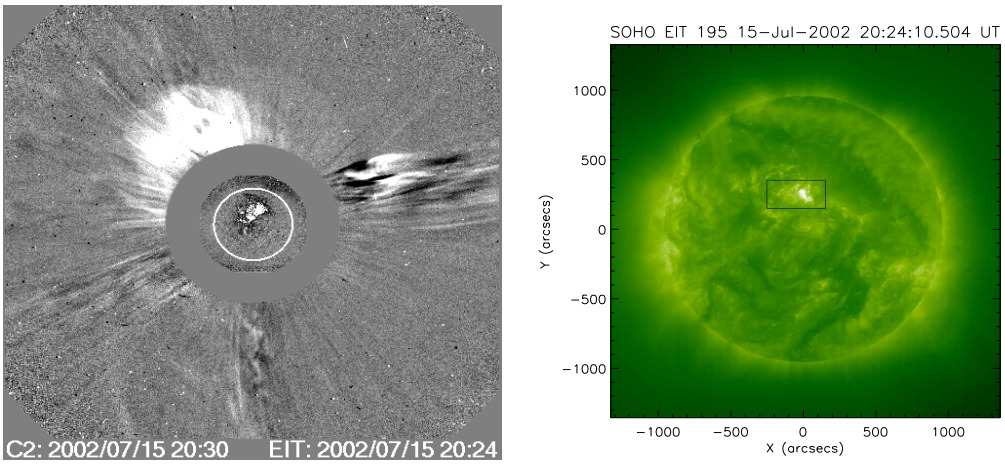

Figure 2.3: *(a) Difference image showing the halo CME observed by LASCO-C2 on 2002 july 15 at 20:30:05 UT, superposed on the EIT difference image relevant to 20:24 UT ; (b) SOHO/EIT full disk image acquired on 2002 july 15 at 20:24:10 UT, showing the location on the disk of the CME source region.*

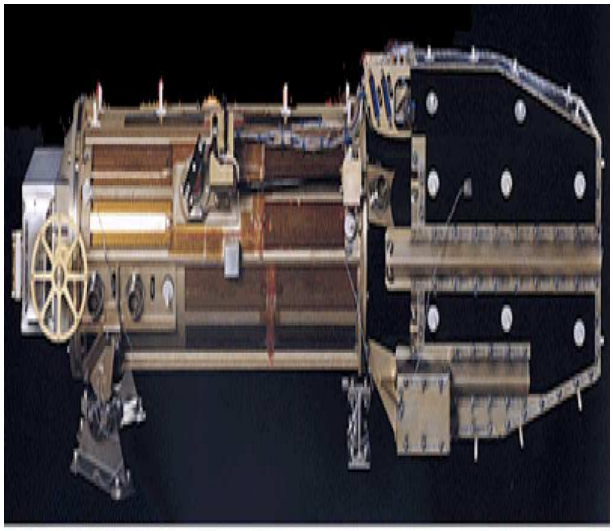

Figure 2.4: *The EIT instrument, described in detail by Delaboudinière et al. 1995*

centered at:

* 171 Å, that observe the spectral lines formed by Fe IX/X and correspond to a temperature of 1.3×10^6 K

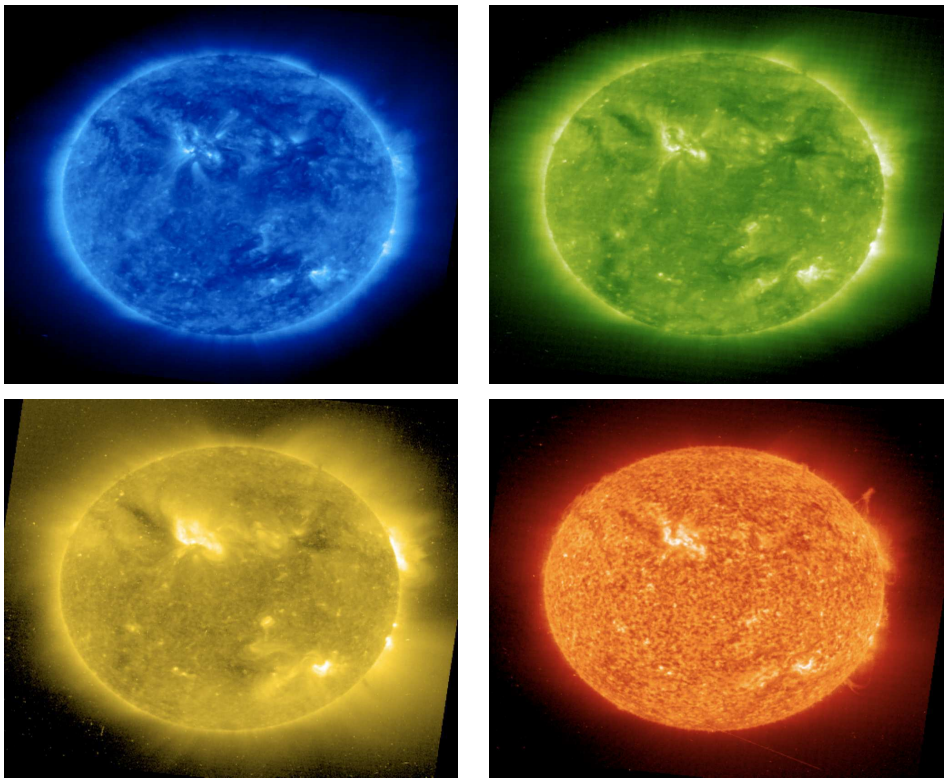

Figure 2.5: *From left to right: images of the solar disk acquired on 21/11/2010 by EIT: in the Fe IX/X line at 171 Å, in the Fe XII line at 195 Å (first row), in the Fe XV line at 284 Å and in the He II line at 304 Å (second row).*

* 195 Å, that observe the spectral lines formed by Fe XII and correspond to 1.5×10^6 K

* 284 Å, that observe the spectral lines formed by Fe XV and correspond to 2.0×10^6 K

* 304 Å, that observe the spectral lines formed by He II and correspond to $6.0-8.0 \times 10^4$ K

For each event we used the EIT full-disk images in the first three wavelengths. The field of view of the EIT instrument is 1024×1024 $pixel^2$ with a resolution of 2.6 arcsec/pixel. The procedure used to recognize the active region responsible for the halo CME initiation

images is summarized as follows:

1. Selection of EIT full-disk images corresponding to the three wavelengths: 171 Å, 284 Å and 304 Å relevant to the days of occurrence of the selected CMEs. These images are provided with 6 hr time cadence, at 01:00 UT, 07:00 UT, 13:00 UT and 19:00 UT.

2. Correction of the data for the flat field, dark current and cosmic rays. This is performed by using the standard EIT calibration procedure **EIT_PREP** in Solar Software (SSW):

   SSWIDL> $eit\_prep, index$,data =data, $outindex, outdata, /cosmic$

3. Alignment of the images using the standard SSW function *drot_map* that rotates a map (obtained from EIT data) using the solar differential rotation formula of Howard et al. (1990).

4. Selection of a pivot image. This selection corresponds to the image obtained around the time of the CME occurrence.

5. Performing difference of images between the pivot image and the images obtained 6, 12, 18 and 24 hours, respectively before and after this image. We noted that the subtraction of images at 304 Å was not really useful since we could not detect significant differences between two successive images. Therefore, we decided not to work further with this wavelength. In Figure 2.6 we show running difference images in different wavelengths for two different events of our sample.

6. Selection of a box around each active region for every difference image. In Figure 2.7 we show all the selected active regions for a 24 hr difference image at 171 Å, associated with the occurrence of a halo CME event occurred on 09/11/2002 at 13:31 UT. When the boundaries of neighboring active regions are not well-defined, the box will include both regions, so that we avoid to neglect potentially significant magnetic flux that will be later used in our calculations.

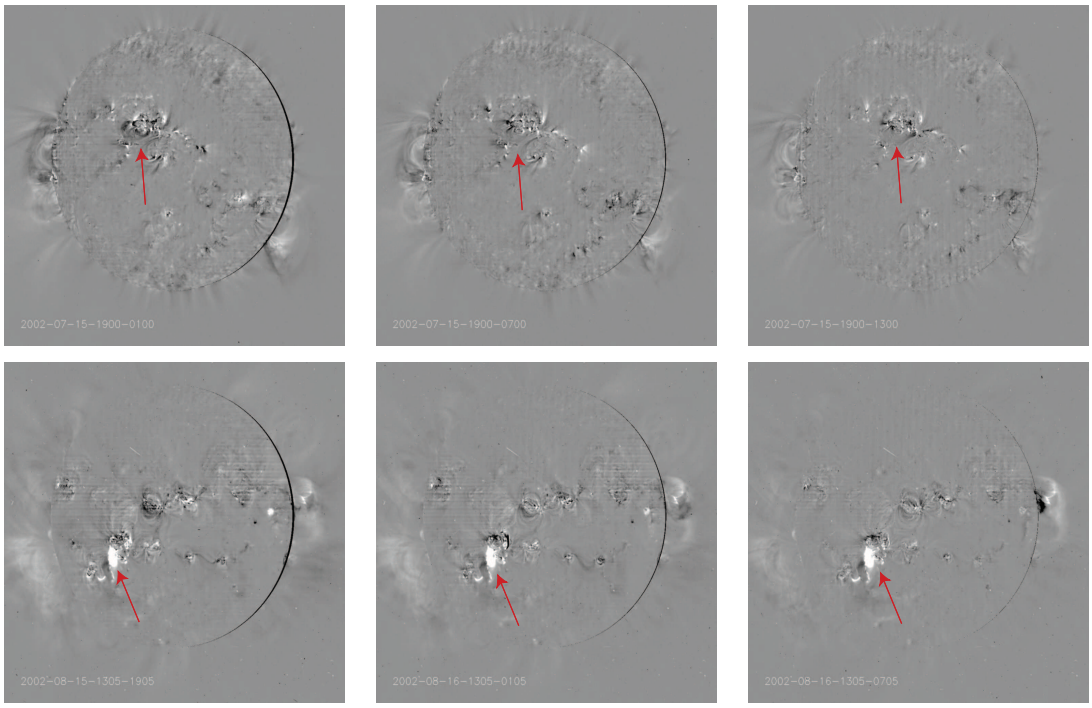

Figure 2.6: *First row : Difference of EIT images acquired at 171 Å, relevant to the event associated to the halo CME that occurred on 15/07/2002 and was detected by LASCO/C2 at 20:30:05. The pivot image was taken at 19:05 UT. Here three images taken 18, 12 and 6 hrs* ***earlier*** *are subtracted from the pivot image. Second row: Difference of EIT images acquired at 284 Å. The halo CME occurred on 16/08/2002 and was first detected by LASCO/C2 at 12:30 UT. The pivot image was acquired at 13:05 UT and we present difference of images taken 6, 12 and 18 hrs* ***later****.*

7. Obtain a set of images relevant to a single or two adjacent active regions for the period between one day before and one day after the halo CME occurrence. In Figure 2.8 we show for example the 171 Å difference images for NOAA 10030. The CME event occurred on 16/07/2002 and was detected by LASCO/C2 at 16:02 UT. The pivot image was acquired at 19:05 UT. From this image we subtracted the images at 01:05 UT (first panel), at 07:05 UT(second panel) and at 13:05 UT(last panel) taken on the following day.

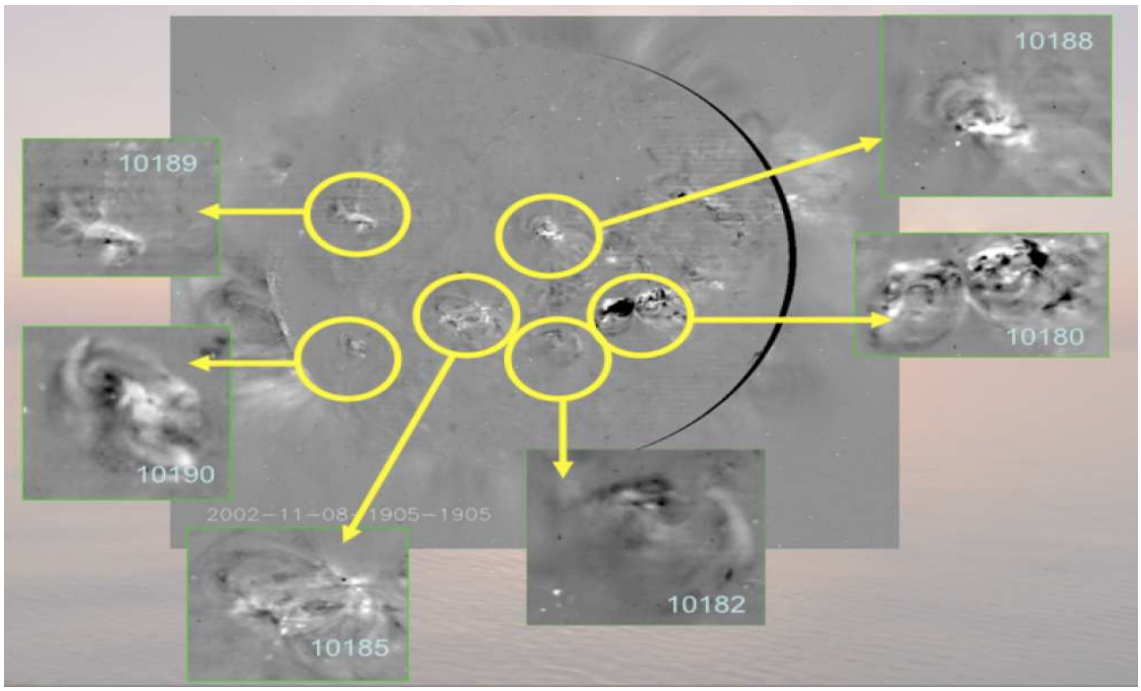

Figure 2.7: *Full-disk 171 Å difference image produced by the difference of the pivot image (acquired at 13:05 UT of 09/11/2002) and the image acquired 24 hrs later (13:05 UT of 10/11/2002). A halo CME occurred on 09/11/1982 and was detected by LASCO/C2 at 13:31UT. All the observed active regions are selected for further investigation.*

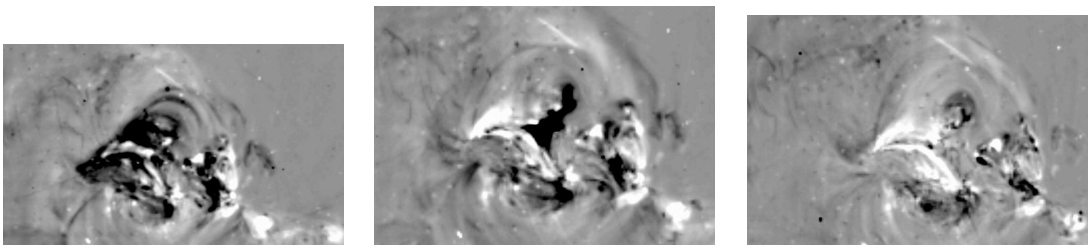

Figure 2.8: *171 Å difference images for NOAA 10030. In this case, the CME event occurred on 16/07/2002 and was detected by LASCO/C2 at 16:02 UT. The pivot image was acquired at 19:05 UT. From this image we subtracted the images at 01:05 UT (first panel), at 07:05 UT (second panel) and at 13:05 UT (last panel) taken on the following day (17/07/2002).*

At this stage we were able to :

(a) Select the biggest brightest and darkest area in each active region with the help of a cursor

(b) Compute the area of the bright biggest region and the area of the dark biggest region

(c) Compute the maximum intensity of the brightest area and the minimum intensity of the darkest area

8. Identify the active region that shows the largest variations in intensity and size (of brightest and darkest area) when the halo CME happens, indicating the occurrence of a dynamic event. In contrast, the other active regions show an almost constant profile in intensity.

9. Follow the same procedure with the full-disk images acquired by EIT at 195 Å. These data have a higher time cadence (12 minutes) than the other data (171 Å, 284 Å, 304 Å). In Figure 2.9 we present the graphs showing the evolution in time of the size (first row) and the intensity (second row) of the largest bright and dark areas of each active region present on the solar disk on 16/07/2002. The 0 in the horizontal axis corresponds to the image taken closer to the CME occurrence (detected at 16:02:58 UT from LASCO/C2), i.e 16:12:10 UT; from this we subtracted images with difference of 12 min until 09:36:10 UT in the same day and 00:36:10UT of the following day (no data were available from 12:36:10 UT till 13:25:59 UT). We can see in each plot that NOAA 10030 (indicated by crosses) shows a different trend than any other active region. Therefore, we considered NOAA 10030 as the initiation site of the CME.

As far as the images acquired by EIT at 195 Å are concerned, we stress that these data are characterized by a higher time resolution (12 minutes) than the other data (171 Å, 284 Å, 304 Å), characterized by 6 hr time cadence, that are nevertheless useful to study how an active region change in such time interval due to a dynamic event.

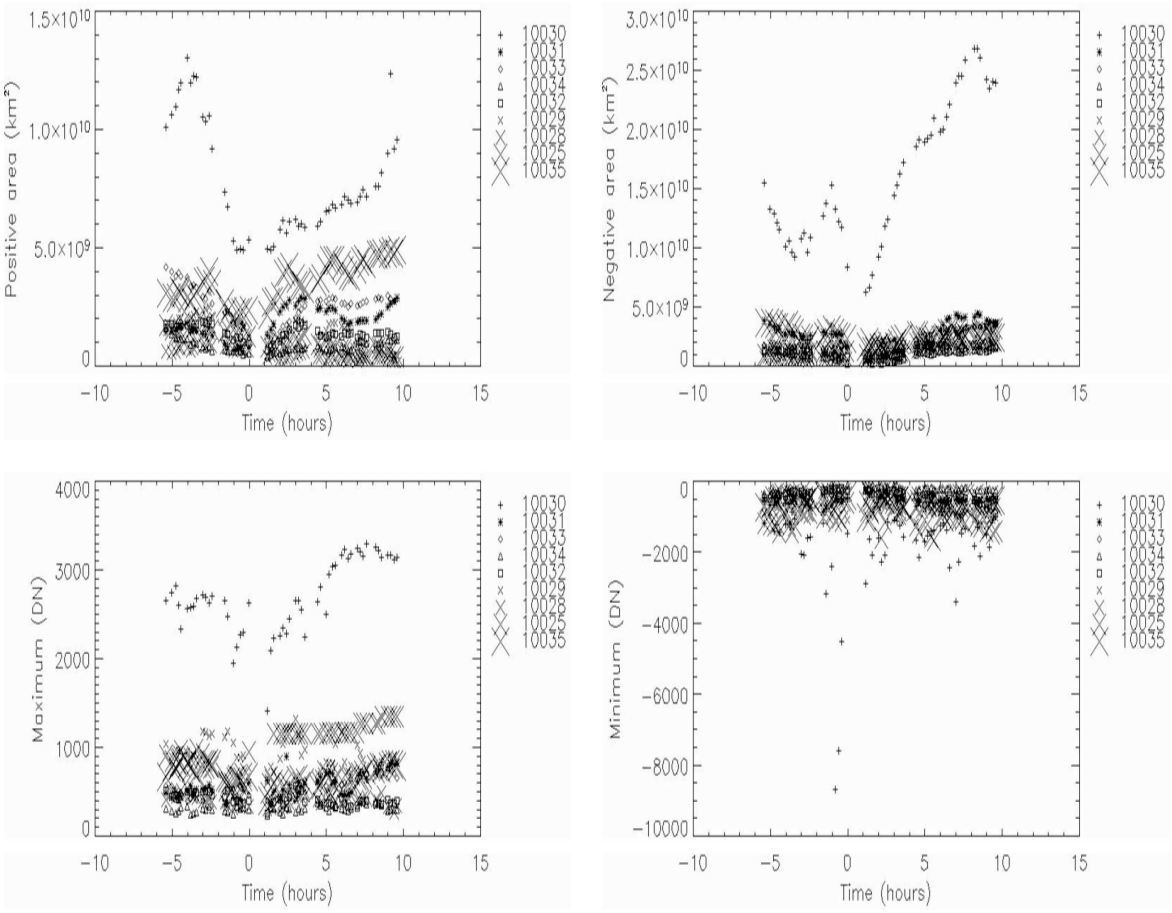

Figure 2.9: *Plots of the size(first row) and the intensity (second row) of the largest bright and dark area vs. time as obtained from the difference of 195 Å images for each active region selected on 16/07/2002. The time cadence is 12 min. We note that the NOAA 10030 (shown by crosses) shows different trend than the other regions and thus can be considered as the most probable initiation site for the CME that was detected at 16:02:58 UT. Time* 0 *corresponds to the image acquired closer in time to the CME occurrence.*

Thus, with images acquired at the three last wavelengths we can obtain a first idea about the candidates (i.e active regions) that are most probably connected to an eruptive event. Then, with the 195 Å images we can observe the evolution of these regions in short temporal periods. When a different trend (relatively to any other active region on the solar

disk) and abrupt changes are detected close to the eruption occurrence (i.e some couple of hours before and after the event), we can verify our 'suspicious' about the origin site of a halo CME.

Moreover, the data acquired at 195 Å can be quite useful in identifying dimming regions that most of the time provide information about the CME source region. Coronal dimmings are usually regarded as the consequence of removal of coronal mass during a CME eruption (Sterling & Hudson (1997); Zarro et al. (1999);Reinard & Biesecker (2008)) and sometimes appear near a flare or near an arcade brightening associated with a filament eruption (Hudson et al. (1996);Canfield et al. (1999)). Dimmings are dynamic phenomena that can develop on a typical timescale of a hour and so their evolution is fast enough and only snapshots of an active region in short time intervals can make apparent their occurrence. There appear to be two classes of dimmings: deep core dimmings (e.g Webb et al. (2000)) and more widespread dimmings coincident with the spatial extent of CMEs detected by coronographs (as investigated by Thompson et al. (2000)). Since during our analysis we are not only interested in bright areas that can be connected to a flare, but also to dark areas that can be connected to coronal dimmings, we need low time cadence data in order to recognize them. These data can only be provided by EIT at 195 Å.

Summarizing, we have selected 38 halo CME events and for each event we have explored the trend in brightness variations of all the active regions detected in the full-disk EIT images acquired on the same day. The double-cross check between the eruptive event registered in the NOAA report and the brightness variation inferred by the difference maps provided us a further indication about the active region that was the site of the initiation of the halo CME. In order to minimize problems related to projection effects, we focused our attention on active regions located between $\pm 35^{\circ}$ of longitude from the central meridian. With this choice, we limited our analysis to 10 active regions and, correspondingly, to 12 CMEs, because both NOAA 10030 and 10365 were the source regions of two halo CMEs.

The halo CME events selected and the relevant active regions found by this method are reported in Figure 2.10, where we distinguish two classes: the first containing active regions giving rise to gradual halo CMEs, i.e. with positive acceleration (hereinafter called Class

Day	CME time[a] (UT)	Linear speed (km s^{-1})	Acceleration (m s^{-2})	Gradual (g) or impulsive (i)	Associated event[b] (Beg, Max, End)UT	Active region NOAA number
2000-02-10	02:30:05	944	11.4	g	C7.3 (01:40, 02:08, 02:39)	8858
2000-04-10	00:30:05	409	2.5	g	M3.1 (23:26, 23:42, 23:55)	8948
2000-08-09	16:30:05	720	2.8	g	C2.3-ERU (15:19, 16:22, 17:00)	9114
2001-03-29	10:26:05	942	3.5	g	X1.7 (09:57, 10:15, 10:32)	9393
2001-04-10	05:30:00	2411	211.6	g	X2.3 (05:06, 05:26, 05:42)	9415
2002-07-15	20:30:05	1151	−25.6	i	X3.0 (19:59, 20:08, 20:14)	10030
2002-07-16	16:02:58	1636	−41.0	i	ERU (15:36, 15:39, 15:49)	10030
2002-08-16	12:30:05	1585	−67.1	i	M5.2-ERU (11:32, 12:32, 13:07)	10069
2002-10-25	15:06:05	870	−23.4	i	ERU (14:09, 14:11, 14:18)	10162
2002-12-19	22:06:05	1092	−36.2	i	M2.7 (21:34, 21:53, 22:17)	10229
2003-05-27	06:50:05	509	−14.6	i	M1.6 (05:06, 06:26, 07:16)	10365
2003-05-27	23:50:05	964	−9.6	i	X1.3 (22:56, 23:07, 23:13)	10365

Figure 2.10: *Data on the halo CMEs and analyzed relevant eruptive events.* [a]*: the CME time indicates the time of first appearance in LASCO/C2.* [b]*: ERU indicates the occurrence of an erupting filament.*

I) and the second relevant to active regions that were sources of impulsive halo CMEs, i.e. characterized by negative acceleration (Class II). In particular, this classification is based on the velocity and acceleration values of a CME:

I) *gradual* CMEs, characterized by velocities $v \sim$ 400 - 600 km s^{-1} and gradual acceleration ($a \sim$ 3 - 40 m s^{-2} within a distance from the Sun less than $\sim$ 30 R$_\odot$), generally associated with eruptive quiescent filaments;

II) *impulsive* CMEs with higher initial velocities, in the range $\sim$ 750 - 1000 km s^{-1}, decelerating at distances $\sim$ 2 R$_\odot$ and generally associated with flares and eruptive active region filaments.

This categorization has its roots on the work of Gosling et al. (1976) and MacQueen & Fisher (1983) who suggested different mechanisms for the acceleration of CMEs. More specifically, their study has revealed that the reason for the different dynamical behavior might be due to a **different driver mechanism** (or at least one with a different strength): gradual CMEs, which are events associated to eruptive quiescent prominences, are supposed to undergo a significant net propelling force over extended periods, while impulsive CMEs, which are flare-associated events, are supposed to arise from an impulsive input into the low corona associated to flare and active region filament eruptions. This traditional classification was afterwards widely used in the study and comprehension of the kinematics of CMEs (as we can see for instance by Chen & Krall (2003); Moon

et al. (2004), Chen et al. (2006), Michalek (2009)).However, it is important to mention that this classification of CMEs has been questioned due to the fact that the study of the kinematical curve is very subjective and it depends on the performance of the instruments, the measurement technique and the morphology of a CME. For this reason, Vršnak et al. (2004) proposed the existence of a continuum of events rather than two distinct categories of CMEs since they found in both types several fast and slow events that either decelerate or accelerate. Moreover, Yurchyshyn et al. (2005) confirmed the lack of observational that can support the two-types classification of CMEs. For simplicity, we adopt this classification when analyzing our results.

2.3 Analysis and Selection of MDI images

In this section we investigate the magnetic helicity flux (or rate) injected through the photosphere by using images acquired by the Michelson Doppler Imager (MDI) on board SOHO. Figure 2.11(a) shows the optical layout of MDI and Figure 2.11(b) shows a magnetogram available at the MDI database (http://soi.stanford.edu/data/).

The Michelson Doppler Imager (MDI) instrument (see Scherrer et al. (1995) for a full description of the instrument capabilities), is designed to probe the interior of the Sun by measuring the photospheric manifestations of solar oscillations. MDI measures the line-of-sight motion (Dopplergrams), magnetic fields (magnetograms) and brightness images in full disk at a resolution of 2 arcsecond/pixel, and a fixed selected area at the disk centre in higher resolution (0.62 arcsecond/pixel). As far as magnetograms are concerned, they show the distribution of the magnetic field across the solar disk, obtained by measures of the magnetic strength using Zeeman splitting of the NiI photospheric line at 6767.8 Å.

In Figure 2.12(a) we present an EIT/SOHO image of the active region NOAA 10030 which was identified by the previously mentioned double check as the source region of the halo CME that occurred on 15/07/2002 at 20:30:05 and in Figure 2.12(b) we show the MDI/SOHO magnetogram relevant to NOAA 10030, acquired at 20:30 UT.

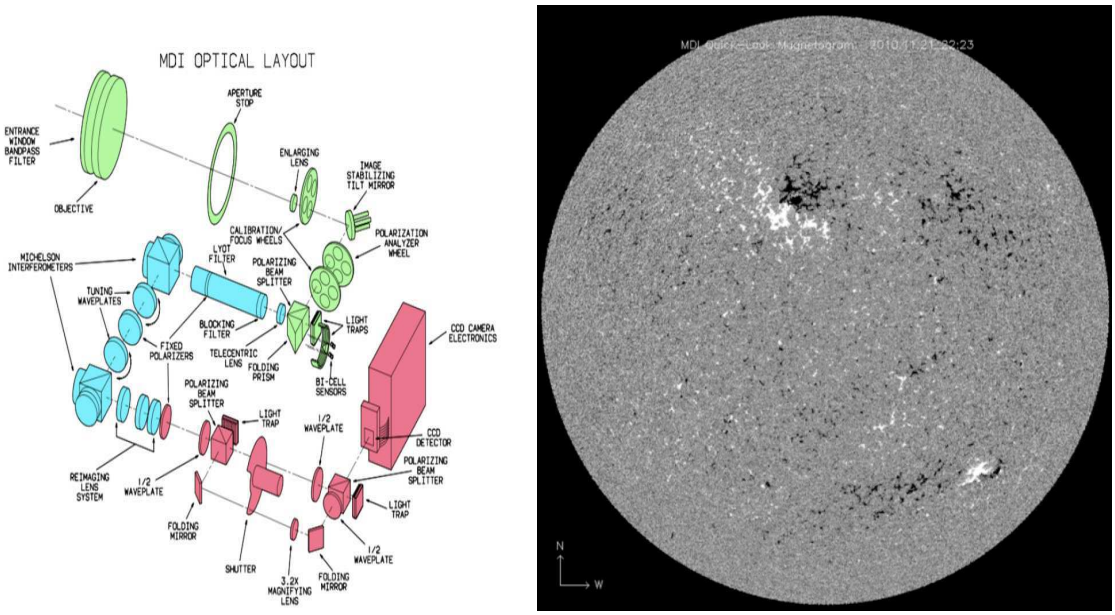

Figure 2.11: *(a)MDI Optical Layout ; (b) MDI/SOHO magnetogram from the MDI database (http://soi.stanford.edu/data/) acquired on 21/11/2010.*

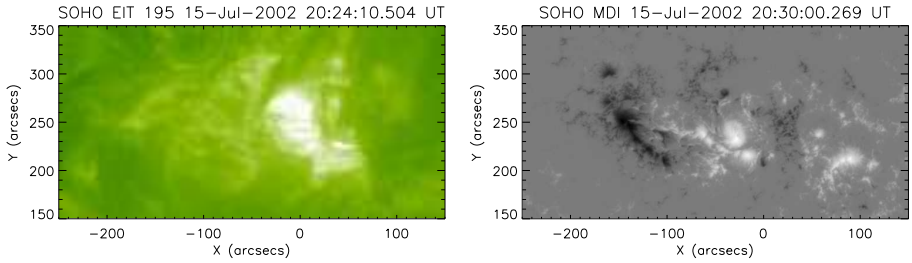

(a) **(b)**

Figure 2.12: *(a) Zoom of the active region NOAA 10030 where a flare occurred and a CME was initiated; the image was acquired at 195 Å by SOHO/EIT during the main phase of the flare; (b) MDI/SOHO magnetogram showing the magnetic configuration of NOAA 10030 on 15 July 2002.*

2.3.1 Magnetic Helicity Calculation in the coronal volume of an active region

We recall that magnetic helicity, defined as $H = \int_V \mathbf{A} \cdot \mathbf{B}\ dV$, is a gauge-dependent quantity unless the boundaries of the volume V are periodic or perfectly conducting. Since our study is related to coronal volumes enclosing the selected active regions, we are dealing with open boundaries. Thus, we work with the commonly-used quantity **relative magnetic helicity** (Berger & Field (1984)), that we have mentioned in Chpater 1: $H_{rel} = \int (\mathbf{A} + \mathbf{A}_p) \cdot (\mathbf{B} - \mathbf{B}_p) dV$.

This relative magnetic helicity may vary due to the passage of magnetic field lines through the photospheric boundary (when the flux emerges), or through the sides (when the magnetic field expands to be in contact with neighboring active regions), or through the outer boundary (when a coronal mass ejection occurs). Unlike the magnetic helicity of fully enclosed magnetic fields, the helicity of open magnetic fields may change with time as it is transported through the boundaries. In this regard, it is worthwhile mentioning that most of the helicity injection in an active region occurs during magnetic flux emergence (Tian et al. (2008)).

Therefore, the magnetic helicity in the coronal volume of an active region is a function of time. In order to determine this time variation, it is possible to use the following equation (Berger & Field (1984)) for the helicity flux (or injection rate) *dH/dt* through a planar surface S_p (indicating the photospheric portion of the surface S bounding the volume V):

$$\frac{dH}{dt} = -2 \int_{S_p} \left[(\mathbf{v}_t \cdot \mathbf{A}_p)\ B_n - (\mathbf{A}_p \cdot \mathbf{B}_t)\ v_n \right]\ dS\ , \tag{2.1}$$

where the magnetic field **B** and the velocity field **v** are observable quantities, the subscript n represents the component of the magnetic field **B** and of the velocity **v** normal to the surface S_p, whereas the subscript t represents the tangential component.

The magnetic helicity content of an active region at a specific time can be determined by integrating the helicity injection rate over time since its birth to the specified time, provided that no CME occurred which would have carried away helicity. According to Eq. (2.1), the magnetic helicity in an open volume can change either by the shuffling horizontal

motions of field lines on the surface (first term, called shear term) or by the passage of twisted or sheared fields through the solar surface (second term, called emergence term).

2.3.2 Calculation of the Magnetic Helicity injected through the photosphere from a series of line-of-sight magnetograms

Two main methods for measuring the magnetic helicity flux through the photosphere have been developed:

* **Chae method** Chae (2001) showed that when magnetic fields are normal to the surface, the flux distribution on the surface $\mathbf{B}_n$ can be exploited to determine the non-steady transverse motion of the field-line footpoints, and proposed to use the displacement velocity U_{LCT} determined by the technique of the local cross-correlation tracking (LCT) as a proxy for the transverse motion v_t. He also introduced a Fourier transform method for the fast computation of A_p from the B_n. Moreover, following Démoulin & Berger (2003) and as we can derive from the Figure 2.13, it is possible to write:

$$U_{LCT} = v_t - \frac{v_n}{B_n} B_t \ , \tag{2.2}$$

and the photospheric helicity flux (or injection rate) simplifies to

$$\frac{dH}{dt} = -2 \int (\mathbf{U}_{LCT} \cdot \mathbf{A}_p) \mathbf{B}_n \ dS \ , \tag{2.3}$$

These equations put together the shear and emergence terms, as Démoulin & Berger (2003) realized that the emergence of a twisted flux system would cause what may appear as shear flows.

* **Pariat method** Pariat et al. (2005) showed that Eq. (2.3) introduces artificial signals because helicity flux densities per unit surface are not physical quantities. Therefore they presented a new estimation of helicity flux per unit of elementary magnetic flux. In this case the helicity flux is given by

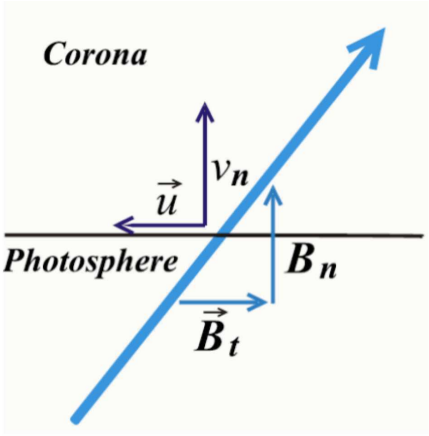

Figure 2.13: *A schematic drawing of a flux tube that rises through the photosphere as presented in Démoulin & Berger (2003). The photospheric footpoint of a field line is moving along the photospheric surface with velocity* $-\frac{v_n}{B_n}B_t$

$$\frac{dH}{dt} = -\frac{1}{2\pi} \int_S \int_{S'} \frac{dA(r)}{dt} B_n B'_n \, dS \, dS' \, , \tag{2.4}$$

where S=S' is the integration surface, $\frac{dA(r)}{dt}$ the relative rotation rate of pairs of photospheric positions defined by x and x', with $r = x - x'$. The use of the helicity flux density per unit of elementary magnetic flux permits us to reduce spurious signals.

The LCT method has some important practical advantages. First of all, it makes use of the line-of-sight magnetograms that are commonly available. Secondly, it is simple to implement, robust and flexible. However, it is possible to introduce large systematic errors into the results by not choosing interpolation algorithms with sufficient care (Potts et al. 2003) or by not choosing the correct size for the two input parameters of this method: FWHM (full width at half maximum) that defines the width of the apodizing window, and the time interval Δt between two images of comparison.

The accumulated magnetic helicity H_i (or total magnetic helicity injection) due to changes across the photospheric boundary can be determined by integrating the

values of the helicity injection rate over the entire time interval Δt analyzed:

$$H_i = \int_0^{\Delta t} \frac{dH}{dt} dt \ , \tag{2.5}$$

Finally, indicating with Φ the average of the magnetic flux crossing the photosphere (given by $\Phi = 0.5\ \Phi_{pos} + 0.5\ |\Phi_{neg}|$), it is useful to evaluate the normalized helicity $|H_i|\ /\Phi^2$, which provides a measure of how much a magnetic configuration is stressed.

Hence, we apply the method developed by Pariat in order to estimate the magnetic helicity flux *dH/dt* and to reduce spurious signals (see also Démoulin (2007) and references therein; Démoulin & Pariat (2009)) for the two sets (Class I and Class II) of CME events by means of MDI/SOHO low-resolution magnetograms taken with a 96 minute cadence.

For each sequence of magnetograms relevant to each active region we determined:

* **The vertical field strength** B_n by multiplying the MDI/SOHO line-of-sight component by $1/\cos\psi$, where ψ is the heliocentric angle. We studied the magnetic evolution of each active region with respect to the time of the first observation of the CME in the LASCO/C2 field-of-view, which is considered below as the reference-time point. The collection of the line-of-sight magnetograms for each active region was carried out over a period of time that was chosen on the basis of the following two characteristics: 1) the time period expands over at least 24 hours before and after the reference time; 2) during this time interval the longitude of the active region must be within $\pm\ 35°$.

* **The parameter of full width at half maximum (FWHM) and the time interval** Δt. The FWHM of the apodizing window function is used into the LCT method and depends on the pixel resolution. We assume a $FWHM = 10'$ that is equivalent to 5 pixels (since the resolution of the magnetograms is $2'$). As far as the time interval is concerned, we select magnetograms for which $\Delta t = 96$ min.

* **The horizontal velocities** of magnetic field lines at photospheric footpoints are determined by measuring the local displacements of magnetic flux concentrations

between two successive magnetograms with the LCT technique.

* **The spatial alignment** of all the images included in each data set is performed by spatially aligning the sequence of magnetograms relevant to each active region by successive non-linear mapping, which takes into account the solar differential rotation effect

This procedure allows us to determine and plot the magnetic flux (total, positive and negative) trend, magnetic helicity injection rate *dH/dt*, accumulated magnetic helicity H_i (that can be estimated by integrating the measured *dH/dt* from the start of the observing run to a specific time) and ratio $|H_i|/\Phi^2$ for the selected active regions. Since some active regions are very close to other active regions (e.g., NOAA 9114, NOAA 9393, NOAA 10069) and an exchange of magnetic helicity flux between them may be occurring (as suggested by Yang et al. (2009) for adjacent active regions) that can affect our calculations, we merge the above mentioned active regions with their neighboring ones (e.g., NOAA 9114+9115, NOAA 9393+9394, NOAA 10069 + 10077) and calculated the total helicity flux

2.4 Results

2.4.1 Class I: Gradual CMEs

In Figure 2.14 we report the evolution of total, positive, and negative magnetic flux expressed in 10^{22} Mx (first row), helicity injection rate dH/dt in 10^{42} Mx^2 hr^{-1} (second row), accumulated helicity injection H_i in 10^{42} Mx^2 (third row), ratio $|H_i|/\Phi^2$ (fourth row), positive (H_+) and negative (H_-) accumulated helicity injection (fifth row) for NOAA 8858 and NOAA 9415 belonging to the Class I (gradual CMEs). Similar plots are reported in Figure 2.15 for NOAA 8948, 9114+9115 and 9393+9394.

* **NOAA 8858** (Figure 2.14, left panel): the total magnetic flux shows a very small decrease during the analyzed period (more precisely, the positive flux remains almost constant, while the negative flux slightly decreases). The helicity injection rate is generally negative, with the exception of few points with positive values. The

accumulated helicity injection H_i shows a continuous increase (in absolute value), with a significant change in the curve slope *after* the CME event (third row). This change is also evident in the $|H_i|/\Phi^2$ curve (fourth row), where it seems possible to distinguish two different regimes. The inspection of the graph shown in the fifth row, which gives the trend of the accumulated negative (asterisks) and positive (crosses) helicity injection, reveals that H_- increases and changes its trend after the CME occurrence, while H_+ is very small and almost constant during the analyzed period. Note that the gradual CME was characterized by a velocity of 944 km s^{-1} and an acceleration of 11.4 m s^{-2}, and was associated with a C7.3 class flare.

* **NOAA 9415** (Figure 2.14, right panel): the total magnetic flux is constant during the analyzed period, whereas the helicity injection rate shows alternating negative and positive values, with some more abrupt changes just before the CME. The accumulated helicity injection shows predominantly negative values prior to the CME occurrence and a successive rise to positive values after it. The ratio $|H_i|/\Phi^2$ has a very irregular behavior, with a sudden change immediately before the CME and a clear increasing trend after it. The values of H_- and H_+ show a very peculiar behavior, characterized by alternate phases where one component remains constant, while the other increases. Interestingly, one of the changes is temporarily correlated with the CME occurrence. The velocity and acceleration of the CME were 2411 km s^{-1} and 211.6 m s^{-2}, respectively, and the associated flare was of X2.3 class.

* **NOAA 8948** (Figure 2.15, leftt panel): the total, positive, and negative magnetic flux are slightly decreasing during the period analyzed. However, if we limit our attention to the time interval preceding the CME, we note a slight increase of both positive and negative magnetic fluxes. The helicity injection rate *dH/dt* (second row) is prevalently positive, with the exception of the last part of the analyzed period. The accumulated helicity injection (third row) is initially characterized by increasing positive values and in the last part of the analyzed period by a decreasing trend. The $|H_i|/\Phi^2$ ratio (fourth row) shows an increasing trend till the time of the

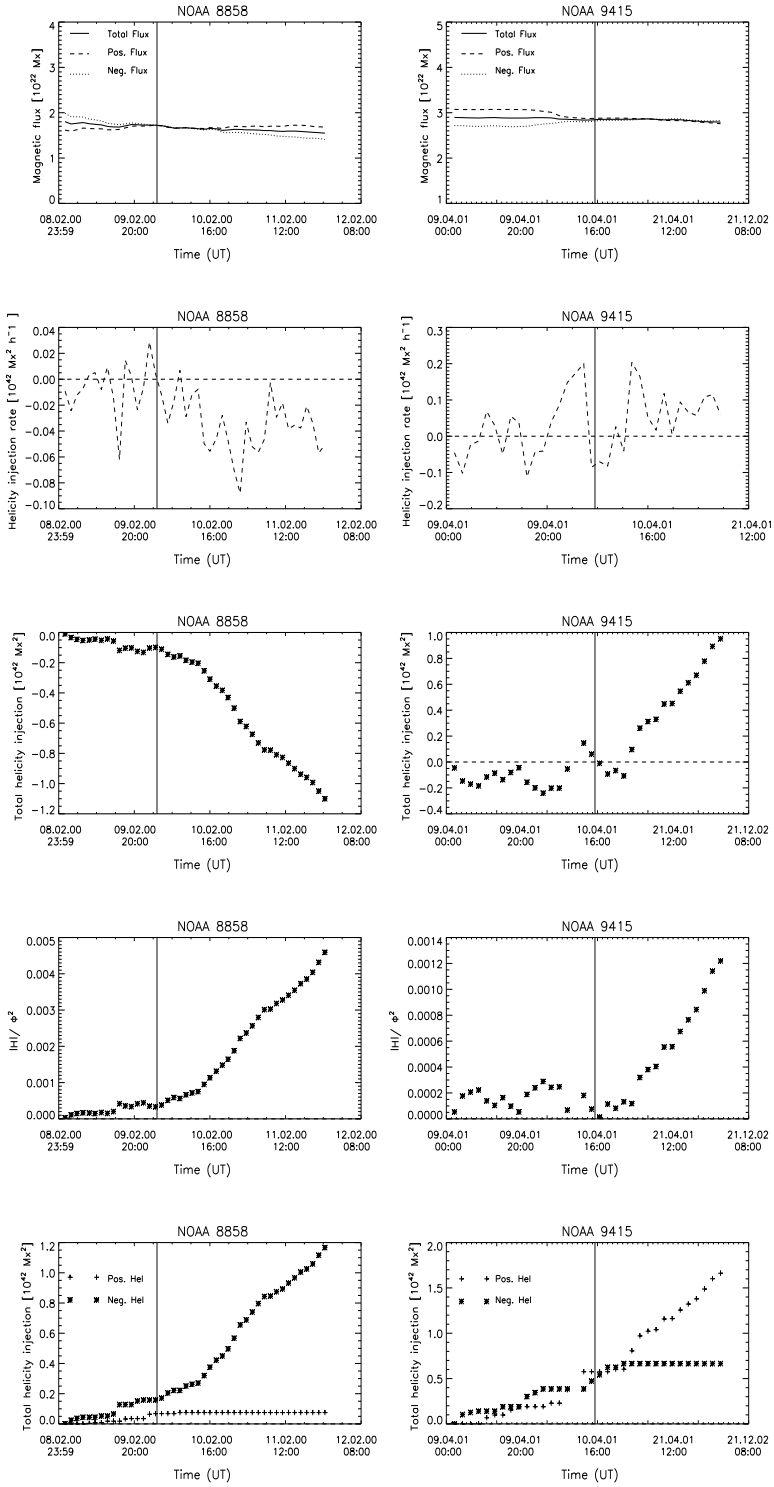

Figure 2.14: *From top to bottom: evolution of the magnetic flux (continuous line indicates the average total flux, marked line the positive flux and dotted line the negative flux), magnetic helicity injection rate, total helicity injection, ratio* $|H_i|/\Phi^2$*, positive* H_+ *and negative* H_- *accumulated helicity injection for ARs 8858, and 9415, belonging to Class I (gradual CMEs). Vertical lines indicate the time of the CME occurrence. Horizontal lines in the second and third rows indicate the zero values for the reported parameters.*

corresponding increase in H_- (see the graph in the fifth row), but not correlated with the CME occurrence. The graph in the fifth row shows that the main contribution to the helicity injection is due to the increase of H_+, while there is an increase of H_- only during the last part of the analyzed period. The CME had a velocity of 409 km s^{-1}, an acceleration of 2.5 m s^{-2}, and was associated to an M3.1 flare.

* **NOAA 9114+9115** (Figure 2.15, middle panel): the total magnetic flux is slightly increasing during the analyzed period and in particular just before the CME occurrence; the helicity injection rate (second row), which is always characterized by negative values, shows an evident increasing trend before the CME occurrence (till the value of -0.4×10^{42} Mx^2) and a phase characterized by lower values (till -0.1×10^{42} Mx^2) *after* it. The accumulated helicity injection (third row) shows a different trend before and after the CME occurrence. This behavior is also evident in the curve showing the ratio $|H_i|/\Phi^2$. The graph reported in the fifth row indicates that the contribution to H_i is only due to H_-. Note that the CME had a velocity of 720 km s^{-1}, an acceleration of 2.8 m s^{-2} and it was associated with a C2.3 flare and an erupting filament.

* **NOAA 9393+9394** (Figure 2.15, right panel): the total magnetic flux shows an increase during the analyzed period (in this case, the positive flux increases, whereas the negative flux decreases); the helicity injection rate (second row) is predominantly characterized by negative values. The curve showing the accumulated helicity injection H_i indicates that there is a continuous increase of helicity, always characterized by negative values, also after the CME. Interestingly, the trend shows a slight variation a few hours before the CME. A similar trend is shown by the H_i/Φ^2 values (fourth row). The graph reported in the fifth row indicates that the main contribution to H_i is due to H_-, and that H_+ starts to increase some hours before the CME occurrence. In this case, the CME, associated to an X1.7 flare, had a velocity of 942 km s^{-1} and an acceleration of 3.5 m s^{-2}.

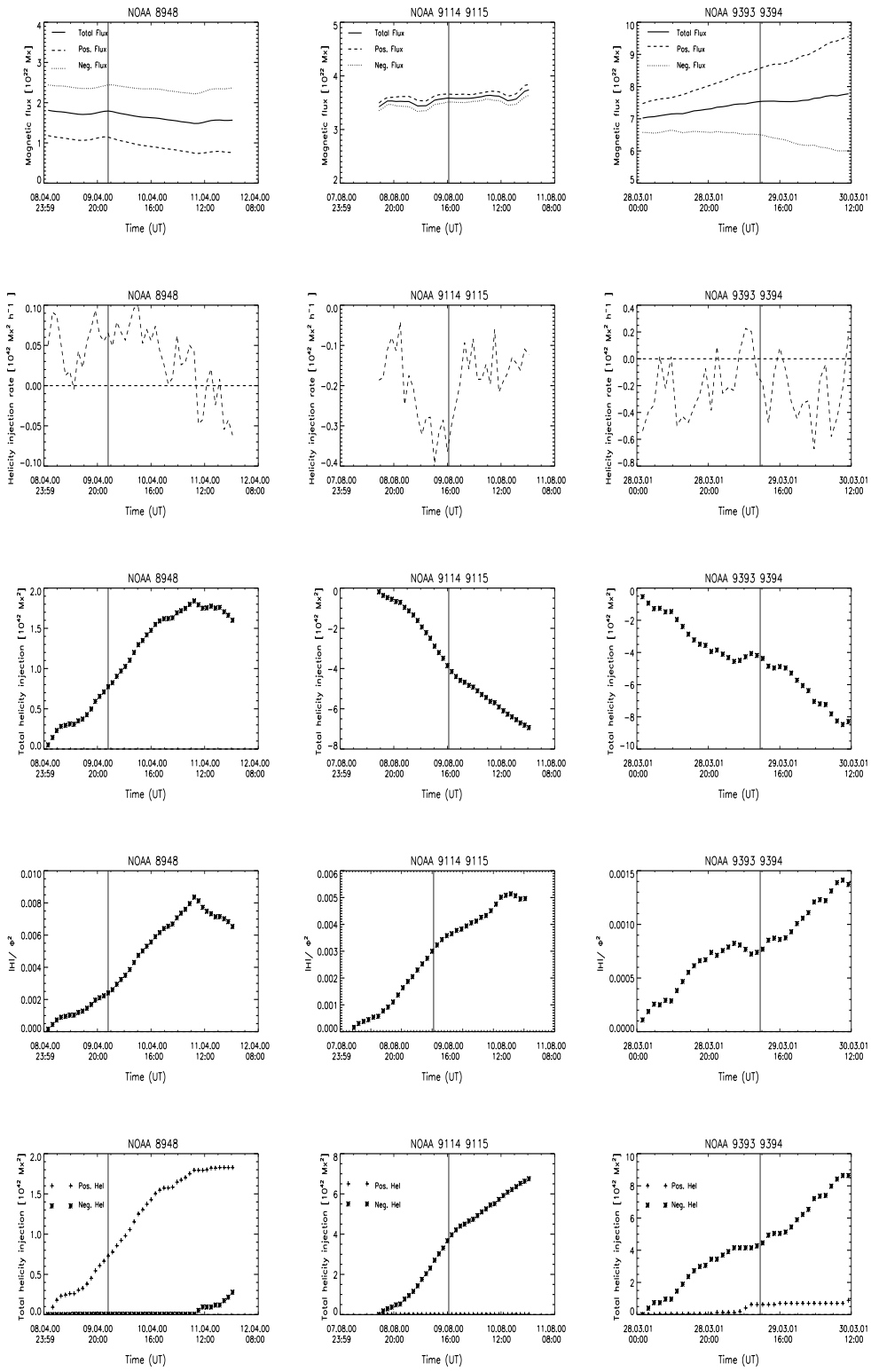

Figure 2.15: *Same as in Figure 2.14 for AR 8948, 9114+9115 and 9393+9394, belonging to Class I (gradual CMEs).*

2.4.2 Class II: Impulsive CMEs

In Figure 2.16 we report the evolution of total, positive, and negative magnetic flux expressed in 10^{22} Mx (first row), helicity injection rate dH/dt in 10^{42} Mx^2 hr^{-1} (second row), accumulated helicity injection H_i in 10^{42} Mx^2 (third row), ratio $|H_i|/\Phi^2$ (fourth row), positive (H_+) and negative (H_-) accumulated helicity injection (fifth row) for 10030 and 10069+10077, belonging to Class II (impulsive CMEs). Similar plots are reported in Figure 2.17 for NOAA 10162, 10229 and 10365.

* **NOAA 10030** (Figure 2.16, left panel): during the analyzed period (five days), the total magnetic flux (as well as the positive and negative fluxes) shows a continuous increase, the helicity injection rate varies initially from positive to negative values and shows sudden changes in coincidence with the occurrence of two halo CMEs; in particular, after the second event, it again assumes positive values. H_i shows a continuous decrease after an initial increase to a maximum value of $\sim 2 \times 10^{42}$ Mx^2 hr^{-1}, and an abrupt variation immediately after the second CME. However, when we look at the curve showing the ratio $|H_i|/\Phi^2$ (fourth row), we notice that there is a very abrupt change immediately *before* the first CME and immediately *after* the second CME. The first change is due to the change in the sign of the accumulated helicity injection, while the latter might be explained by the changes in the trends of H_- and H_+. In particular, concerning the trend of H_- and H_+, reported in the fifth row, we can see that H_- is initially constant, then (some hours before the first CME) it starts to increase and this increase abruptly stops just before the second CME. The behavior of H_+ is almost specular: it is increasing at the beginning of the period examined, then it stops (approximately when H_- starts to rise) and again suddenly starts to increase in coincidence with the CME (when H_- becomes constant). Note that the first CME, associated with an X3.0 class flare, was characterized by a velocity, as measured by LASCO C2, of 1151 km s^{-1} and a deceleration of 25.6 m s^{-2}, whereas the second CME had a velocity of 1636 km s^{-1}, a deceleration of 41.0 m s^{-2}, and was associated to an erupting filament.

* **NOAA 10069+10077** (Fig. 2.16, right panel): the magnetic flux shows an increase during the analyzed period, while the helicity injection rate (second row) is initially characterized by negative values and, after the CME occurrence, by positive values. This trend is reflected in the curve representing the accumulated helicity injection H_i, where the abrupt variation immediately *after* the CME is evident. The same behavior is shown by the $|H_i|/\Phi^2$ values (fourth row). The graph shown in the fifth row shows that H_- and H_+ have a similar trend to that observed for NOAA 10030: H_- initially increases while H_+ remains constant and after the CME they invert their trends: H_- remains constant while H_+ starts to increase. In this case, the CME velocity was 1585 km s^{-1}, the deceleration was 67.1 m s^{-2}, and the associated M5.2 flare was related to an erupting filament.

* **NOAA 10162** (Figure 2.17, left panel): the total magnetic flux is almost constant during the analyzed period (this is due to a smooth increase of the positive flux and to a contemporary decrease of the negative flux); the helicity injection rate shows a very spiky behavior, generally characterized by positive values. The accumulated helicity shows an almost monotonic increase, with a small plateau (reflecting the dH/dt value) at the CME occurrence. The ratio $|H_i|/\Phi^2$ shows an increasing trend with a similar plateau in coincidence with the CME occurrence. H_+ has a trend similar to H_i and $|H_i|/\Phi^2$, while H_- remains constant (assuming values very close to zero). In this case, the CME had a velocity of 870 km s^{-1}, a deceleration of 23.4 m s^{-2} and was associated with an erupting filament.

* **NOAA 10229** (Figure 2.17, middle panel): in this active region the total magnetic flux decreases during the analyzed period (the negative flux shows a stronger decrease than the positive flux), whereas the helicity injection rate generally shows negative values, with some abrupt changes to positive values. The accumulated helicity, and correspondingly the ratio $|H_i|/\Phi^2$ are monotonically increasing. In this case H_- (see the graph in the fifth row) shows a continuous increase, while H_+ has only a slight increase just before the CME occurrence and again some hours later. The velocity

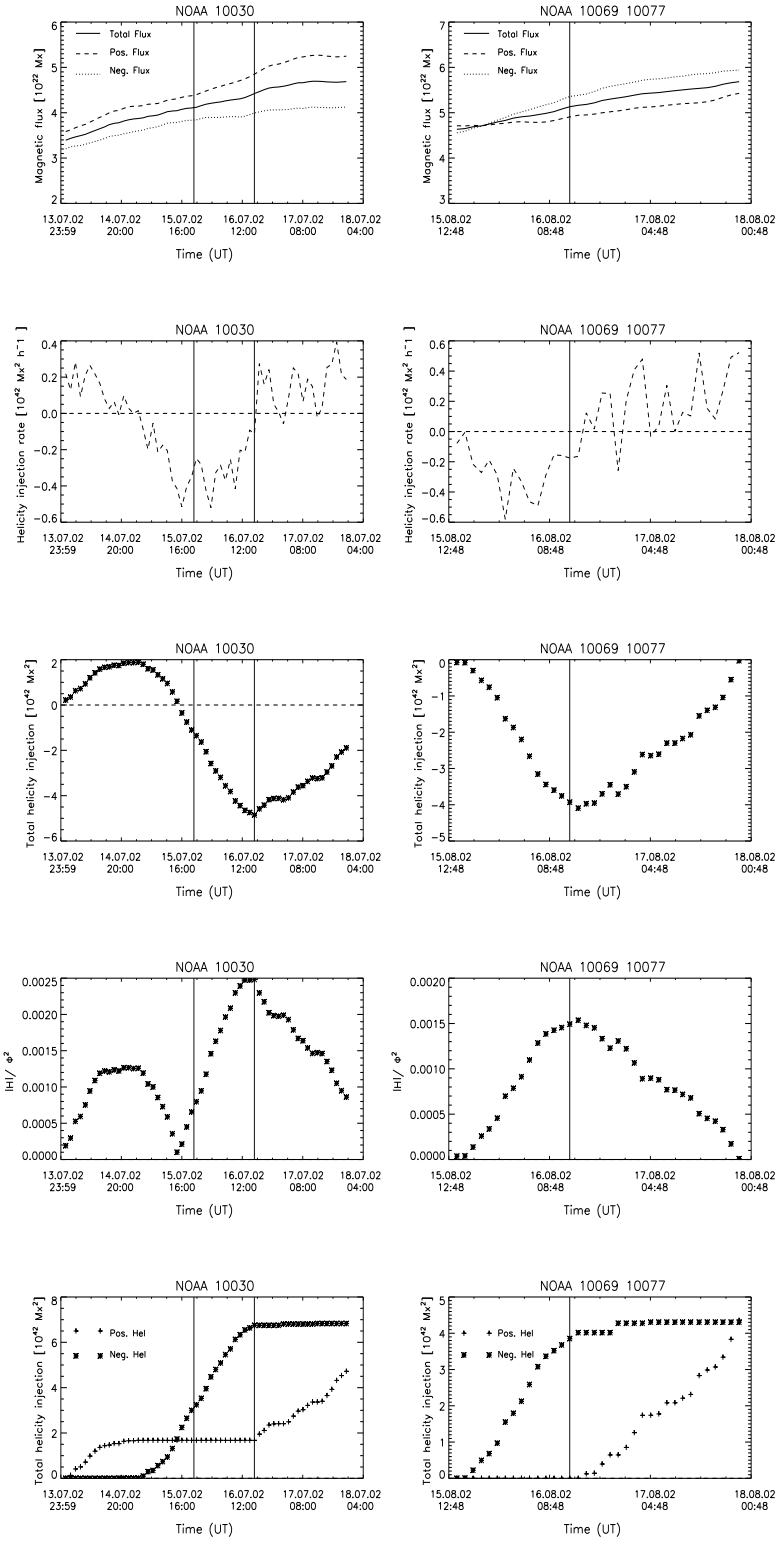

Figure 2.16: *Same as in Figure 2.14 for AR 10030 and 10069+10077, belonging to Class II (impulsive CMEs).*

and deceleration of the CME were 1092 km s^{-1} and 36.2 m s^{-2}, respectively, and the associated flare was of M2.7 class.

* **NOAA 10365** (Figure 2.17, right panel): in the first row we can see that the total magnetic flux shows an evident increase during the analyzed period. However, a more careful inspection of this graph indicates that there is a clear increase before the first CME and almost no increase before the second CME. The helicity injection rate dH/dt is initially characterized by positive values and does not show significant variation after the first CME, while it changes, assuming also negative values, after the second CME. This behavior is clearly shown in the accumulated helicity (third row) and even more evidently in the $|H_i|/\Phi^2$ trend, especially as far as the second event is concerned. Similarly, H_+ (see the graph in the fifth row), which increases during the entire analyzed period, shows a small plateau after the second CME, and later starts to increase again, while H_-, which was almost zero until this event, starts to increase. The first CME had a velocity of 509 km s^{-1}, a deceleration of 14.6 m s^{-2}, and was associated with an M1.6 flare, while the second CME presented a velocity of 964 km s^{-1}, a deceleration of 9.6 m s^{-2}, and was associated with an X1.3 flare.

Our results for all of the selected ARs are presented in the Table 2.10 We note that the $|H_i|/\Phi^2$ values obtained in our analysis for both Classes of CMEs are lower than those obtained by Démoulin & Pariat (2009): this is probably due to the limited time interval we used for the measurements of helicity accumulation, which in most of the cases excluded the emergence phase.

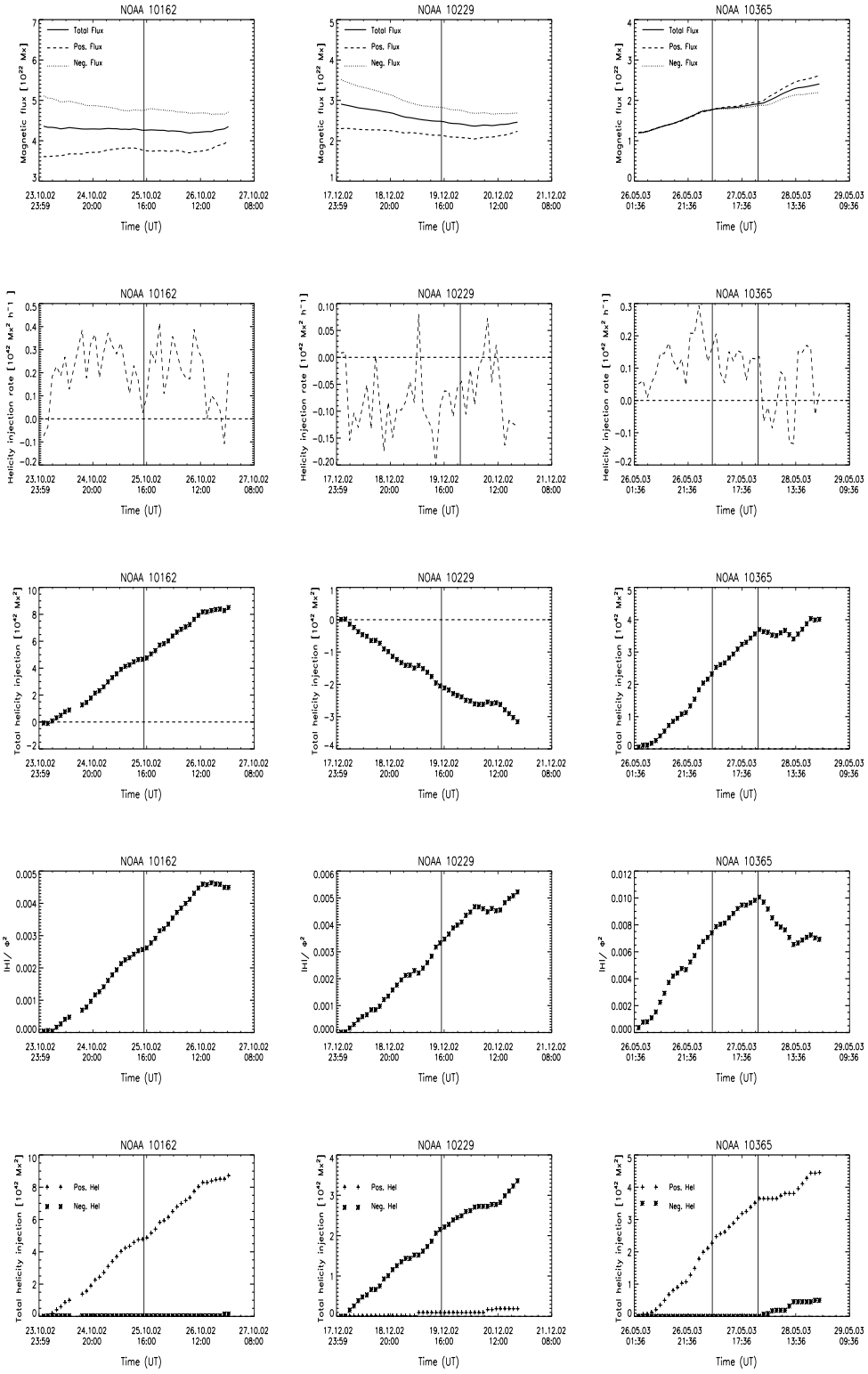

Figure 2.17: *Same as in Figure 2.14 for AR 10162, 10229 and 10365, belonging to Class II (impulsive CMEs).*

NOAA	Latitude degrees	Event class	TMF[a]	HC[b]	TC[c]	ΔH_+ 10^{42} Mx^2	ΔH_- 10^{42} Mx^2
8858	+27	C7.3	slightly decreasing	yes	after	0.1	1.2
8948	−15	M3.1	slightly increasing	no	–	1.8	0.3
9114+9115	+12	C2.3-ERU	slightly increasing	yes	before	0	7
9393+9394	+20	X1.7	increasing (positive)	yes (small)	before	1	8.5
9415	−22	X2.3	constant	yes (great)	before and after	1.7	0.7
10030	+18	X3.0	increasing	yes	before	5	7
10030	+18	ERU	increasing	yes (great)	after	5	7
10069+10077	−8	M5.2-ERU	increasing	yes (great)	after	4	4.3
10162	+25	ERU	constant	yes (small)	before	9	0
10229	+15	M2.7	decreasing	no	–	0.2	3.5
10365	−6	M1.6	increasing	no	–	4.5	0.5
10365	−6	X1.3	constant	yes	after	4.5	0.5

.

Figure 2.18: *Table2: Characteristics of the active regions, halo CMEs and analyzed relevant eruptive events.* [a] *TMF: trend of the magnetic flux.*[b] *HC: Helicity change (slope of the curve).*[c] *TC: Time of change relative to the CME occurrence.*

2.5 Discussion

The role of magnetic helicity evolution in active regions producing eruptive events is considered to be very important and it is believed that the accurate measurement and modeling of the magnetic helicity is essential to understand the coupling between the photosphere, the corona and the heliosphere.

The study presented here was aimed at determining the temporal variations of magnetic flux and magnetic helicity injection in a sample of active regions generating halo CMEs, and how these variations could possibly be correlated with the CME occurrence.

We investigated the evolution of magnetic flux, magnetic helicity injection rate, and total magnetic helicity injection for ten active regions leading to twelve halo CMEs.

As a general result, we can deduce from the graphs shown in Figures 2.14 - 2.15 and Figures 2.16 - 2.17 and from Table 2.18 that there is no unique behavior in magnetic helicity injection accompanying halo CME occurrence. In fact, in some cases there is an abrupt change in H_i correlated in time with the CME event (see, e.g., NOAA 8858, 9415, 10030 [second CME], 10069+10077, 10365 [second CME]), in others there is a slight change in the curve slope (NOAA 9114+9115, 9393+9394, 10162), and in some no significant variation

is recorded (NOAA 8948, 10229, 10365 [first CME]). Therefore we cannot infer a general rule from this analysis.

We can, however, try to determine what conditions could give rise to these different behaviors and we discuss some possible relationships between the parameters characterizing the sample of ARs we analyzed.

A first conclusion that is possible to draw from the graphs shown in Figures 2.14 - 2.15 and Figures 2.16 - 2.17 is that the presence (or absence) of an abrupt change in H_i cannot be ascribed to the fact that the CME is gradual or impulsive: we actually found these changes in both classes (even if the most conspicuous H_i variations are associated with impulsive CMEs).

Nevertheless, an interesting result that can be deduced from the analysis of the total magnetic flux concerning the two classes is that the latter remains almost constant or shows a very slight increase for all the ARs that give rise to gradual CMEs, while it is significantly increasing or decreasing (with the exception of NOAA 10162) for impulsive CMEs. Moreover, on average the variation in helicity for the impulsive CMEs is more significant than for gradual CMEs. So the contribution in magnetic helicity injection due to flux emergence is quite significant also for more mature active regions, analogous to the results obtained by Tian et al. (2008) for new-born active regions.

In this regard, we recall that as already stated by other authors (see, e.g. Démoulin & Pariat (2009) and references therein), an increase of the magnetic flux, indicating the emergence of new flux tubes from the sub-photospheric layers, is the most important effect in causing the increase in the magnetic helicity flux. It is also possible that this emergence destabilizes the coronal magnetic configuration and leads to an eruptive event. On the basis of our results, we can conclude that this process was probably at work in some of the analyzed active regions, that is NOAA 9114+9115, NOAA 9393+9394 and NOAA 10030 (first CME), taking into account that in these active regions the change in magnetic helicity flux was observed *before* the CMEs. Note that these CME events are associated with X-class flares or erupting filaments.

Another effect, which causes a change in magnetic helicity flux *after* the CME, is

related to a possible lack of torque balance between the subphotospheric and the coronal domain of a flux rope, which can occur once the CME has removed the accumulated stress in the magnetic field (Longcope & Welsch (2000), Chae (2003), Pevtsov et al. (2003), Pevtsov et al. (2008)).

The imbalance of magnetic torque can induce a transfer of helicity from the convective zone below the active region by torsional Alfvén waves, which is present until the coronal field has a torque large enough to balance the sub-photospheric torque.

Our analysis indicates that the observed change in the magnetic helicity flux occurred after the CMEs could be ascribed to this process for NOAA 8858, NOAA 9415, NOAA 10030 (second CME), NOAA 10069+10070 and probably also for NOAA 10365 (second CME).

However, in some of these cases, a flux emergence process also occurs, so it is not possible to state definitely what the main mechanism at work is. What we can notice from the trend of H_+ and H_- is though that for some of the active regions just mentioned these parameters show an alternate trend. In these active regions the cancellation of magnetic helicity should be taking place. Therefore it would be worthwhile to extend this study to other active regions that show a change in the magnetic helicity flux after a CME to obtain further information on this process.

Concerning NOAA 8948 and NOAA 10229, both characterized by decreasing magnetic flux and no change in the magnetic helicity trend both before and after the CME, we recall that also the photospheric shearing motions can be responsible for increasing the stress in the magnetic field. However, the new, less energetic configuration reached by these active regions after the eruptive events was probably not characterized by a torque imbalance as in the other cases. Interestingly, both events are associated with M-class flares, while the majority of the events quoted in the second category (i.e., those associated with the torque unbalance) are associated with X-class flares (characterized by a higher energy output than M-class flares) or with erupting filaments, whose expulsion could greatly change the coronal magnetic configuration of the active region.

Another interesting result concerns the hemispheric helicity rule, which implies that

H should be negative for ARs in the Northern hemisphere and positive for those in the Southern hemisphere Seehafer (1990). Figures 2.14 - 2.16, Figs. 2.15 - 2.17 and Table 2 show that the analyzed ARs have a helicity accumulation in agreement with this rule, with the exception of NOAA 9415 and NOAA 10030 (showing both positive and negative H_i values during the analyzed time interval), 10069+10077 (showing negative helicity) and 10162 (characterized by positive helicity). Therefore 4/5 of the active regions of Class I have a helicity accumulation in agreement with the hemispheric helicity rule, while 3/5 of the active regions associated with impulsive CMEs seem to be related with an exception to this rule.

In conclusion, this study showed that magnetic helicity accumulation in our sample of active regions generating halo CMEs can exhibit significant changes when there are indications of new magnetic flux emergence. This emergence can change the helicity injection rate and also destabilize the coronal magnetic configuration, leading to an eruptive event.

Significant changes of the helicity injection rate can apparently also occur without the involvement of magnetic flux emergence. In most of these cases the observed changes follow the CME events and can be attributed to a process of restoring a torque balance between the subphotospheric and the coronal portion of the flux tubes.

Finally, we emphasize the result concerning the magnetic helicity injection with alternating sign found in those active regions where a considerable change of magnetic helicity was found, that was correlated in time with the CME occurrence. As in these active regions a cancellation of magnetic helicity should take place, we plan to further investigate this process both in these ARs as well in others, where a similar trend could be singled out.

2.6 Future Work

In our sample, we have dealt with active regions that emerged in the solar atmosphere during the solar maximum of the 23rd Solar Cycle. It would be interesting to investigate also those events that occurred during the solar minimum, so that we can obtain more general conclusions. Moreover, we plan to analyze a larger time interval (not just a day

before and a day after the eruption), so that we can follow the active region from its emergence till its decay.

It would be important to analyze data with the highest image resolution in order to be able to recognize smaller velocity fields, which nevertheless can change the magnetic structures in a slow but continuous manner. This additionally highlights the importance of getting images at short time cadence, so as to be able to follow in detail the evolution of the magnetic field in different levels. For this reason, we plan to analyze data acquired by HMI/SDO that can provide images similar to MDI but with higher resolution. Moreover, in the next future, the Solar Orbiter is expected to provide simultaneously images from the solar wind, the photosphere and the corona, that will complement our computations, or vice versa our computations will give results that could be more consistent with the observed data.

Note: the material presented in this chapter has been published by Astronomy and Astrophysics (Smyrli et al. (2010)) with A. Smyrli, F.Zuccarello and S. L. Guglielmino of the University of Catania(Italy), P. Romano and D. Spadaro of the INAF-Catania Astrophysical Observatory (Italy), F. P. Zuccarello of the Centre for Plasma Astrophysics in Leuven (Belgium) and with A. W. Hood and D. Mackay of the Institute of Mathematics in University of St. Andrews (Scotland, U.K).

Chapter 3

Computational Study of the Magnetic Helicity Inside a Convective Cell

"When you set out on your journey to Ithaca,
pray that the road is long,
full of adventure, full of knowledge.
The Lestrygonians and the Cyclops,
the angry Poseidon – do not fear them:
You will never find such as these on your path,
if your thoughts remain lofty, if a fine
emotion touches your spirit and your body.
The Lestrygonians and the Cyclops,
the fierce Poseidon you will never encounter,
if you do not carry them within your soul,
if your soul does not set them up before you."
Konstantinos P. Kavafis, **"Ithaca"** (1911)

3.1 Introduction

One of the most fundamental properties of the Sun is its magnetic field. It is the basic precursor for a large number of important energetic phenomena including Space Weather and geoeffective events (Zhang et al. (2003); Dmitriev et al. (2005) Bothmer & Daglis (2007)) such as Coronal Mass Ejections (e.g. van Driel-Gesztelyi et al. (2002b); Zhou et al. (2003); Zhou et al. (2006) and Schmieder (2006)) and Flares (as for example the commonly studied case of the X 17 solar flare of 28/10/2003, presented by Schmieder et al. (2006); den (2008) and Zuccarello et al. (2009)). Consequently, a significant effort is made to understand the origin of the solar magnetic field through the analysis of both observational data and numerical models. The origin and evolution of the magnetic field on the solar surface depends on a variety of large and small-scale subsurface fluid flows, which eventually constitute the solar dynamo mechanism. One such flow is the thermally-driven turbulent convection, the main energy transport mechanism, in the Sun's internal layer from $\sim 0.713\ R_{\odot}$ (Christensen-Dalsgaard et al. (1991)). The plasma flows that take place in the convective zone lead to the spatio-temporal evolution of the photospheric and coronal magnetic field. Therefore, interpreting the magnetic field transport throughout the solar interior and its injection across the solar surface through turbulent convective motions can be a key element in understanding the basic properties of the observed solar activity.

Solar convection is in a highly turbulent state, with a very large Reynolds number (the flux freezing assumption is valid) and is directly observable in the photosphere where it takes the form of a pattern of cells. Each cell is characterized by a bright central area, where hot plasma rises and by dark borders where downflow of plasma occurs (Figure 3.1). Taking into account the life-time and the length scale of the convective flow pattern, it seems that we are dealing with a multiscale convection at the solar surface and we can distinguish i) **the granulation** with typical diameters of $0.7 - 1.5$ Mm and a life-time of $5 - 10$ min, ii) **the mesogranulation** with a length scale of 5 Mm and a life-time of a few hours (but its existence remains a source of debate for many solar physicists such as Wang et al. (1989), Chou et al. (1991), Hathaway et al. (2000) or Rieutord & Rincon

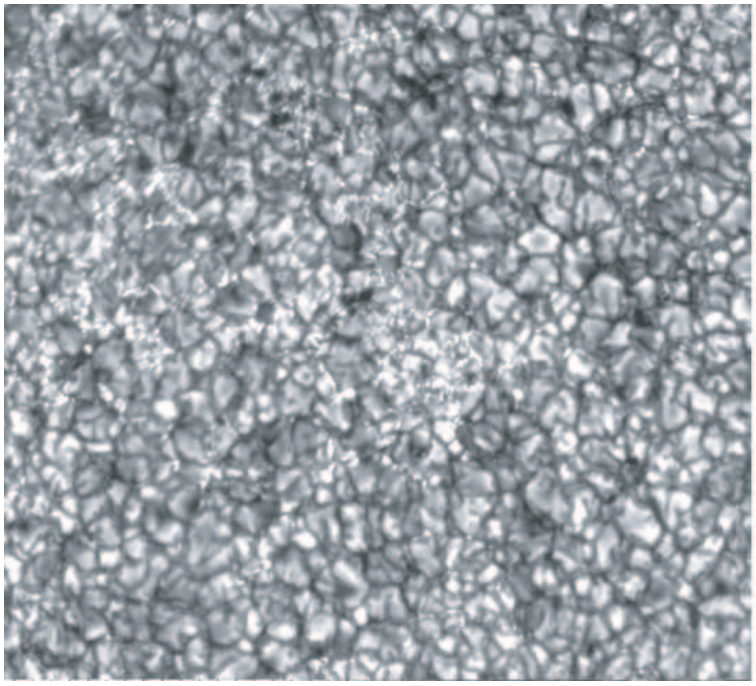

Figure 3.1: *Image of the solar granulation, where white areas represent hot rising flux and dark areas cold sinking motions of fluid. The image was acquired by G. Sharmer at the Swedish Solar Telescope on 10 July 1997.*

(2010) and iii) **the supergranulation** with a life-time of $1-2$ days and a length scale of $22-50$ Mm. Commonly, granular and mesogranular structures are advected by the large supergranular flow (Leighton (1964); De Rosa & Toomre (2004)).

From the above mentioned network patterns, the latter seems to be of particular interest since magnetic concentrations are observed at the boundaries between supergranules. Solar supergranulation has been observed (Leighton (1964); Zwaan (1978); Tarbell et al. (2000); Shine et al. (2000)) to accumulate vertical magnetic field in the adjacent regions between supergranules by a strongly converging and downward flow. As a result, magnetic elements of either polarity and strength are swept away from the centre of a cell (including also granular and mesogranular structures), being advected to the vertex more than any other location of the supergranular boundary (Figure 3.2), and an intercellular network is formed. Parker (Parker 1963) was the first to confirm the compression and enhancement

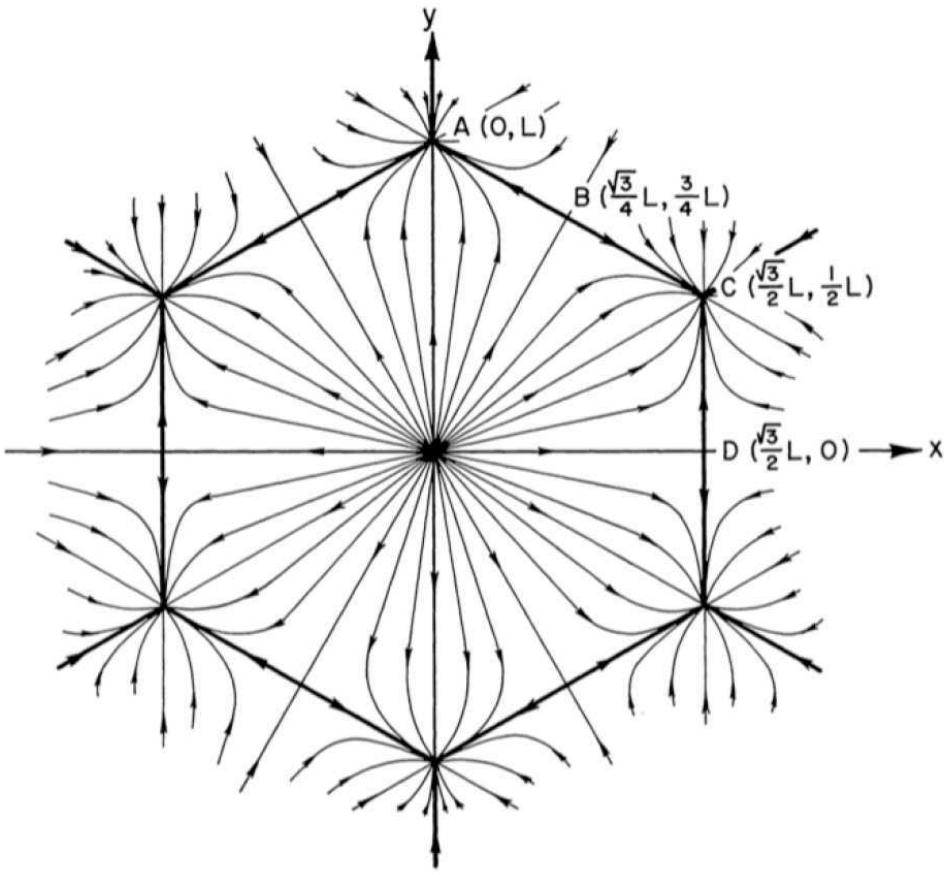

Figure 3.2: *Sketch of the horizontal motions at the top of a supergranule, as discussed in Clark & Johnson (1967)*

of magnetic fields at the neighboring boundaries of supegranular cells.

Such dynamic behaviour of the supergranular flow provoke a "channeled" magnetic field that enhances the rates of heating of the higher layers and the so-called **network** (Schrijver et al. (1997); Hagenaar et al. (1999)) appears. As was first discovered by Simon and Leighton (Simon & Leighton 1964) this can be recognized as bright emission when using spectral lines sensitive to magnetic activity such as the overlying chromospheric emission network observed in Ca II H. Images that use the emission in the $CaIIH$ line as a proxy for the photospheric magnetic field show bright points (**Network Bright Points, NBP**) concentrated on the junctions between supegranular cells (Figure 3.3).

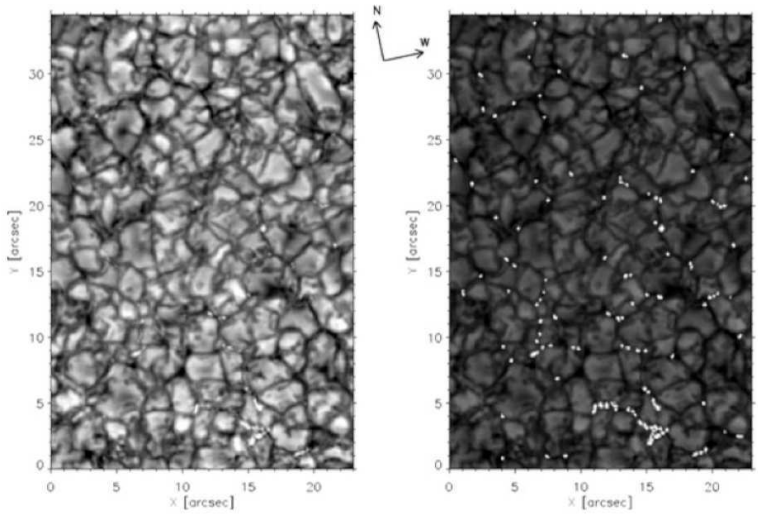

Figure 3.3: *Images of a quiet-Sun internetwork region observed at the centre of the solar disk with the Swedish Solar Telescope. The region was observed by Sánchez Almeida et al. (2004) through a 10.8 Å wide filter centered in the G-band. The two images correspond to the same snapshot but the second one has lower contrast and the position of bright points has been marked in white.*

The dynamics of these small scale elements are being examined in detail since they can play a role in the exchange of energy between the photosphere, the transition region and the corona. In good seeing conditions, we can observe inside the network the so-called **internetwork (IN)**: mixed polarity fields with very small strength (between 5-500 G) with a $1 - 4$ Mm size and a lifetime of less than 12 min (Harvey (1971); Lin (1995); Nisenson et al. (2003); Lites et al. (2008)).

Concluding, magnetic flux concentrations of a strength of around 10^{19} Mx, emerge intermittently as bipole pairs in the internetwork and then drift apart, following the supergranular convection pattern flow. Subsequently, they interact with already existing network elements (Hagenaar (2001); Schrijver et al. (1997)). However, that is not the case for larger magnetic flux tubes (with strength higher than 10^{19} Mx) as they are rooted deeper in the convective zone.

As far as the observation of supergranular convective flow is concerned, **doppler imag-**

ing, **local helioseismology** (as done by Hirzberger et al. (2008)) and tracking methods, such as the **Local Correlation Tracking (LCT**) the **Coherent Structure Tracking (CST)** and the **Ball Tracking (BT)** techniques, are often used to determine characteristic properties of the supergranulation (see the review on supergranulation by Rieutord & Rincon (2010))

From the above mentioned, it is obvious that the turbulent fluid motions occurring inside supergranular cells are continuously evolving the magnetic configuration. The influence of turbulent fluid motions on magnetic flux tubes can result in twisted and sheared magnetic field configurations and can lead to the heat of the higher layers of the solar atmosphere and consequently, an activity observed in the corona can be strongly related to the strong supergranular flows. The footpoints of numerous individual field lines interact inside the supergranular cells. They change their topology by reconnection, thus leading to instabilities and contributing to a transport and evolution of the magnetic flux in the solar corona. Subsequent energy build up and release can trigger events such as flares and CMEs. It is therefore extremely important to understand the processes occurring in supergranules in order to create an accurate model of the global solar surface magnetic activity.

It is the purpose of the work presented in this Chapter to investigate the emergence of bipolar regions inside supergranular cells and to describe their horizontal transport due to supergranular flows. Calculations related to the magnetic helicity trend that accompanies supergranular flow will then be carried out. The case considered in detail is an idealized one of a hexagonal cell that is considered as a single unit of the global supergranular network. We calculate how the two-dimensional motion of simple bipolar magnetic features, inside the hexagonal cell and along its boundaries, contributes to the accumulation of magnetic helicity. First, we consider a single bipole and a variety of different angles of emergence between the positive and the negative concentrations. Secondly, we consider more than one bipole inside the supergranular cell so as to let a variety of different process occur. The results show that magnetic helicity tends to accumulate in large amounts for the case of strong shear motions between magnetic polarities.

This Chapter is ordered as follows. The model set up and the computational technique are given in Section 3.2. Before considering a hexagonal cell, we run some computations for a single bipole moving inside a square box and analyze the results in Section 3.3. The emergence of a single bipolar pair inside a hexagonal cell is introduced in Section 3.4. A brief discussion on the build-up of magnetic helicity due to different motions between the two magnetic concentrations of opposite polarity is given in Section 3.5. The insertion of multiple bipolar pairs at random locations inside the hexagonal cell is briefly described in Section 3.6. In Section 3.7, we conclude by summarizing the significance of the results.

3.2 Model Set Up

The aim of this work is to study the build up of magnetic helicity due to different processes that occur inside a supergranular cell and lead to the evolution of the magnetic carpet (Figure 3.4):

* **flyby or advection** (two polarities are moving relative to one another without any interaction between them).
* **flux emergence** (two magnetic elements of opposite but equal amounts of flux appear as pairs simultaneously). The emergence of new flux occurs in most of the cases in the centre of the cell, related to the strong convective upflow.
* **flux cancellation** (two magnetic concentrations of opposite polarities move towards each other and disappear, following the original definition of (Martin et al. 1985)).
* **coalescence** (two polarities of the same sign move towards each other and merge into a larger polarity). Cancellation and coalescence occur usually at sides and near the vertices of supergranular cells.
* **fragmentation** (a large magnetic concentration splitting into two smaller polarities). The larger the flux concentration the more likely fragmentation is to occur.

The following procedure is applied to produce the horizontal motion of magnetic concentrations inside a supergranule:

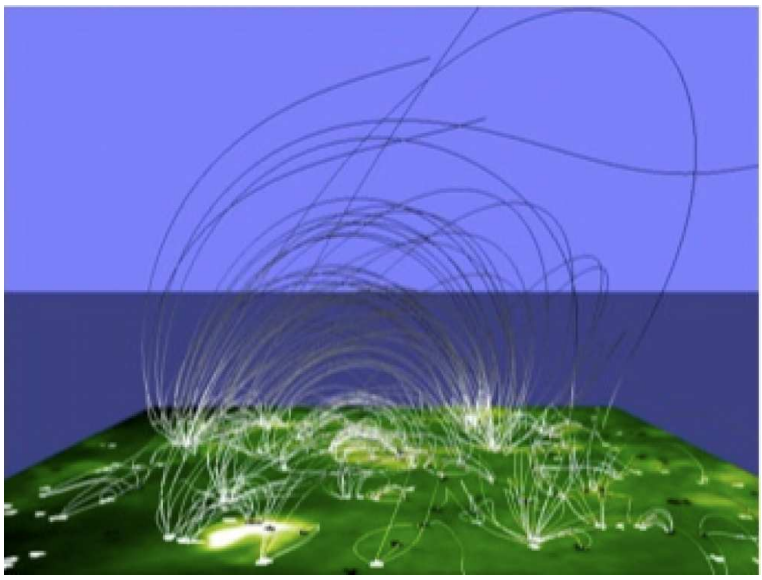

Figure 3.4: *This image is a model of magnetic fields at the surface of the Sun: the "magnetic carpet", developed using data from several instruments on board the ESA/NASA Solar and Heliospheric Observatory (SOHO) spacecraft, obtained from the Solar Oscillations Investigation's (SOI) webpage*

1. Initially, we define the domain of our computations. We use a box of 256×256 grid points and a 0.129 arcsec/pixel resolution. We choose this resolution so as to represent an area in the centre of the solar disk that covers around 24 Mm (23.942 km $\times$ 23.942 km). The whole size of the computational box is set to unity.

2. The coordinate system is cartesian. Accordingly, the scaled length of the x- axis is 0 and 1. The same scaling is used for the y- coordinates.

3. Next, we insert the hexagonal cell inside the computational box, by defining its centre, its length and the position of its vertices. Moreover, we define the middle points along its sides so that we can define the motion of magnetic features along them. The simple geometrical properties of a hexagon, allows us to define all of its points when we know its length and its centre coordinates as seen in Figure 3.5. For example, the x-coordinate of the position of the middle point M_{12} that is lying between the vertices V_1 and V_2 , will be $M_{12x} = x_0$ and its y-coordinate will be

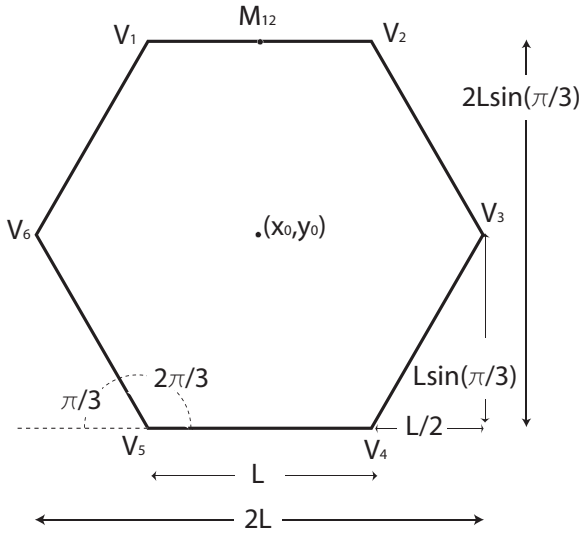

Figure 3.5: *A Hexagonal Cell with length L. The geometrical properties of the hexagon allow us to define easily the location of its vertices and the middle points between two vertices.*

$M_{12y} = y_0 + L * \sin(\pi/3)$. The centre of the hexagon coincides with the centre of the computational domain, i.e $(x_0, y_0) = (0.5, 0.5)$. The length of the hexagonal cell is taken to be L=0.3. This corresponds to a diameter of ~ 14 Mm in accordance with typical values given for the diameters of supergranular cells (Parnell (2001); Mackay et al. (2002)). Observationally the exact size of the supergranular cell has not been uniquely determined because it depends on the technique used. For example when the flows obtained by the MDI data are used, a length of 12-20 Mm (i.e De Rosa & Toomre (2004)) is estimated. In contrast, when the maximum of the power spectrum that corresponds to the line-of-sight velocity is used, a length scale of a supegranular cell lies in the range between 20 and 63 Mm (Hathaway et al. (2000); Hathaway (2004)).

4. We force the emergence of magnetic features in the interior of the hexagon, by creating a smaller square box with size $l = L/2$ (Fig. 3.6 (a)) that shares a common centre with the surrounding hexagonal cell.

5. Insert the magnetic concentrations. For each polarity we need to define the following characteristics :

   * **Shape**. Every magnetic feature in our computations is considered to be circular and the polarities remain circular throughout the whole computational period.

   * **Magnetic flux**. We assume that each magnetic polarity follows a Gaussian profile, as it can be seen in Fig.3.6 (b), where :

$$\mathbf{B}_z = \sum_{i=1}^{N} \mathbf{B}_{zi}\, exp(-(\mathbf{r}_i)^2/(r_0)^2) \tag{3.1}$$

   where N is the number of polarities and hence N/2 the number of bipoles, $\mathbf{r}_0 = L/10$ is their width. The location (x_i, y_i) is defined by the indexes that represent each grid cell and $\mathbf{r}_i = (x - x_i)\hat{i} + (y - y_i)\hat{j}$. A peak strength of $B_0 = \pm 100$ G (for the positive or negative polarities respectively) is considered.

   * **Location of the bipole**. We define the initial coordinates for the positive and negative magnetic concentrations (x_1, y_1), (x_2, y_2) respectively.

   * **Flow Profiles** for each polarity. In order to represent the motion of the magnetic features we need to set up a flow field $\mathbf{U} = (U_x, U_y)$. This flow field is used to move the magnetic sources so that for $t = t_0 = 0$ we get $x_i = x_{i0}$ and $y_i = y_{i0}$ and for $t = t_i$ we get $x_i = x_{i0} + U_x(t_i - t_0)$ and $y_i = y_{i0} + U_y(t_i - t_0)$. We assume that the velocity fields inside a supergranular cell can be described by just surface flows along the horizontal plane (U_x, U_y). As far as the vertical component of the flow field is concerned, U_z, it is proven from observations using mainly Doppler velocity maps to be rather small (e.g. Giovanelli (1980); Wang & Zirin (1988); November (1989); Hathaway et al. (2002); Duvall & Birch (2010); Rieutord & Rincon (2010)). At the vertex of the cell we assume zero velocity, and so each hexagonal corner is a stagnation point. We require the magnetic field to be swept to the supegranular boundary by implying for each magnetic fragment a radial motion (with respect to the centre of the cell) toward the boundaries and later along the boundaries towards the nearest vertex. When a polarity

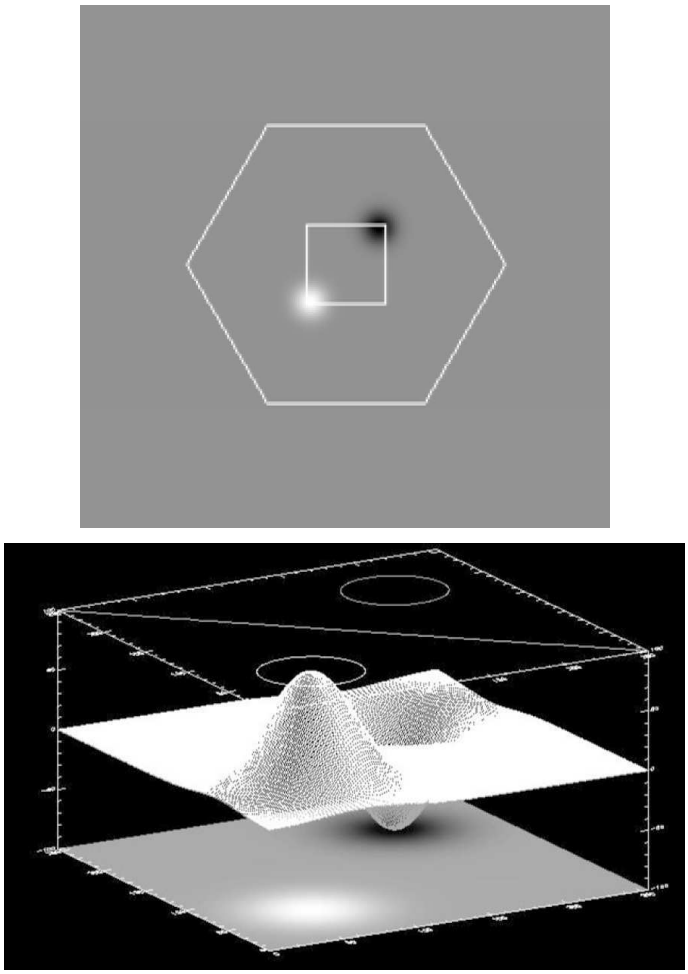

Figure 3.6: *(a) Representation of the relative sizes in the whole computational domain: the hexagonal cell, the smaller square box where bipoles are inserted and each polarity; (b) Gaussian profile of the magnetic field for each polarity, appearing on the bottom of the box as white and black circles.*

reaches the hexagonal cell side, it moves towards the closest vertex. As a result, the flow can be initially considered as a common diverging motion of all the magnetic concentrations away from the hexagonal centre and eventually as a converging flow towards any of the six vertices (Figure 3.2). There have been different values proposed for the horizontal flow velocity, obtained from various observations and/or computations, including its dependence on the flux that a

magnetic feature carries (Parnell (2001)), and its position inside a supergranular cell and along its boundaries. For examples see (Leighton et al. 1962), (Simon et al. 1994), (Hagenaar et al. 1999), (Hagenaar 2001), (Simon et al. 2001b) and (Priest et al. 2002). Consequently, there is a range for the typical speeds for magnetic concentrations between 0.03 and 4 km/sec. In our simulation we use a value of 0.5 km/sec.

* **Duration** of the computational run. We fix the total number n of time steps to be $n = 800$, where each step corresponds to $dt = 0.5$ min. So the total computational time is 400 min (about 6.5 hrs). The typical observed lifetime of supergranules can exceed our computational time. Sometimes they are found to last for several days as De Rosa & Toomre (2004) have shown in their detailed study of the life histories of more than 6000 supergranular cells. Nevertheless, the main purpose of our computations is to be in accordance with a realistic supergranular length size (L) and a realistic flow field (U_x, U_y) inside the cell and this limits our choice for the time step dt. We therefore choose dt to be small enough so that we get results correctly resolved in time (if the time step is too large we do not correctly resolve the movement of the fragments). The number of snapshots used are chosen so that the polarities always reach the corners of the hexagonal cell.

3.3 Test Cases

Before dealing with complex flows of one or more bipolar pairs inside a hexagonal cell, we perform some simpler computations for the entire domain. We consider the motion of two magnetic features (either of the same or of opposite sign) inside the whole square box. We initially follow this procedure mainly for two reasons :

I) We wish to check the accuracy of our results while applying the code of Chae that is commonly used for observational data.

II) We want to have a clear idea how different interactions of magnetic features can

affect the magnetic helicity trend.

3.3.1 Application of the code of Chae

In our simulations we used the code developed by Chae (Chae (2001); Chae et al. (2004); Chae & Jeong (2005)), which we used during the observational research of Active Regions related to eruptive events (see Chapter 2). However, here we have the advantage that there is no need to correct for effects of differential rotation, diffusion and meridional flow, as in the case of real observational data. We assume that throughout the computation, our box remains at the same position which for simplicity is coincident with the centre of the disk of the Sun.

In order to apply in our simulations the code of Chae, previously used in the analysis of MDI magnetograms (see Chapter 2), we first run the code using exactly the same values for the computational box as for an observed magnetogram. This simplifies our calculations and excludes any possibility of error occurrence and false results. To demonstrate this, the values used for the computational domain are again 256×256 pixels and the resolution size is equal to 2 arcsec/pixel, so the numerical grid is a square of side 371200×371200 km^2 . This is done so that we are in accordance with the resolution of real full-disk, MDI line-of-sight magnetogram data.

We choose a number of 100 snapshots and a $dt = 30$ min as the time difference between them. This corresponds to 50 hrs computational run which is approximately 2 days and is consistent with the average number of days used in our observational data analysis (see Chapter 2). Moreover, at this first stage we choose to work with the simplest flow that can define the motion of magnetic fragments inside the domain. This is a uniform constant speed just along one dimension which can be for example the x-direction ($U_x = 0.5$ km/sec) with zero component on the y direction ($U_y = 0$). In that case, by varying the y-coordinate of the initial position of each polarity inside the box (x,y), we can describe different processes occurring between two polarities. For example, a cancellation of the two concentrations will occur, when they are placed opposite to each other (i.e. same y-coordinate) and they move towards each other. The magnetic field strength is set fixed

to $B_0 = 100$ G and the radius of the circular magnetic concentrations is chosen to be $r_0 = 0.15$, so that we can follow in detail their interactions and their influence on the magnetic helicity evolution.

We aim to demonstrate that we have successfully transformed the code developed by Chae into a useful and accurate method that we can apply to the computation of flows of magnetic concentrations inside a box and get trustworthy results to describe the trend of the accumulated magnetic helicity. We show that our computations give a correct value for the resulting vector potential **A** with the use of a Fast Fourier Method as presented in Chae (2001). For this we consider, $B_z(x, y)$ and set:

$$\mathbf{A} = (A_x, A_y) = \nabla \times (\Phi \hat{z}). \tag{3.2}$$

With this,

$$\nabla^2 \Phi = -B_z \tag{3.3}$$

and so

$$\frac{\partial^2 A_x}{\partial x^2} + \frac{\partial^2 A_x}{\partial y^2} = -\frac{\partial B_z}{\partial y} \tag{3.4}$$

$$\frac{\partial^2 A_y}{\partial x^2} + \frac{\partial^2 A_y}{\partial y^2} = \frac{\partial B_z}{\partial x} \tag{3.5}$$

using the Fourier solutions :

$$A_x = FT^{-1}\left[\frac{jk_y}{k_x^2 + k_y^2} FT\left(B_z\right)\right] \tag{3.6}$$

and

$$A_y = FT^{-1}\left[-\frac{jk_x}{k_x^2 + k_y^2} FT\left(B_z\right)\right] \tag{3.7}$$

where the Fourier transform of a function $A(x, y)$ is given as :

$$FT\left(A\right) = \sum_{x,y} A\left(x, y\right) \exp\left(-jk_x x - jk_y y\right) \tag{3.8}$$

In this way, we are able to calculate the value of B_0 and check if it has the correct value, i.e whether it is a gaussian function with a peak of 100 G. This is achieved by considering the equation that relates a magnetic field with its vector potential: $\mathbf{B} = \nabla\times\ \mathbf{A}$. Since from our calculations we compute the A_x and A_y components of the vector potential (we consider that the current that sustains the magnetic field is confined to the surface and hence A_z=0), we can derive the calculated component for B_0 in cartesian coordinates and check if its value is equal to the original defined $B_0 = 100$ G according to the equation:

$$B_z = \frac{\partial A_y}{\partial x} - \frac{\partial A_x}{\partial y} \tag{3.9}$$

More specifically, B_z may be expressed from the contribution of the spatial derivatives of its vector potential $A_{x,y} = (A_x, A_y)$ and so for each grid cell (i, j) of the computational domain it can be approximated with the use of the formulae on the previous $(i-1, j-1)$ and following (i+1,j+1) grid cells respectively :

$$B_z^{i,j} = \frac{A_y^{i+1,j} - A_y^{i-1,j}}{2 \times resolution} - \frac{A_x^{i,j+1} - A_x^{i,j-1}}{2 \times resolution} \tag{3.10}$$

Note the spacing between the $i+1$ and $i-1$ is two grid cells and so we have to divide by $2 \times resolution$.

As the calculations reproduced a magnetic field with peak strength very close to 100 G for each polarity and for each snapshot, we could verify that our computational technique gives accurate results.

We now examine the trend of the vector potential **A** of a Gaussian magnetic field **B**. In figure 3.7 we show the surface plots of the magnetic field of each polarity, when a 'fly-by' process occurs (described in detail in Section 3.3.2) for two different snapshots : at the beginning of the computational run ($t = 0$) and at the end ($t = 100$) where they end up on the corners of the computational domain. The peak value is as expected $\pm$100 G.

Specifically, we can examine the evolution of A_x and A_y along the y and x direction for each polarity. Since the magnetic field **B** is stronger on the centre of a magnetic concentration, we expect its vector potential to get maximum absolute values when approaching to the central part of the polarity. For example, let us estimate the behavior of A_y along

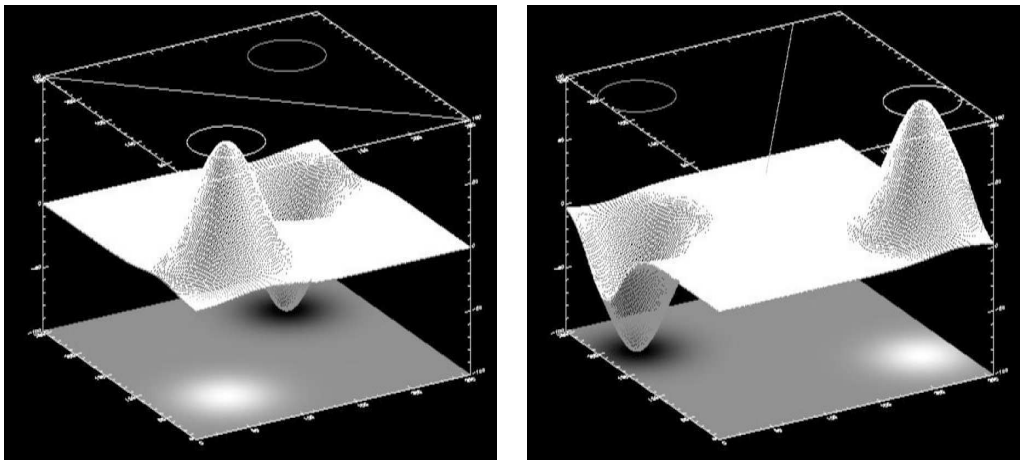

Figure 3.7: *Surface plots of the gaussian profile of the magnetic field for each polarity for the computational run that represents the "fly-by" process, at the beginning and at the end of the computational run.*

the x-axis for a positive polarity having its centre located at (x_i, y_i) (Fig. 3.8). Firstly, we expect very low values in any grid point not inside the radius r_0. Since we are dealing with a positive polarity, we want to obtain a Gaussian plot that gets a peak and is always positive. For this we require that the vector potential field is rotating anti-clockwise, and so the A_y will be directed downwards (i.e negative values) when we are approaching the polarity from its left side and upwards when we are moving away from the polarity towards higher values of x. The absolute value of A_y will be increasing as we are approaching the centre of the magnetic concentration from either side where it reaches a maximum. This means that we expect a rapid change in the point that corresponds to the centre of the polarity, since A_y is jumping from negative values to positive.

In Figure 3.9 we show the surface plots of the A_x and A_y components of the vector potential, for both the positive and the negative polarities, for the very first snapshot in the "fly-by" process. The centre of each polarity is the point where the surface plot changes rapidly and passes through zero.

Similarly, for the trend of A_x along y-axis and for a anti-clockwise rotation of the vector potential that gives a positive $\mathbf{B}$, we expect opposite behavior, as shown also by

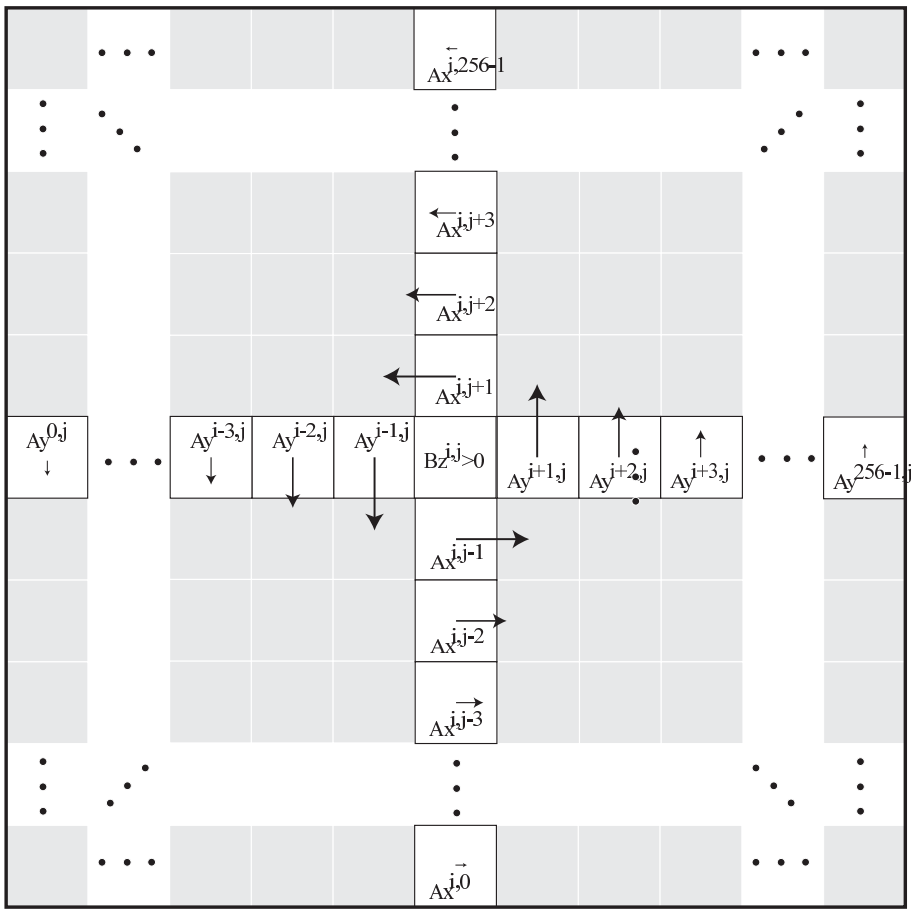

Figure 3.8: *Evolution of A_x and A_y along the y and x direction for a positive polarity located at (x_i, y_i) inside the computational domain (*256×256 *grid points).*

the '-' sign in equation (3.9), positive values of A_x for $y \leq y_{central}$ and negative values for $y \geq y_{central}$. Since the vector potential is strongest on $y = y_{central}$, the A_x will show rapid change so as to move from the highest positive value towards the highest negative value.

Figure 3.10 shows the vector potential profiles for A_y and A_x along the x and y direction respectively for the positive (top row) and the negative polarity (bottom row). The different type of lines (i.e solid, dashed, dotted etc) show the different evolution of vector potential for different $(x_{central}, y_{central})$ of the magnetic polarity with $B_0 = 100$ G. In that way, we obtain the simple spatial dependence of the vector potential for each polarity, avoiding any distortions from the interaction of magnetic flux between two features to enter in our

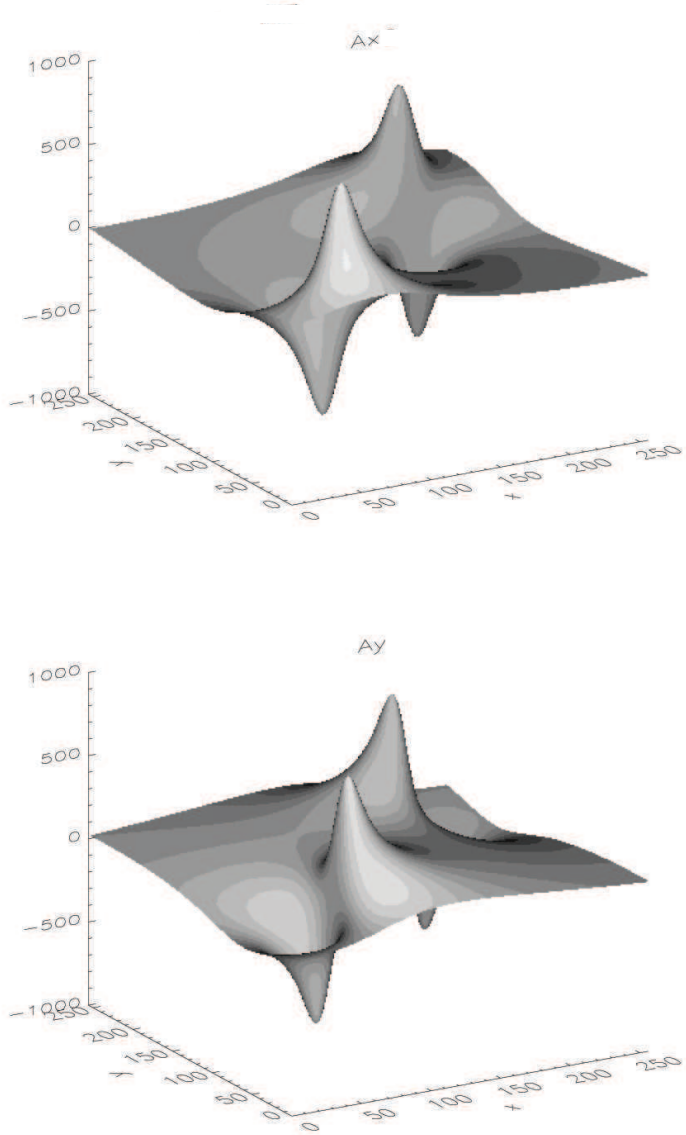

Figure 3.9: *Surface plots of the A_x and A_y component of the vector potential for the positive and the negative polarities for the first snapshot in the "fly-by" process. The centre of each polarity is where a rapid change in the plot is observed.*

calculations. The obtained plots seem to follow our predictions and the right-hand rule according to which the curl of a clockwise rotating field on (x, y) will give a negative field

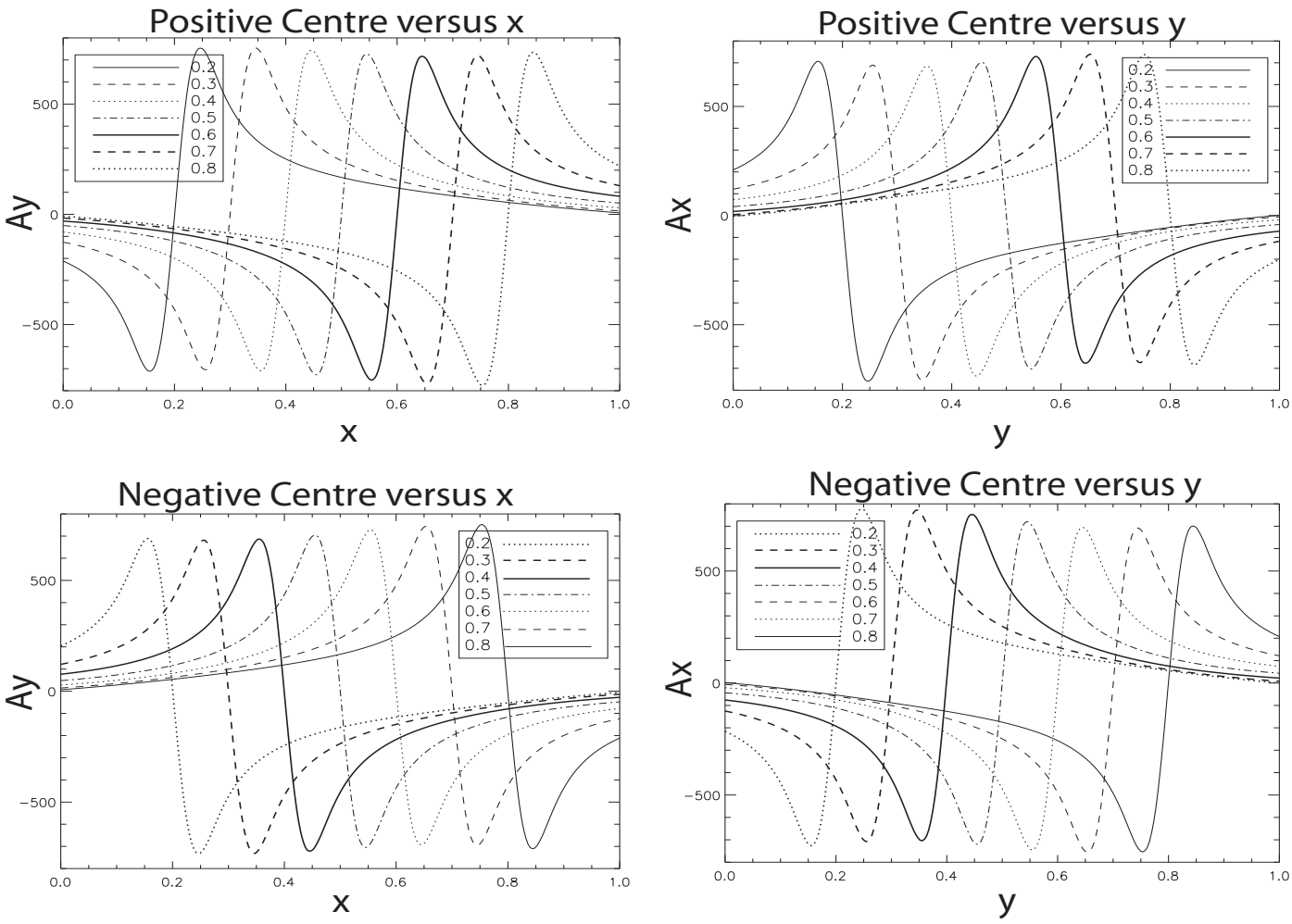

Figure 3.10: *Top row: spatial evolution of A_y and A_x (from left to right) along the x and y axis for the positive polarity. Second row: the same for the negative polarity.*

on the z-direction. This result confirms that our calculations are trustworthy enough and so we can move to the study of some simple flows of a bipolar pair inside the computational domain.

3.3.2 Study of different motions of a bipolar pair

We investigate the motion of two polarities inside a square box to get a general idea on how this motion can affect the pattern of magnetic helicity.

"FLY-BY" OR ADVECTION

In our first case, we consider two polarities of opposite sign with initial coordinates $(x_1, y_1) = (0.25, 0.25)$ and $(x_2, y_2) = (0.75, 0.75)$. The polarities are moving in opposite directions, so that at the midpoint of the computational run, they both pass at the central x-coordinate ($x_1 = x_2 = 0.5$) of the box. At this time, they have the minimum distance ($d = 0.5$) but the maximum relative shear between them. At this position, where the polarities get closest to each other, we expect a significant contribution to the evolution of magnetic helicity and consequently an important change in its accumulation. Snapshots for the computational run are shown in Figure 3.11.

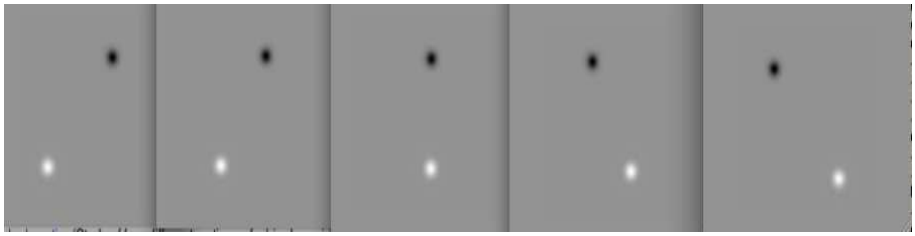

Figure 3.11: *Snapshots of the computational run that represents the* ***"Fly-by"*** *between two opposite polarities inside the computational domain (square box) with initial positions* $(x_1, y_1) = (0.25, 0.25)$ *and* $(x_2, y_2) = (0.75, 0.75)$ *respectively.*

The following Figures (3.12,3.13,3.14) show the magnetic helicity accumulation H_i between two times t_0 and t_i (where $H_i = \int_{t_0}^{t_i} \frac{dH}{dt} dt$, with t_0=0 defining the beginning of the computational run and t_i the final time step), the total unsigned magnetic flux Φ (with $\Phi = \Phi_{pos} + |\Phi_{neg}|$) and the magnetic helicity transport rate dH/dt in the first, second and third row respectively. The above parameters are expressed in 10^{40} Mx^2 (for the total injected helicity H_i), 10^{20} Mx (for the Φ) and 10^{40} Mx^2 hr^{-1} (for the dH/dt). Each column in Figures (3.12,3.13,3.14) corresponds to a different separation distance between the two polarities, starting from the maximum one in the left column of Figure 3.12 (i.e $y_1 = 0.25$, $y_2 = 0.75$) to shorter ones by re-defining their initial y coordinates (y_1 increases from each plot to the other by $dy = 0.05$ and the same happens for y_2 which gradually decreases by $dy = 0.05$). In

accordance with our expectations, the magnetic helicity accumulation increases as the initial separation distance between the two polarities decreases: the graphs in the first column of Figure 3.12 show the results for the maximum initial separation between the magnetic concentrations and we can see that the total accumulated helicity is significantly smaller than the value obtained in the graph of the second column of Figure 3.13 where the two polarities are closer ($y_1 = 0.40$, $y_2 = 0.60$). In both cases the total magnetic helicity accumulation is positive and this is related to the orientation of the relative motion of the two polarities. In our simulation the positive polarity is 'under' the negative and moves on the right whereas the negative is higher (on the y-axis of the computational box) and moves on the left. If we simply reverse the location (and consequently the velocity vectors) of the two polarities (i.e. positive higher than the negative and with a negative velocity), the absolute amount of magnetic helicity accumulation will be the same in value but negative. Hence, the sign of magnetic helicity depends on the orientation of the relative motion of magnetic fragments.

The diagram of the rate of change of magnetic helicity is observed to be almost symmetrical for all the cases and its peak occurs when the two polarities have the same x-coordinate and this can be connected either to the fact that the two polarities at this moment are closer to each other than in any other snapshot or that the component of velocity perpendicular to their joining line is maximum. More specifically, if we distinguish two components of velocity : one perpendicular and one along the line joining the two polarities, it results that the perpendicular component is the main responsible for the production of magnetic helicity. When the two polarities are far in the opposite corners of the box, there is also a component of velocity along their joining line, i.e. they are moving towards each other. This component gets lower when the two polarities approach the centre of the box and vanishes completely when they are located at $x = 0.5$; here the perpendicular component gets the maximum value and its influence in the build-up of magnetic helicity is greater. In other words, the small distance, the presence of a maximum perpendicular component of velocity and

the absence of motion towards each other, leads to the peak in the rate of change of magnetic helicity.

The decrease of total magnetic flux for the last two cases (Figure 3.13, second column and Figure 3.14), results from the vicinity of magnetic fragments of opposite sign into a distance that is less than their radius, and the subsequent cancellation of part of their magnetic fluxes. However, we note that the total magnetic flux for all the plots, even for the cases shown in Figure 3.12 where there is no cancellation, it is not constant. For example, in the first column of the Figure 3.12 the total magnetic flux is varying between 14.0210 and 14.0230 10^{20} Mx. We believe that this variable trend may be due to numerical errors.

To summarize the results obtained in the "fly-by" case, we can conclude that **the stronger the shearing motion, the larger the helicity injection.**

CANCELLATION

We now investigate the process of cancellation that was partially observed in the "fly-by" case and is characterized by the loss of magnetic flux in two encountering magnetic features that were initially isolated. A very first definition, gained through detailed observational analysis of videomagnetographs from the Big Bear Solar Observatory, of magnetic flux cancellation on the Quiet Sun (inside some well defined supergranular cells) can be found in the work of Livi et al. (1985). As far as a theoretical explanation to this process of loss of magnetic flux is concerned, there have been developed different models that either include the emergence of U-shaped loops through the photosphere or the submergence of omega loops across the photospheric boundary ((Zwaan 1978)). Parker ((Parker 1975)) proposed that for the latter case magnetic reconnection needs to occur above the photosphere so that the loop can overcome the magnetic buoyancy and submerge , whereas for the case of emergence of a U-loop, the reconnection is not a necessary condition. Recently, a very interesting observational analysis of G-band images of the Solar Optical Telescope on board Hinode, given by Kubo et al. (2010), highlights the importance of understanding the

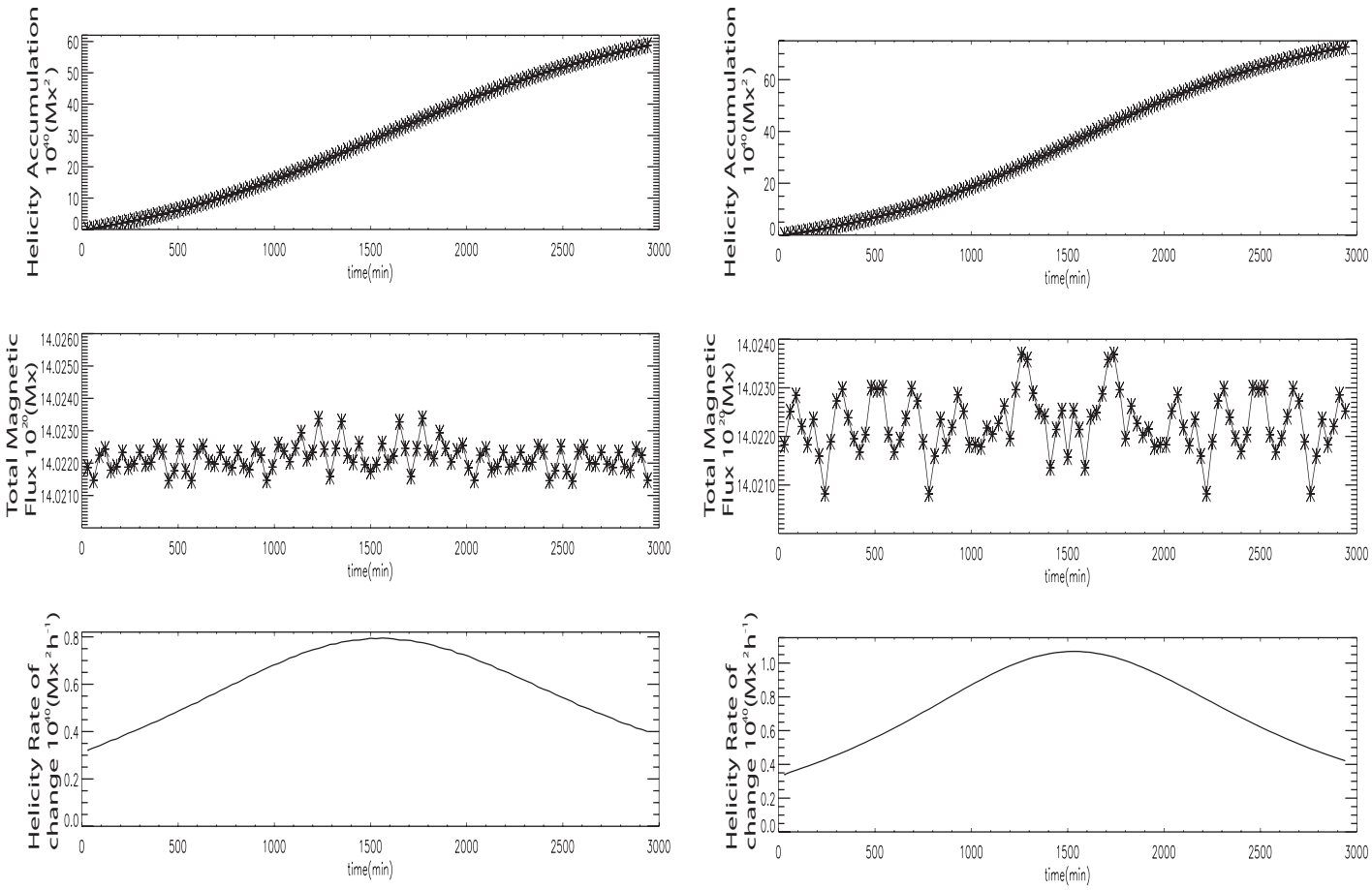

Figure 3.12: ***"Fly-by"*** *case. From top to bottom : evolution of the magnetic helicity accumulation H_i, total unsigned magnetic flux Φ and rate of change of magnetic helicity dH/dt for different initial positions of the positive and negative polarities* $(x_1, y_1) = (0.25, 0.25)$ *and* $(x_2, y_2) = (0.75, 0.75)$ *in the first column, and changing with a step* $dy = 0.5$ *in the second column, so that* $(x_1, y_1) = (0.25, 0.30)$ *and* $(x_2, y_2) = (0.75, 0.70)$.

role of subsurface convective flows into explaining the collision of opposite magnetic polarities.

The magnetic field distribution during different time steps in the run is shown in Figure 3.15. Here the initial position is at $x_1 = 0.25$ and $y_1 = 0.50$ and $x_2 = 0.75$ and $y_2 = 0.50$ for the centre of the positive and the negative polarities respectively.

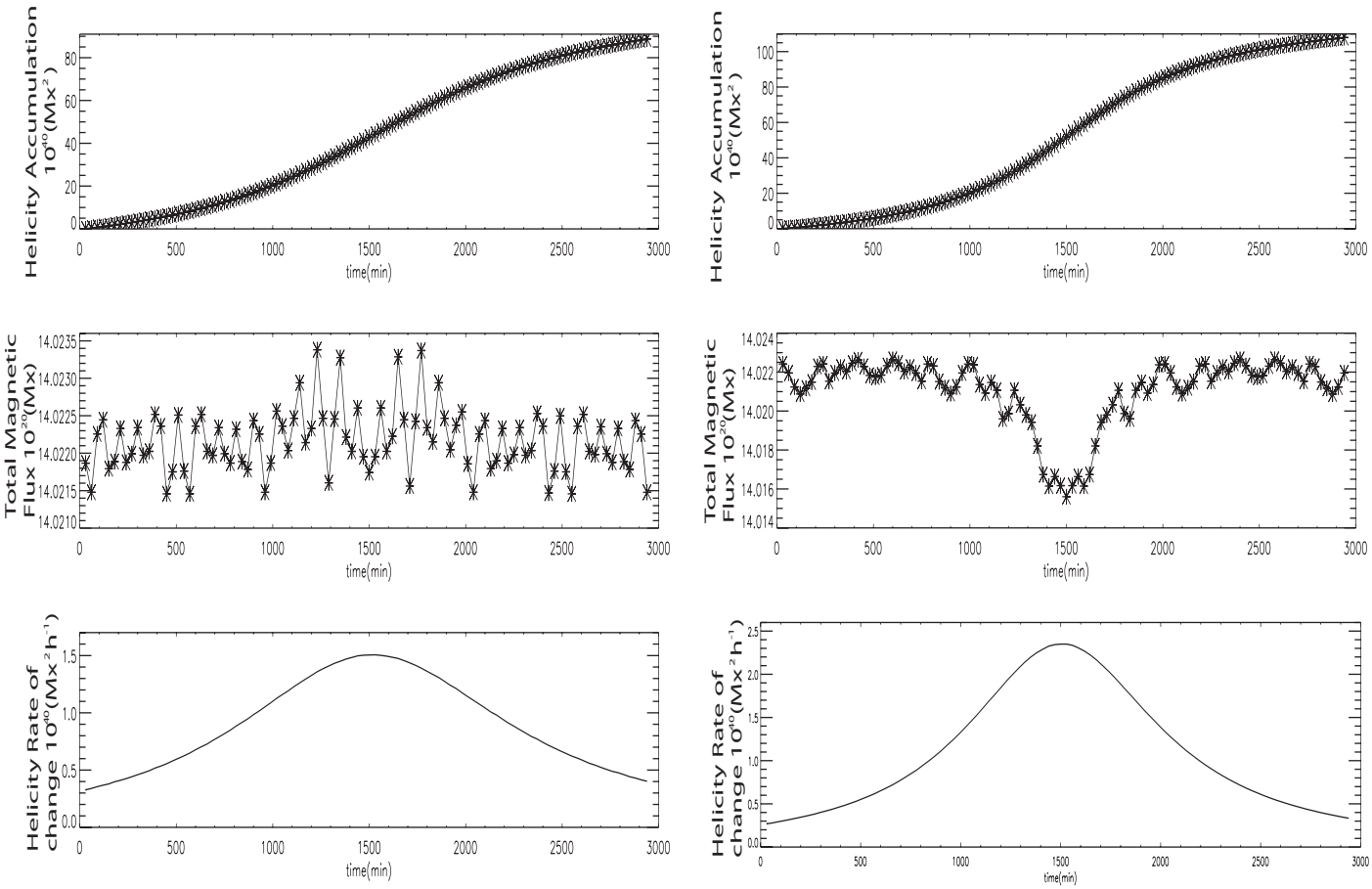

Figure 3.13: *Same as in Figure 3.12, but now the initial positions of the positive and negative polarities are* $(x_1, y_1) = (0.25, 0.35)$ *and* $(x_2, y_2) = (0.75, 0.65)$ *for the first column and* $(x_1, y_1) = (0.25, 0.40)$ *and* $(x_2, y_2) = (0.70, 0.60)$ *for the last column.*

We let the two opposite polarity magnetic fragments move with uniform horizontal velocity towards each other so that they eventually come into contact, they collide and they gradually disappear at the centre of the box. The plots of magnetic helicity accumulation, total unsigned flux and rate of change of magnetic helicity are shown in the Figure 3.16 (a). The plot that describes the accumulation of magnetic helicity is negative and this depends on the orientation of the two polarities. We can prove this by running one more computation where the positive polarity is on the right

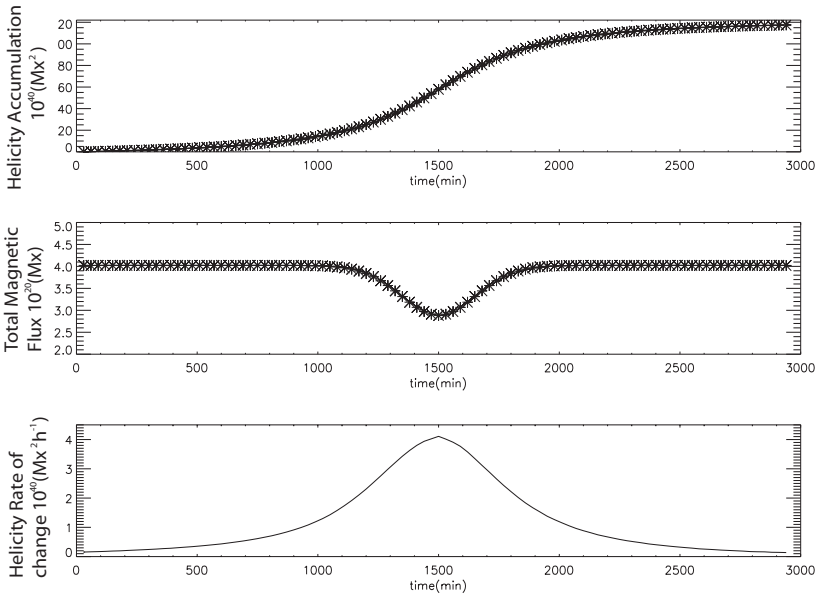

Figure 3.14: *Magnetic helicity accumulation H_i, total unsigned magnetic flux Φ and rate of change of magnetic helicity dH/dt, but now the positive polarity is initially inserted in the position $(x_1, y_1) = (0.25, 0.40)$ and the negative in $(x_2, y_2) = (0.75, 0.55)$.*

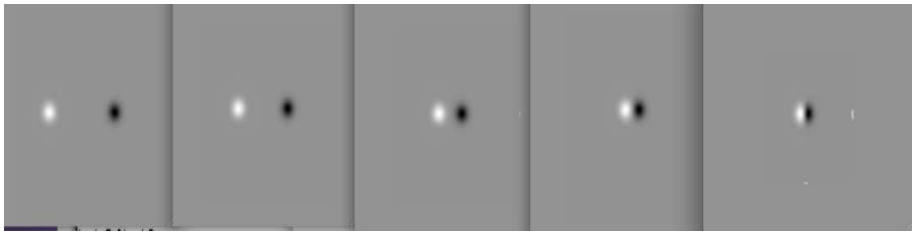

Figure 3.15: *Snapshots of the computational run that represents the* ***cancellation*** *process that occurs between two opposite polarities inside the computational domain with initial positions $(x_1, y_1) = (0.25, 0.50)$ and $(x_2, y_2) = (0.75, 0.50)$ respectively.*

side and the negative one on the left side.

As expected, we obtain positive values for the accumulated magnetic helicity, but with the same absolute value as before. The plot of the temporal evolution of the absolute total magnetic flux (third row) is in agreement with the definition of can-

cellation: at later times of the computational run, when the two opposite polarities encounter each other, there is gradual loss of magnetic flux till its disappearance. We note that the magnetic flux does not disappear completely (i.e the graph does not fall to zero) and this is connected to our computational technique since we decide to stop the run at one time step before the end ($nt - 1$) so as to avoid any problems that the code would have to face by the complete absence of magnetic field.

We note that both the plots that describe the magnetic helicity accumulation and the rate of change of magnetic helicity, give very small values compared to the "fly-by" case. The reason for this difference is because in this case the two polarities move straight away towards each other and at around the half of the computational time (i.e. when they approach the centre of the box), they already encounter and cancel each other. In contrast, in the 'fly-by' case the relative motion of the two polarities lasts for a longer period and thus affect significantly the build up of magnetic helicity. Moreover, the low production of magnetic helicity can be explained by considering the components of velocity perpendicular to and parallel to the line joining the two polarities. In contrast with the "fly-by" case, where the perpendicular component of the velocity contributes to high magnetic helicity production and when it gets a maximum value (i.e when one polarity is located above the other) results to maximum rate of change of magnetic helicity, here this component is completely absent, we have just the component parallel to the line joining them and thus very low generation of magnetic helicity.

Additionally, in Figure 3.16 (b), we present another cancellation process, but this time the two polarities are initially located at the opposite corners of the square, they move towards each other and they cancel at the centre of the square. The plots describe a situation where the two polarities are moving for longer period inside the box, since the cancellation of magnetic flux occurs some time steps later than in the previous case (Figure 3.16 (a)) and hence they produce higher amounts of accumulated helicity than in the first case. However, we note that these values are again small compared to the values obtained for the "fly-by" process.

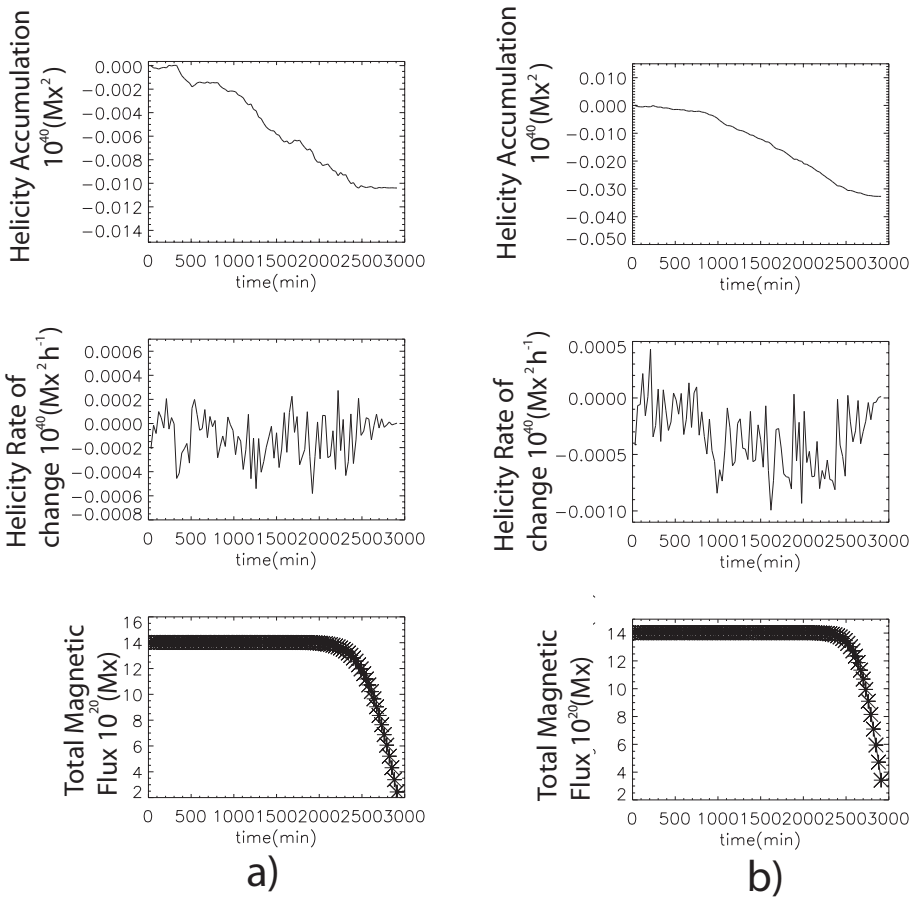

Figure 3.16: *From top to bottom: evolution of the magnetic helicity accumulation H_i, total unsigned magnetic flux Φ and rate of change of magnetic helicity dH/dt for the case of* ***cancellation****: a) two polarities move towards each other along the x-axis initially located at $x_1 = 0.25$ and $y_1 = 0.50$ and $x_2 = 0.75$ and $y_2 = 0.50$ and b) two polarities move towards each other initially located at $x_1 = 0.25$ and $y_1 = 0.20$ and $x_2 = 0.75$ and $y_2 = 0.75$.*

EMERGENCE

Here we consider a dipolar feature located at the centre of the box and consists of two separate and of opposite polarity concentrations. These concentrations they start to migrate towards opposite directions along the x-direction. The centre of the positive polarity is at $(0.40, 0.50)$ and the centre of the negative one at $(0.60, 0.50)$ so that at the beginning of this process they are in contact and they interact with

each other, but later they are moving apart, as two completely isolated magnetic concentrations. Figure 3.17 shows the amount of accumulated helicity H_i, the total unsigned flux Φ(with a sudden decrease at the end of the computational run due to the fact that the polarities reach the borders of the box and partially vanish) and the rate of change of magnetic helicity *dH/dt*. As previously found, the values for magnetic helicity flux are much smaller compared to the ones obtained in the 'fly-by' computations.

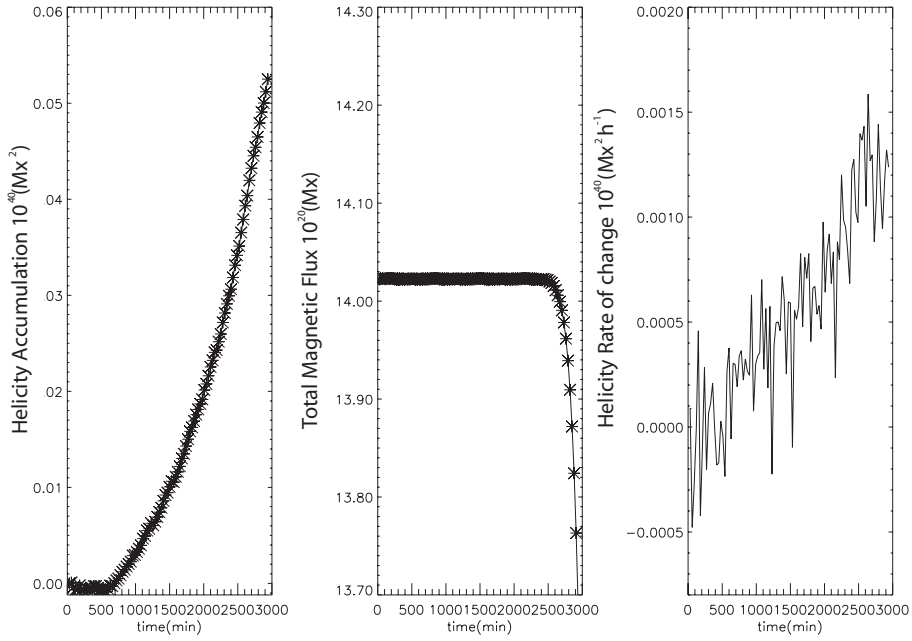

Figure 3.17: *From left to the right : evolution of the magnetic helicity accumulation H_i, total unsigned magnetic flux Φ and rate of change of magnetic helicity dH/dt for the computational case of* ***emergence****: two opposite polarities generated close to each other and gradually moving away from each other till their complete separation.*

COALESCENCE

We consider the same initial location and velocity direction for the two magnetic concentrations as in the computational run of cancellation. The difference is that now we are describing the flow of two magnetic features of the same polarity towards each other. Thus, a larger polarity (with $R = 2 * r_0$ that carries double amount of

flux) is observed to be created after some time at the centre of the computational box. Figure 3.18 shows the computed injection of magnetic helicity H_i, the total absolute magnetic flux Φ and the rate of change of helicity *dH/dt*.

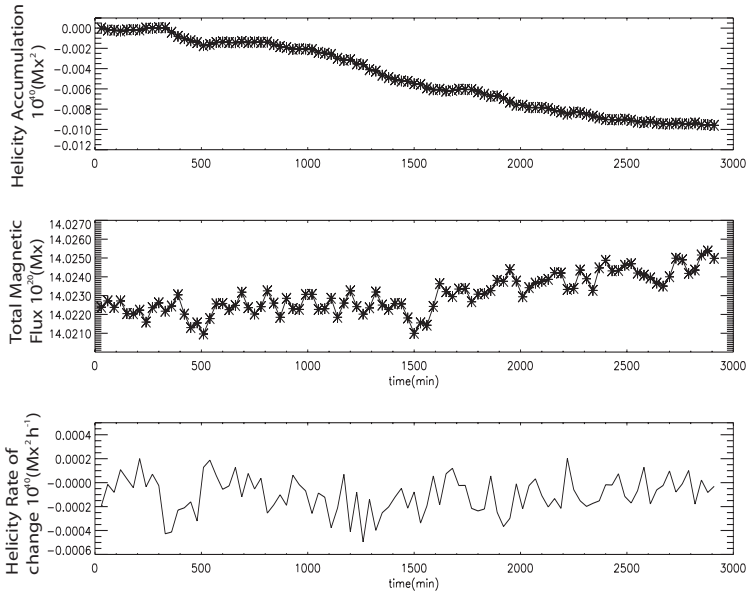

Figure 3.18: *From top to bottom : evolution of the magnetic helicity accumulation H_i, total unsigned magnetic flux Φ and rate of change of magnetic helicity dH/dt for the computational case of* ***coalescence****: two positive polarities move towards each other so that at the end of the computation they collide.*

Interestingly, we note that the resultant accumulated helicity by the end of the coalescence process is $H_i \sim -0.01 \times 10^{40}$ Mx^2, almost equal to the value obtained through the process of cancellation,but in the latter case we are dealing with a complete loss of magnetic flux.

This shows that the magnetic helicity depends on the orientation of the relative motions of the magnetic polarities and on characteristics of the shearing motion (i.e. whether their motion lasts for the whole computational run or for just half of it until the two polarities cover half the box and whether they are moving radially towards each other). If such an

assumption is correct, this confirms that magnetic helicity is an excellent parameter that can reveal how a flow can result to the knottedness and/or linkages of magnetic field lines depending just on the absolute value of the magnetic flux at their footpoints but not on their sign. The magnetic configuration can lead to the different events (such as cancellation or coalescence) but to same results in terms of production of magnetic helicity. We should be careful though not to arrive to general conclusions, till we reach a large number of computational runs that verify the above assumption.

FRAGMENTATION

Here two neighboring polarities of the same flux (we run our computation with positive polarities) that are initially placed close to the centre of the box and appear as a single polarity unit (of same sign and double amount of flux), start to separate and migrate towards opposite directions. As a result, at the end of the computation we have the two isolated magnetic features of the same sign far from each other. The analyzed plots for the magnetic helicity accumulation, for the total unsigned magnetic flux and the rate of change of magnetic helicity are shown in Figure 3.19. If we compare these results with the case of emergence of two opposite polarities (Figure 3.17, we see that the results are the same: by the end of both processes the accumulated magnetic helicity is slightly higher than 0.05×10^{40} Mx^2 and the plots that describe the rate of change of magnetic evolution seem to be identical. **Can we conclude that we have an example showing the independency of magnetic helicity on the sign of the magnetic field? Can we conclude that it is the common flow field of a whole system composed by the interaction of various mixed-sign polarities that is responsible for the build-up of magnetic helicity and not each magnetic polarity individually?** Once more, we should pay attention not to arrive to generalizations until we have a large number of examples that are in accordance with the above results.

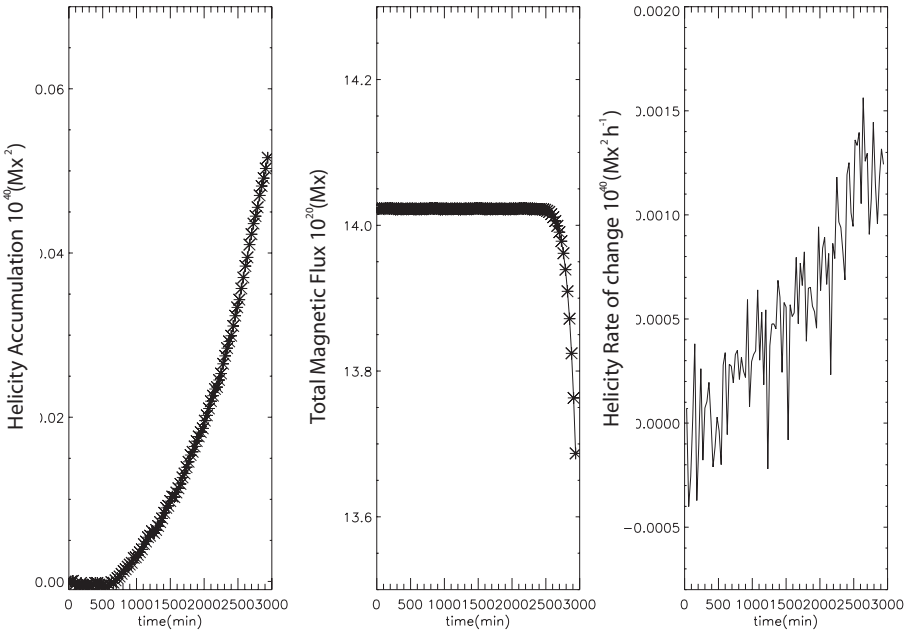

Figure 3.19: *From left right: temporal evolution of the same parameters as in the previous cases: H_i, Φ, dH/dt.* ***Fragmentation****: two positive polarities being located close to each other appear as a unit. Their velocities have opposite directions and after some snapshots, they start to separate and by the end of the computation they appear as two individual polarities.*

3.3.3 Summary of the Results

Our first study, concerning the motion of two magnetic polarities inside a computational square box, gives us some first indications about the evolution of magnetic helicity related to processes such as advection, cancellation, emergence, coalescence and fragmentation. From the case of advection, we realize that the magnetic helicity sign depends on the orientation of the motion of the two polarities. Moreover, we realize that the separation distance between the two magnetic fragments can influence the final amount of accumulated helicity. The smaller the distance, the higher is the shear and thus the higher is the amount of accumulated helicity at the end of the computational run.

Concerning the other processes, where the motion of the two polarities is radial outwards (emergence or fragmentation for opposite or same sign polarities respectively) or

towards each other (cancellation or coalescence for opposite or same sign polarities respectively), we note that the production of magnetic helicity is rather small. This is affected by the fact that the two polarities move for less time (almost half the computational run) inside the box and thus there is no time for large shear and significant amounts of helicity to be produced.

Additionally, we note that we can distinguish two components of velocity during the motion of the polarities: one perpendicular to and the other parallel to the line joining their centers. When the two polarities are moving relative to one another without any interaction ("fly-by" case), both velocity components are present and the perpendicular one gets its maximum value when the two magnetic features are in the centre of the box. The complete absence of this perpendicular component in the other processes, such as cancellation and emergence, leads to a much lower production of magnetic helicity. As far as the process of cancellation is concerned, we note that when the cancellation occurs with an initial tilt angle of 45° (i.e. the two polarities are on the opposite corners of the box, move towards each other and cancel at the centre), we get final accumulated magnetic helicity three times larger than for the case that the cancellation happens along the x-axis. This slight increase is connected to the fact that in the tilted case, the cancellation occurs at later time step. Hence, there is more time for the magnetic helicity to build-up.

3.4 SINGLE BIPOLE INSIDE A HEXAGONAL CELL

Having analyzed the basic flows between two polarities inside a square box, and having discussed the different ways that they can contribute to the evolution of magnetic helicity, we proceed with the insertion of a hexagonal cell inside the computational domain. This is carried out following the steps that have been described in the Section 3.2.

This is a first attempt to obtain meaningful measures of the magnetic helicity on the Quiet Sun, from the so-called magnetic carpet evolution. In the first attempt only a small portion of it, a convective supergranular cell which is governed by the numerous and continuous converging and diverging motions of magnetic fragments is considered. In this Section, we work with the emergence of one bipole and we try to explain how the various

relative motions between its two polarities can affect the magnetic helicity pattern. In the next section we study the motion of magnetic fragments, starting from two and then up to five bipolar pairs. In the multiple bipole case, we expect to observe a large number of interactions between fragments of the same or of opposite polarity, leading to results similar to the ones studied in the Section 3.3.

In order to study in detail the evolution of magnetic helicity inside a hexagonal cell due to the motion of two opposite polarities, we divide the hexagon into six equilateral triangles (as is defined by the symmetric properties of this geometrical shape). We shall keep the initial location of one polarity (the positive) fixed in one triangle (such as the fourth triangle defined by V_4OV_5 in the Figure 3.20) and we will allow the other polarity (the negative) to have continuously changing coordinates and move in each one of the triangles. Obviously, there will be a case where the two fragments end up in the same vertex and disappear (corresponding to the process of cancellation) or the case where they will end in anti diametrical vertices (driven by a "fly-by" motion along the boundaries of the cell as shown in Figure 3.20). These cases do not exactly match with the already studied processes, but for all of them we investigate how they result in magnetic helicity accumulation. We should be careful while emerging the polarities, that their initial position is confined inside the small computational box which has size $l = L/2 = 0.15$.

Different relative motions between the two magnetic concentrations inside the cell and along its boundaries will depend on the initial location of the negative polarity. We wish to study the following quantities:

- **Initial Tilt Angle** between the positive and negative polarity, defined as:

$$\tan\delta = \frac{y_{20} - y_{10}}{x_{20} - x_{10}} \tag{3.11}$$

  where (x_{20}, y_{20}) are the initial coordinates for the negative polarity and (x_{10}, y_{10}) the coordinates for the positive. For all the computational runs the latter is fixed to the location $(0.499, 0.47)$. The tilt angle between the two polarities influences the direction of their velocities and their relative motion not only inside the hexagon but also along its boundaries.

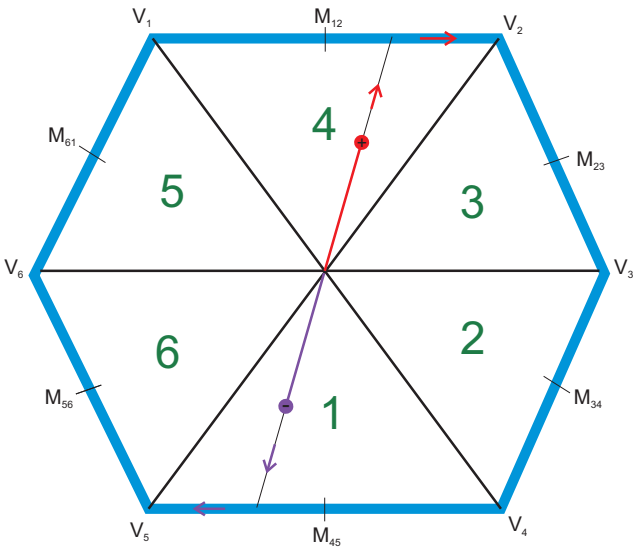

Figure 3.20: *Schematic drawing of the six equilateral triangles that compose a hexagonal cell and of the motion of each polarity, according to which triangle the magnetic concentration is initially located.*

- **Angle on hexagonal sides.** Here we estimate the angle between the velocity vectors of the two polarities when they both have reached the hexagon. Due to the geometrical properties of the hexagonal shape this angle can either be $\pm 60°$, $\pm 120°$, $0°$ or $180°$.

- **Separation distance** between the two polarities at the beginning of each computational run defined as :

$$d = \sqrt{(x_{20} - x_{10})^2 + (y_{20} - y_{10})^2} \tag{3.12}$$

- **Velocities inside the hexagonal cell and along its boundaries.** For each polarity we assume that it is initially moving radially away from the centre towards the hexagonal borders. As soon as a magnetic feature reaches a hexagonal side it moves towards the closest vertex. Thus, in accordance with the drawing of Figure 3.20, we can define for example the horizontal velocity component v_x according to the

velocity $v_{0h} = 0.5$ km/s as follows: When a polarity is moving in the hexagonal side that lays between M_{12} and V_2 or in the side between V_4 and M_{45}, then $v_x = v_{0h}$ When a polarity is moving in the hexagonal side between V_2 and M_{23} or in the side between M_{56} and V_6, then $v_x = -v_{0h} \times \cos(\pi/3.)$.

- $\mathbf{H}_i$, $\mathbf{H}_{i+}$, $\mathbf{H}_{i-}$ magnetic helicity accumulation for the total, the positive and the negative magnetic concentrations.

- $\boldsymbol{dH/dt}$, $\boldsymbol{dH/dt}_+$, $\boldsymbol{dH/dt}_-$ rate of change of magnetic helicity, for the total, the positive and the negative magnetic concentrations.

- $|\Phi|$ total absolute magnetic flux

The last parameters related to magnetic helicity are again computed using the method developed by Chae. However, we note that here the resolution of pixel size is 0.129, around 16 times smaller than the value used in real magnetograms or in Section 3.3 (where $resolution = 2''/pixel$). Consequently, we have to be careful when applying subroutines where the pixel resolution is neeeded. For instance, notice that we have to rescale the value for the parameter of full width at half maximum (FWHM) of the apodizing window function which is used in the LCT method, (November & Simon 1988)) and depends on the pixel resolution. Usually an optimal value for the extension of the area that tracks the displacement of the magnetic features between subsequent images (i.e. the so-called 'window' that is tracking a region of a magnetogram), is chosen to be bigger than the smallest feature seen in the data (see explanation on how this method is being applied by (Chae 2001)). Taking into account that for the magnetograms we used a gaussian width of the apodizing window equal to $FWHM = 10'$ that is equivalent to 5 pixels, we now use $FWHM = 5 \times resolution$.

3.4.1 "FLY-BY" ALONG THE HEXAGONAL SIDES

The first type of motion considered is the radial divergence of two polarities inside the hexagonal cell. Two polarities of opposite sign **emerge with a tilt angle of** $\sim 90^\circ$ and

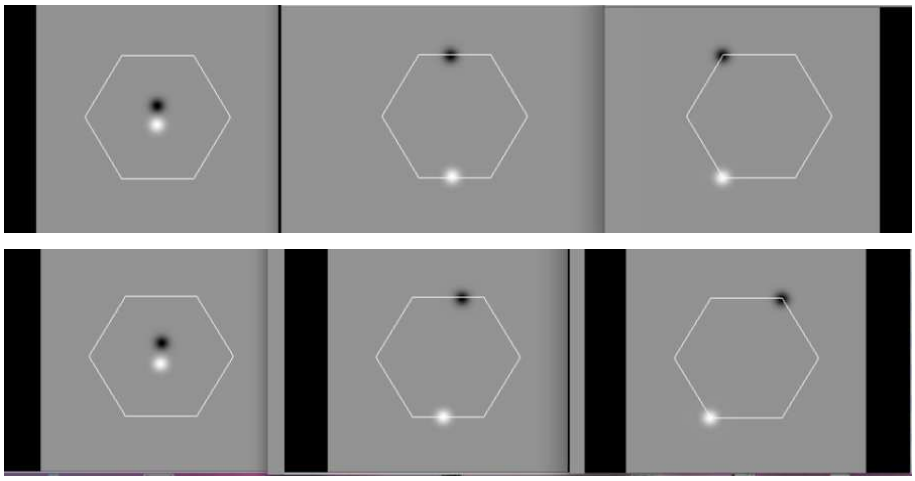

Figure 3.21: *Snapshots of the computational run that show the evolution of the magnetic field distribution when the initial tilt angle between two opposite polarities is around* 90° *and they either end on a parallel (top row) or on an antiparallel (bottom row) motion along the hexagonal cell.*

they start moving away from each other inside the hexagonal cell till they reach the side of the hexagon. This relative radial outward motion of two magnetic concentrations can result in a parallel or anti-parallel motion (with a angle of 0° or 180° respectively) along the cell boundaries, the latter being related to the "fly-by" process that we have already studied. In Figure 3.21 we see the initial position of two polarities, their position on touching the hexagon boundary of the cell and their final position. In this example the initial location for the negative polarity can either be the $(0.50, 0.55)$ leading to a parallel motion or the $(0.505, 0.56)$ resulting in an antiparallel motion between the two polarities when touching the hexagonal borders . The separation distances are 0.09 and 0.1 respectively and the tilt angles 89.3° and 86.7°.

In Figure 3.22 and Figure 3.23 we present two sets of plots that show the evolution for magnetic helicity accumulation (H_i), rate of transport of magnetic helicity (dH/dt, dH/dt_+) and total absolute magnetic flux ($|\Phi|$) for the parallel and the antiparallel case respectively. The quantities are expressed in 10^{35} Mx^2, 10^{35} Mx^2 hr^{-1} and 10^{20} Mx respectively. For both cases, we find that during the motion towards the hexagonal sides

(i.e. until $t \sim 200$ min), the accumulated amount of helicity is almost zero. This seems to be in accordance with our previous study and corresponds to the case of emergence and separation of two opposite magnetic concentrations. The situation changes when the polarities touch the hexagonal borders and move along them. We note in Figure 3.22 that the absolute value of magnetic helicity accumulation due to the positive polarity is reaching slightly higher values then the amount of magnetic helicity accumulation due to the negative polarity. This is probably due to the fact that the positive polarity reaches later the hexagonal side and hence moves in total for a longer period than the negative polarity. The rate of change of magnetic helicity is the same for the positive polarity in both the cases (as expected since it is given a fixed position and motion) and almost the same but reversed for the negative, since it changes the sign of its velocity component (from a motion towards the left vertex of the cell in one case to a motion towards the right vertex). This affects the sign of the accumulated amount of helicity.

When the flow of the two concentrations along the cell boundaries is antiparallel (resembling the fly-by process), the helicity that is accumulated by the positive concentration has the same sign as the helicity accumulated by the negative one and they both add-up and by the time they both reach the vertices they lead to the build-up of a large amount of total accumulated helicity (-100×10^{35} Mx^2, see Figure 3.23, first panel).

This is not observed in the case of parallel flow between the two polarities, since now the helicity that the positive concentration accumulates is of the opposite sign to the helicity due to the motion of the negative fragment and so they eventually almost cancel each other by the end of the computational run. At the end the total amount of injected helicity is -4×10^{35} Mx^2 (see Figure 3.22, first panel) for the parallel case, that is 25 times smaller than the value obtained for the fly-by case. The total unsigned magnetic flux remains constant throughout the whole computational period. Concluding, we find that the antiparallel motion of two opposite magnetic fragments along the hexagonal borders produces a a large accumulation of magnetic helicity that is probably connected to a rather complex topology in the magnetic configuration.

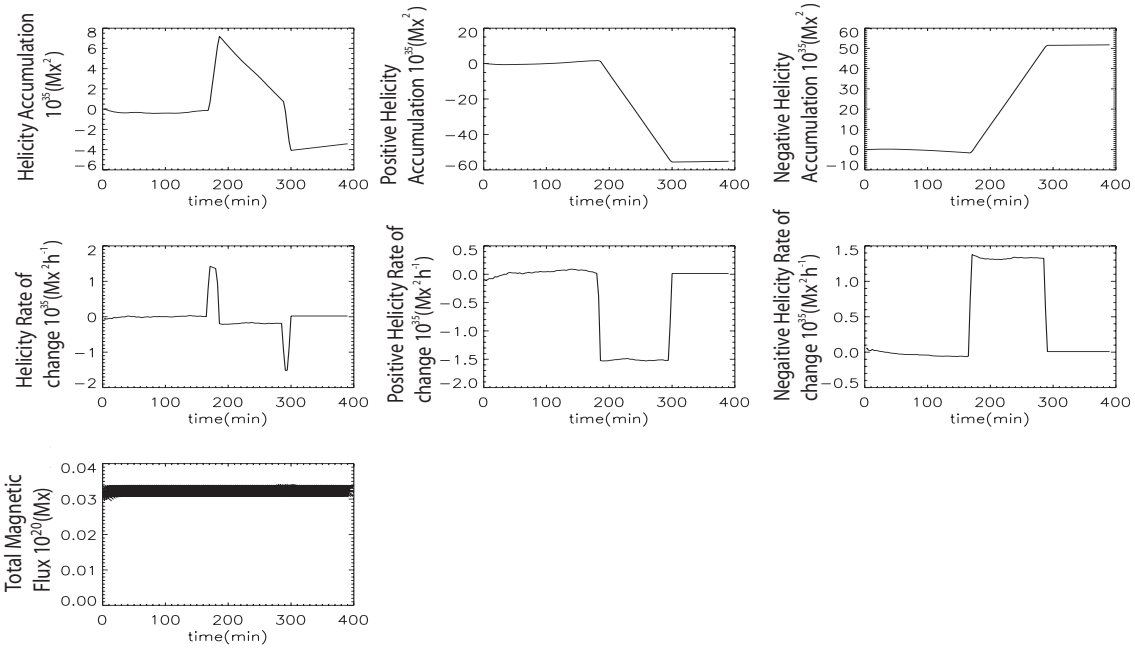

Figure 3.22: *First row: evolution of magnetic helicity accumulation for the total (first column), positive (second column) and negative (third column) polarities. Second row: rate of change of magnetic helicity for the total (first column), positive (second column) and negative (third column) polarities. Third row: total unsigned magnetic flux. The computational run corresponds to the case where the positive polarity ends on V_5 and the negative on V_1.*

3.4.2 CANCELLATION ON A HEXAGONAL VERTEX

(a) We set the initial location of the negative polarity at the point $(0.465, 0.43)$, which means that the tilt angle between the two fragments is $\delta = 50°$. Now the fragments will end up at the same vertex (V_5), where they will encounter and gradually lose their magnetic flux. Figure 3.24 shows some snapshots of this computational run. This is similar to the process of magnetic cancellation. Since both polarities are moving along the same hexagonal side and towards the same direction, their tilt angle when both have reached the side V_4V_5 is 0°.

The two concentrations are initially closely spaced, their separation distance is 0.07

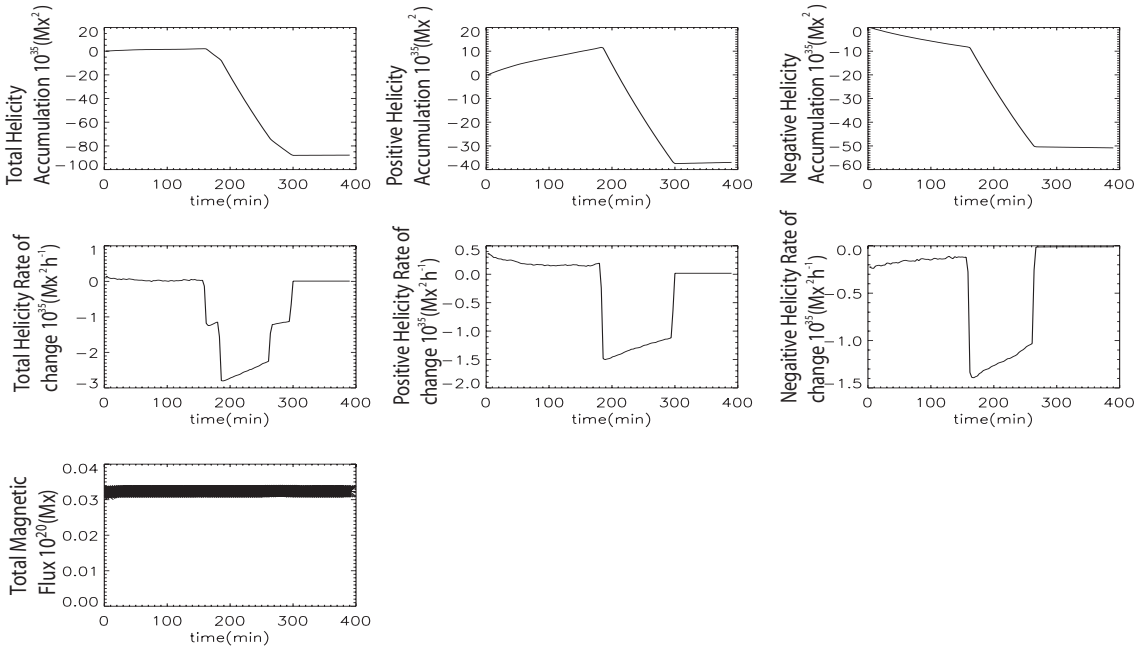

Figure 3.23: *Same parameters as in Figure 3.22. Case where the positive polarity ends on V_5 and the negative on V_1, so they move antiparallel along the hexagonal sides.*

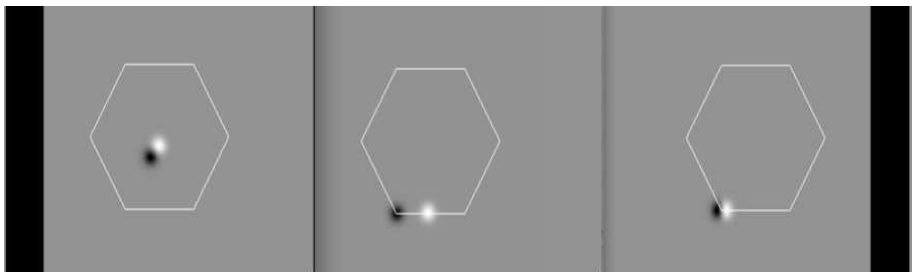

Figure 3.24: Snapshots of the computational run that show the evolution of the magnetic field distribution when two opposite polarities emerge with an initial tilt angle of $\delta = 50°$ and move along the same hexagonal side V_4V_5, directed towards the same vertex V_5 where they cancel.

and thus this short separation distance yields a high amount of accumulated helicity even from the start. This underlines the importance of a pre-existing shear between two polarities in the early stages of evolution of their total magnetic helicity. We should

notice that since the two polarities have opposite fluxes but move towards the same direction, their sign of magnetic helicity should have opposite signs. We present the graphs (Figure 3.25) of H_i, H_{i+}, H_{i-} in the first row, of dH/dt, dH/dt_+, dH/dt_- in the second row and total absolute magnetic flux ($|\Phi|$) in the last row. The positive flux, being further away from the hexagonal border than the negative, will have to travel a longer distance and so produce a larger amount of helicity flux. That is why the graph describing the total amount of accumulated helicity follows the trend and sign of the positive polarity. We also observe a sudden decrease ($\sim 50 \times 10^{35}$ Mx^2) in the amount of total accumulated helicity, during the time interval that the negative polarity has reached the hexagonal side but the positive one is still moving inside the hexagon. This also verifies the fact that the total accumulated helicity is influenced by the positive polarity that travels longer distance inside the cell.

As far as the plots that describe the rate of change of magnetic helicity are concerned, we note discontinuities (rapid change in the sign) in both the plots of the positive and negative polarity, at the time that each polarity reaches the edge of the hexagon. This is connected to the fact that the sign of magnetic helicity depends on the orientation of the relative motion of the two polarities. As soon as the polarities reach the hexagonal sides, they change direction and hence they influence the magnetic helicity sign. These discontinuities in both plots affect the total rate of change of magnetic helicity. There is a short time period where the plot that describes the total rate of change of magnetic helicity shows a sudden turnover. This sudden reversal starts when the negative concentration reaches the edge of the hexagon and ends when the positive reaches the hexagonal side too.

The mutual loss of magnetic flux in both magnetic features, is shown in the last row. Additionally, in the last row we note that initially there is an increase in the amount of the total flux, this is related to the fact that the two polarities are initially located close to each other, i.e. they have a close separation distance and so we deal with the case of partial emergence. Thus, the two magnetic fragments are initially partially overlapping. As the computation runs, the two polarities move away from each other,

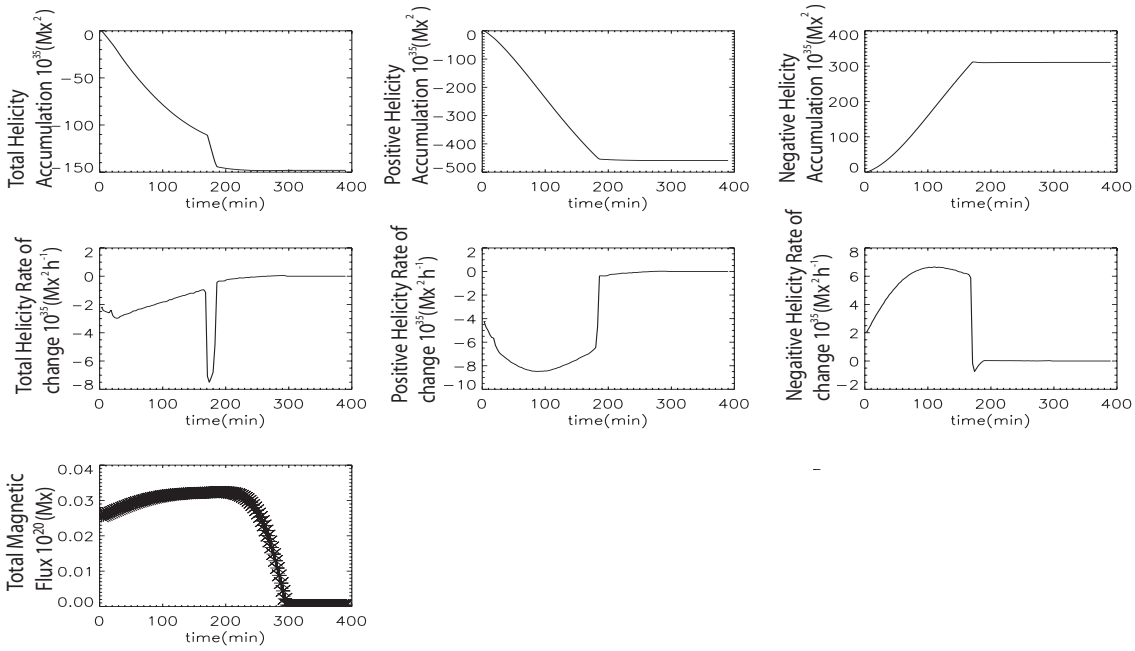

Figure 3.25: *Same parameters as in Figure 3.22. Case of* ***cancellation*** *: the velocity fields of both the positive and negative polarity have the same direction, are pushed towards the side V_4V_5 and then towards the vertex V_5 where they cancel each other.*

they become completely isolated and hence we can observe larger amount of total magnetic flux.

(b) Another case of loss of magnetic flux between the two polarities can be observed when the negative fragment is approaching the vertex V_5 from the V_6V_5 hexagonal side. In this case the angle formed by the velocity vectors of both polarities during their motion along the hexagonal sides, will be $-120°$. This motion can be achieved if for example the initial position of the negative fragment is $(0.46, 0.47)$ and so the tilt angle is $\delta = 0°$ since they both have the same y-coordinate, while their distance is rather small ~ 0.04. In Figure 3.26 we show three different time steps where the polarities a)emerge, b)reach the hexagonal sides and c) arrive to the stagnation points.

The results are shown in Figure 3.27. Both polarities get very high absolute values of magnetic helicities during their motion inside the hexagonal cell (444×10^{35} Mx^2 and

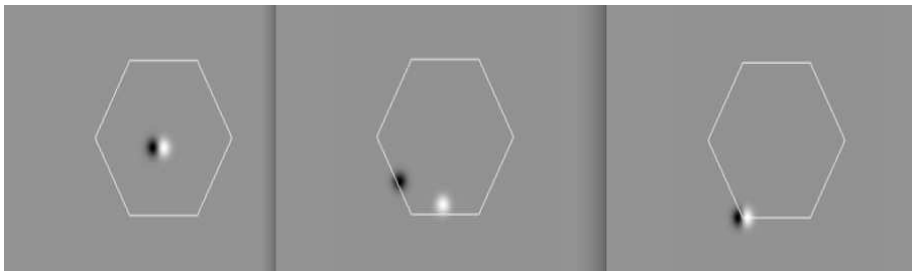

Figure 3.26: *Snapshots for the case of two opposite polarities emerging with a zero initial tilt angle. Then the negative fragment is directed towards V_6V_5, while the positive is directed towards V_5V_4. At the end they meet on V_5 where they cancel.*

312×10^{35} Mx^2 for the positive and the negative concentrations respectively) and this can be connected to the fact that the complexity of their relative motion can lead to large injection of magnetic helicity.We find that the positive polarity arrives faster at the hexagonal corner and so the motion of the negative concentration will affect the helicity flux at the later stages of the computation, as in these stages the velocity of the positive fragment is zero.

As far as the plots that describe the rate of change of magnetic helicity are concerned, we observe in all three of them sharp peaks. For each polarity these peaks start when the concentration reaches the hexagonal edge, and end when each polarity arrives at the vertex where it has zero velocity. This supports the idea that the sign of magnetic helicity depends on the orientation of the relative motion of two polarities. When the two magnetic concentrations reach the hexagonal borders and change direction, their resultant magnetic helicity changes and hence the total magnetic helicity is affected. As a result, we observe a sharp peak in the plot that describes the total rate of change of magnetic helicity that starts when the first polarity (positive) reaches the edge of the hexagon and goes on until the second (negative) polarity also reaches the hexagonal side and ends when both concentrations arrive at the hexagonal vertex where they cancel.

The initial emergence and the final cancellation processes are clearly shown in the plot

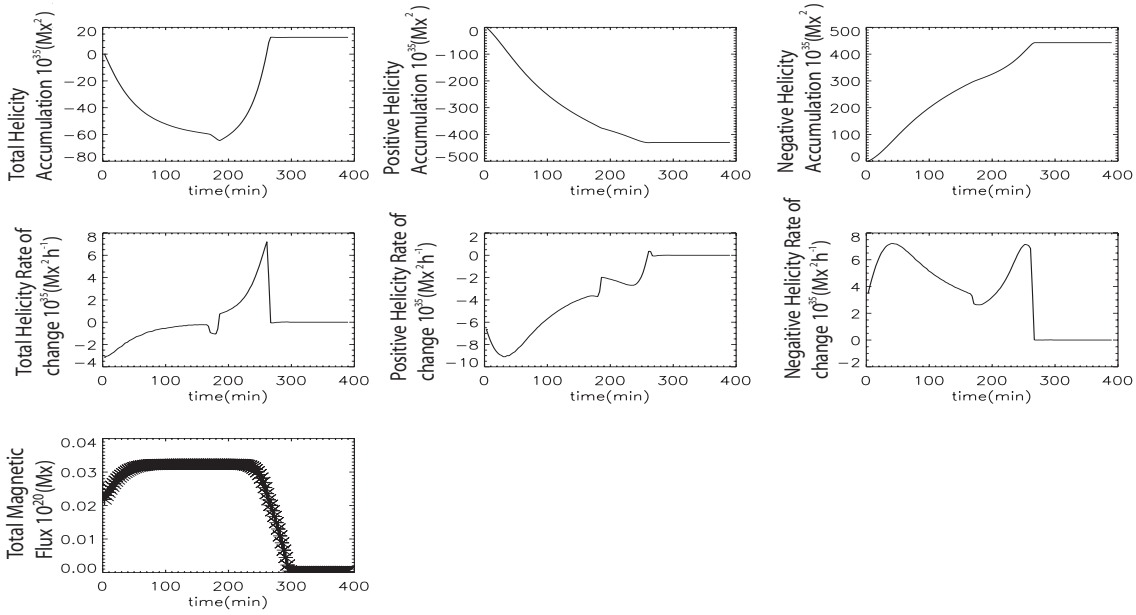

Figure 3.27: *Same parameters as in Figure 3.22. Another case of* ***cancellation****: the negative polarity moves along V_6V_5 directed towards the vertex V_5 where it cancels with the positive polarity.*

of the total unsigned flux.

3.4.3 WHEN THE NEGATIVE POLARITY ENDS AT V_4 AND A CASE OF EMERGENCE

We now distinguish two different flows that can lead to the magnetic concentration of negative flux reaching the vertex V4 of the hexagon:

(a) The initial position of the negative flux is at $(0.52, 0.46)$, so that its tilt angle with the positive concentration is $\delta = -25.5°$. As we can see in Figure 3.28 when the two polarities reach the hexagonal borders they move along the same side V_4V_5 but are directed towards opposite directions. This means that the velocity fields of the two polarities create an angle of 180° when they are moving along the same hexagonal side.

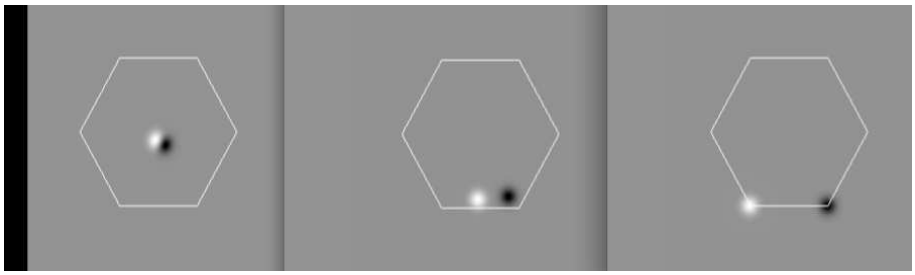

Figure 3.28: *Snapshots for the case of two opposite polarities that emerge in the triangle* V_4OV_5*, move towards the same hexagonal side* (V_4V_5) *and end up on different vertices.*

Figure 3.28 illustrates the initial close separation distance between the two polarities that is found to be 0.02. This is leading to a large build-up of magnetic helicity from the early stages of computation, as we can see from Figure 3.29. When the two polarities reach the sides of the hexagon, they move in opposite directions. At the beginning, the trend of total accumulated helicity follows the sign of the positive polarity because it covers larger distance inside the hexagon. Similarly, the plot is later affected again by the motion of the positive fragment because it is still moving inside the cell when the negative already touched its borders. The fact that the negative polarity is reaching the hexagonal vertex V_4 faster than the positive reached the vertex V_5 can be observed in the plot of the total accumulated helicity as a sudden decrease.

As far as the plots that describe the rate of change of magnetic helicity are concerned, we note discontinuities (rapid change in the sign) in both the plots of the positive and negative polarity, at the time that each polarity reaches the edge of the hexagon. This behavior was previously detected in the Figure 3.25 and it shows that the sign of magnetic helicity depends on the orientation of the relative motion of the two polarities. As soon as the polarities reach the hexagonal sides, they move towards different directions and so affect the sign of the magnetic helicity. These discontinuities in both plots affect the total rate of change of magnetic helicity. As in Figure 3.25, we notice that there is a short time period where the plot that describes the total rate of change of magnetic helicity shows a sharp reversal that starts when the negative concentration reaches first the edge of the hexagon and ends when the positive reaches

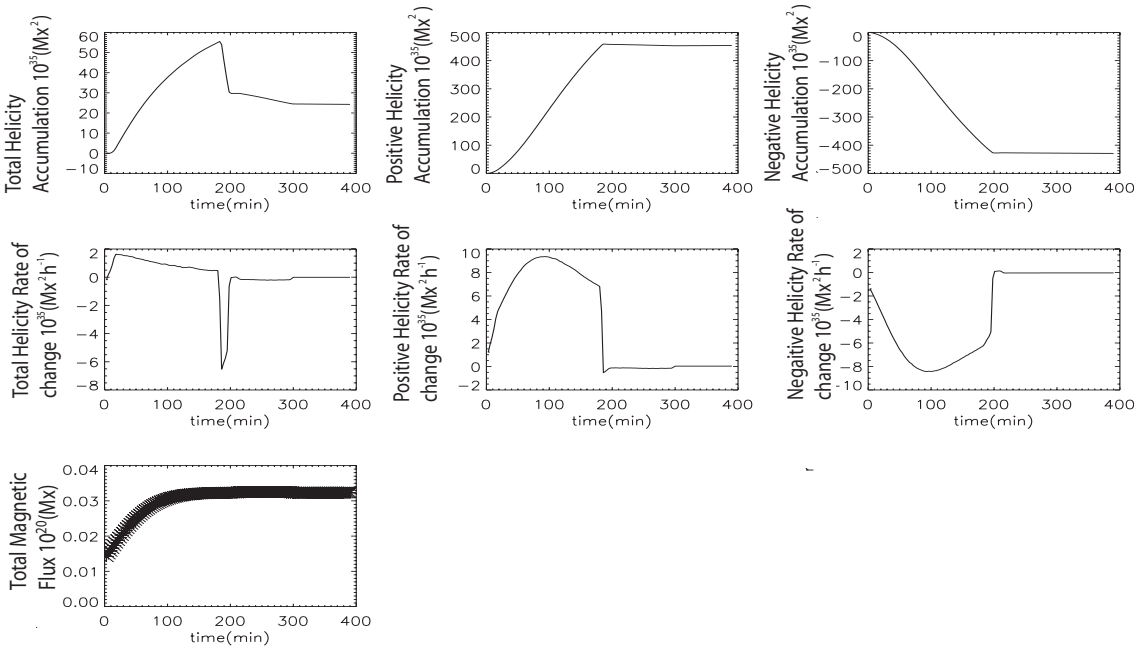

Figure 3.29: *Same parameters as in Figure 3.22. A case of initial* ***emergence****. The two opposite polarities travel towards the same hexagonal side* (V_4V_5)*, but they end up on different vertices.*

the hexagonal side too.

The observed initial increase of magnetic flux is related to the fact that the magnetic concentrations are neighboring each other and consequently they overlap and for that reason the whole process of flow inside the hexagonal cell can be considered as a case of emergence.

(b) Another route by which the negative polarity can reach the vertex V_4, is from the side lying to the right (i.e along the side V_3V_4) and so the velocity vectors of the two polarities will form an angle of $-60°$. This can be achieved if for example we locate the negative feature at (0.56,0.456) which gives an initial tilt angle of $\delta = -12.9°$ with the positive concentration. The separation distance between the two polarities is higher than in the previous case ($d = 0.06$). In Figure 3.30 we show three snapshots of the computational run for the first time step, some middle time step when the polarities

are close to the hexagonal sides, and the final configuration.

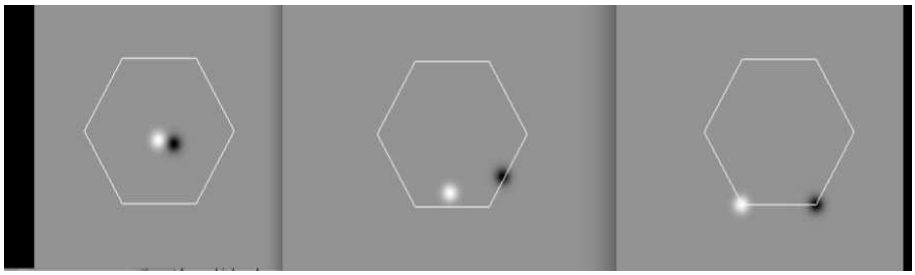

Figure 3.30: *Snapshots for the case of the positive polarity reaching the V_5 vertex and the negative one reaching the V_4 vertex.*

In Figure 3.31 we observe almost the double amount of accumulated helicity ($\sim 120 \times 10^{35}$ Mx^2) than in the previous case ($\sim 60 \times 10^{35}$ Mx^2). Nevertheless, we observe the same behavior in the plot of the total magnetic helicity : an initial increase (showing the governing influence of the positive concentration as long as it moves inside the cell), followed by a sudden decrease (showing the governing influence of the positive concentration as long as it travels along the hexagonal side while the negative has already reached the vertex).

Once again, we note discontinuities in the all the three plots that describe the rate of change of magnetic helicity. As already explained, (in the previous example or in the example shown in the Figure 3.25) such discontinuities show that the sign of magnetic helicity depends on the orientation of the relative motion of the two polarities. When a polarity changes direction, i.e. does not move any longer inside the cell but along its boundaries, the sign of its magnetic helicity is influenced and can change rapidly. The discontinuities observed in the plots for the positive and negative polarities, affect the plot that describes the total rate of change of magnetic helicity. Hence, there is a short time period where the plot that describes the total rate of change of magnetic helicity, shows a sharp turnover that starts when the negative concentration reaches first the edge of the hexagon and ends when the positive reaches the hexagonal side and ends at the vertex V_5.

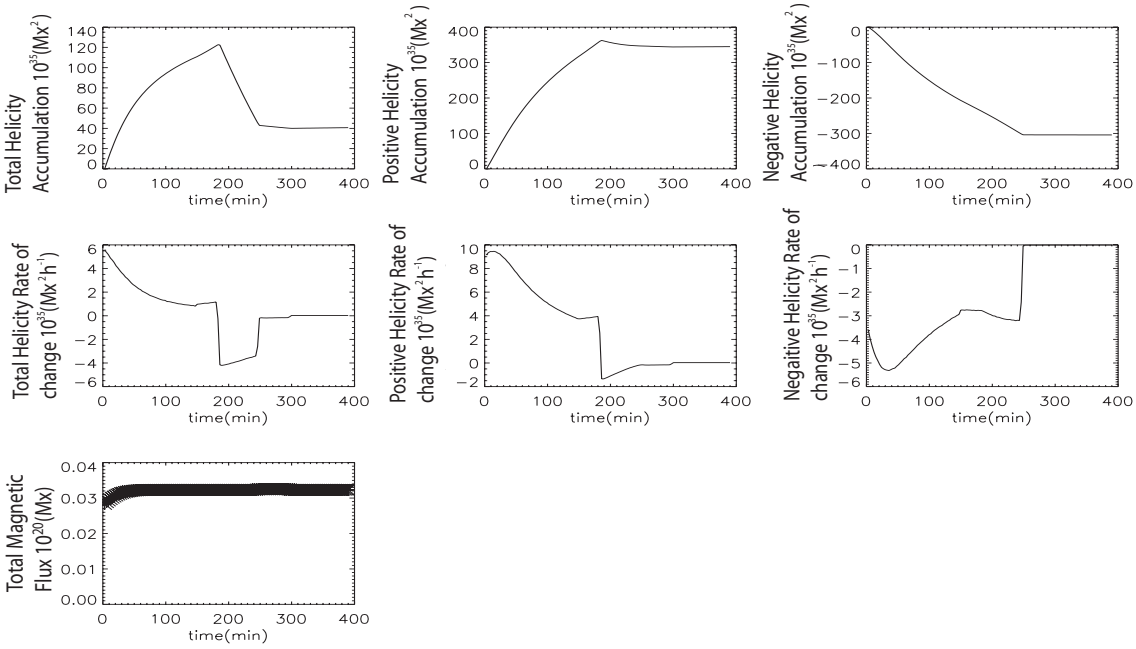

Figure 3.31: *Same parameters as in Figure 3.22. A case where the positive polarity ends on V_5 and the negative on V_4, the latter moving along V_3V_4.*

The plot that describes the total absolute magnetic flux remains constant since we do not deal with any process of cancellation. A very slight increase is observed at the beginning of the computation, related to the fact that initially the magnetic fluxes of the two polarities overlap each other by a very small amount.

3.4.4 WHEN THE NEGATIVE POLARITY ENDS AT THE V_3

The negative feature can end up in the V_3 vertex of the hexagonal cell, either by moving clockwise (i.e along the V_4V_3 side) or by moving anti-clockwise (i.e along the side V_2V_3).

(a) We locate the negative concentration at the position (0.565, 0.465) and let it move radially inside the cell, then it reaches the side V_4V_3 and from there it moves towards the V_3 vertex. In that case the tilt angle between the two polarities is $-4.7°$, their initial separation distance is 0.06 and their angle when both are moving along the hexagonal borders is 120°. The snapshots in Figure 3.32 describe the relative motion

of the two fragments for this computational example.

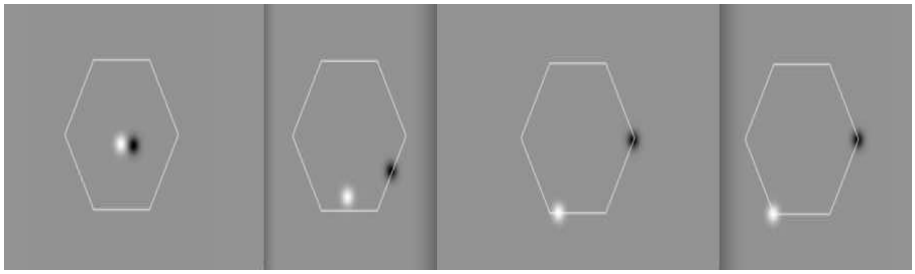

Figure 3.32: *The negative polarity moves along the side V_4V_3 and ends at the vertex V_3. We can see on the third image that the negative polarity has reached the vertex V_3 while the positive is still moving along the hexagonal side.*

The upper left panel of Figure 3.33 shows that the magnetic helicity accumulation is positive, following the trend of the positive polarity while it moves inside the cell. As we can see in Figure 3.32 there is a period when the positive concentration still moves inside the cell while the negative polarity is already flowing along the hexagonal border. For this reason the helicity of the positive polarity gets higher absolute values and keeps on contributing primarily to the trend of the total helicity flux. During this time (t = 150 min to t = 280 min), the U_y component of the velocity of the negative polarity changes sign (from downward direction inside the cell to upward direction when the polarity moves along the hexagonal cell) and its helicity flux shows an inversion in its trend which can be observed in the total build-up of magnetic helicity.

The plots that describe the rate of change of magnetic helicity show discontinuities as in the previously mentioned examples. This behavior, observed in all of the three plots, is connected to the fact that each polarity changes direction when it reaches and move along a hexagonal side.

The total magnetic flux remains almost constant as shown in the lower panel of Figure 3.33, since there is no interaction of magnetic flux between the two concentrations. However, there is a very small initial increase in the amount of the total absolute

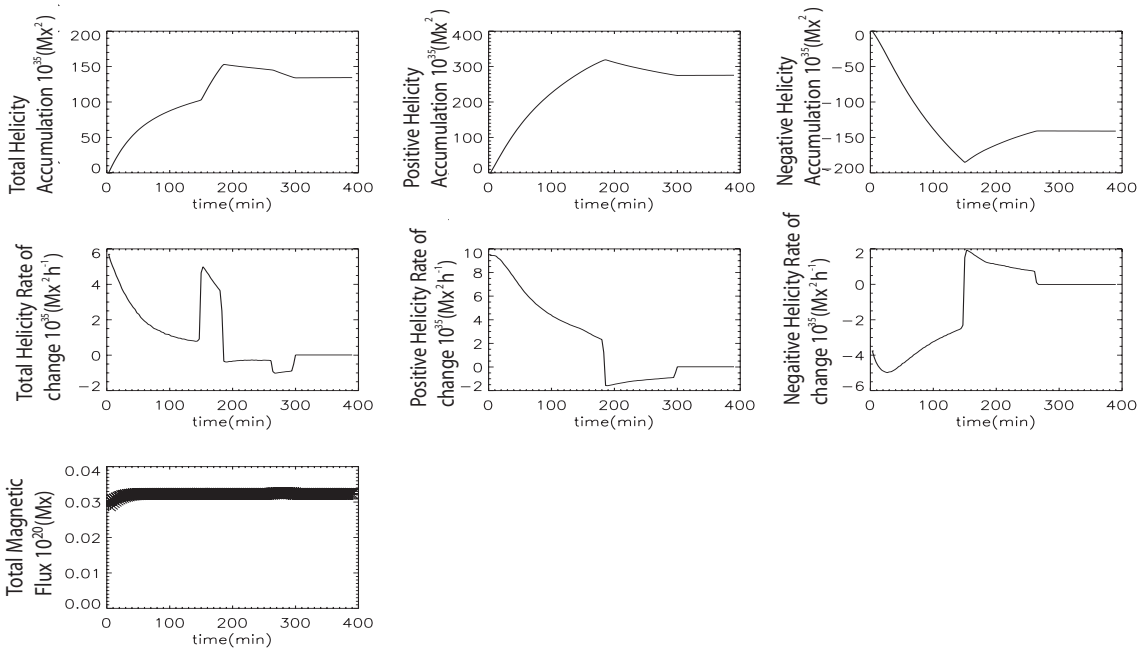

Figure 3.33: *Same parameters as in Figure 3.22. A case where the initial position of the negative polarity leads to a radial motion towards the V_4V_3 side and then to the vertex V_3. The positive polarity reaches the vertex V_5 as in previous examples.*

magnetic flux because at the beginning of the computation, the two polarities are overlapping each other by a small amount. As soon as the two polarities move away from each other and become completely isolated, there is no interaction between them and the total absolute magnetic flux becomes constant.

(b) We consider (0.56, 0.53) as initial location for the negative polarity, so that it reaches the vertex V_3 by moving along the V_2V_3 side. In this case, the tilt angle between the two magnetic fragments is 44.5°, their initial separation $d = 0.08$ and the angle between their flow fields while moving on the hexagonal borders is $-120°$. In Figure 3.34 we show some representative time steps of the computational run: when they emerge, when they approach the hexagonal sides and when they reach the vertices.

We observe an initial increase in the plot that describes the total amount of accumulated helicity (see Figure 3.35) and this reveals the governing influence of the positive

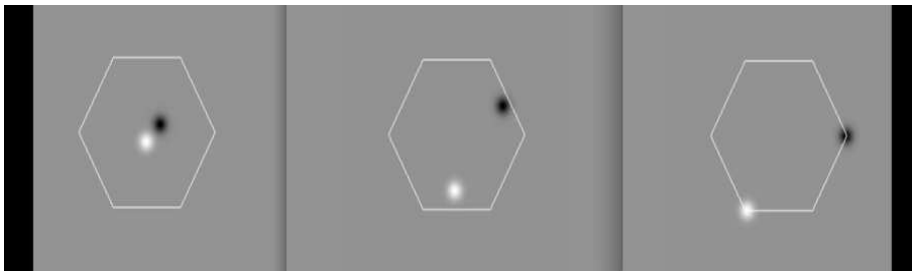

Figure 3.34: *Snapshots for the case where the initial location of the negative magnetic feature leads it towards the V_2V_3 hexagonal side and then towards the V_3 vertex.*

concentration (that is still moving inside the cell even though the negative has reached the border V_2V_3). This increase is followed by a sudden decrease that can be correlated with the trend of accumulated helicity observed for both the positive and the negative polarities. This occurs because when the two concentrations reach the hexagonal borders, they change direction of motion and lead to a change in the magnetic helicity sign.

Discontinuities are observed in each of the three plots (total, positive and negative) that describe the rate of change of magnetic helicity. Such an evolution has already been explained in the previous examples.

The total unsigned magnetic flux remains stable. Thus, no processes of emergence or cancellation between the two magnetic concentrations occur.

3.4.5 WHEN THE NEGATIVE POLARITY ENDS AT THE V_2

In this computation the negative polarity can reach the vertex V_2 by two different sides of the hexagon, depending on its initial coordinates. In section 3.4.1 we have already analyzed the case where the two polarities move relative to each other ("fly-by") and the negative concentration ends at the V_2 vertex from the left-hand side. The other possible way to reach V_2 is by a flow along the side V_3V_2, thus creating an angle of 61° with the velocity field of the positive flux that moves along the side V_4V_5. Let us for example locate the negative fragment at the position (0.54,0.545), so that the separation distance with

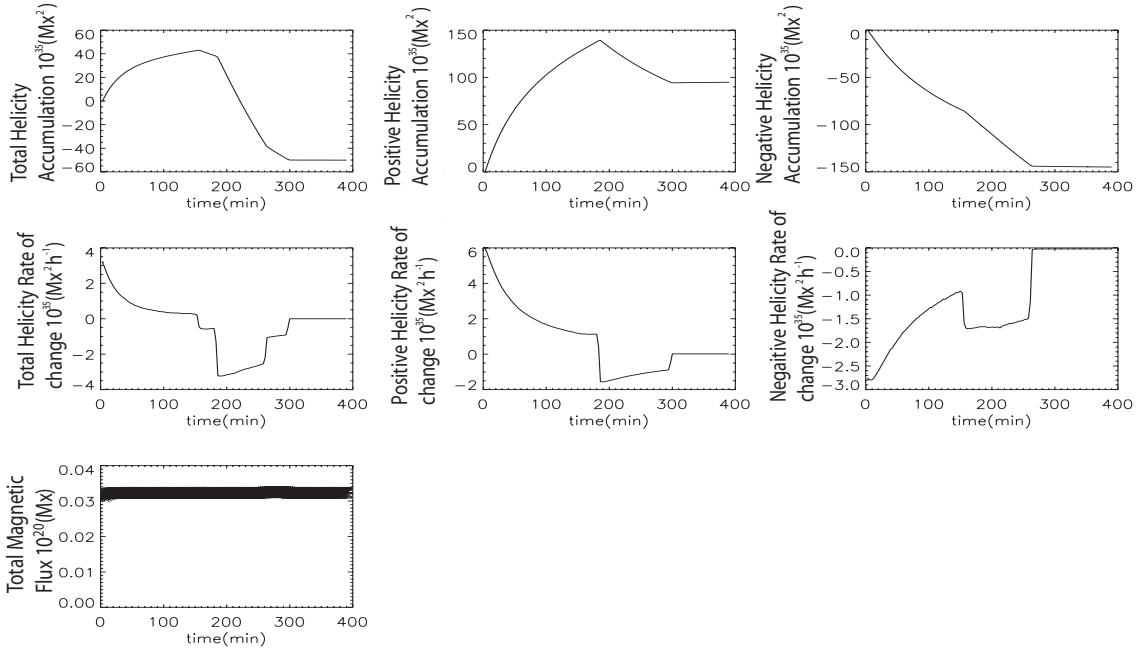

Figure 3.35: *Same parameters as in Figure 3.22. A case where the negative polarity is moving radially towards the V_2V_3 hexagonal side and ends up on V_3. The positive polarity ends at V_5.*

the positive polarity is $d = 0.08$ and their initial tilt angle is 61°. Four snapshots of this computational run are shown in Figure 3.36, where we can see that the negative polarity reaches the vertex V_2 while the positive polarity is still moving along the hexagonal side .

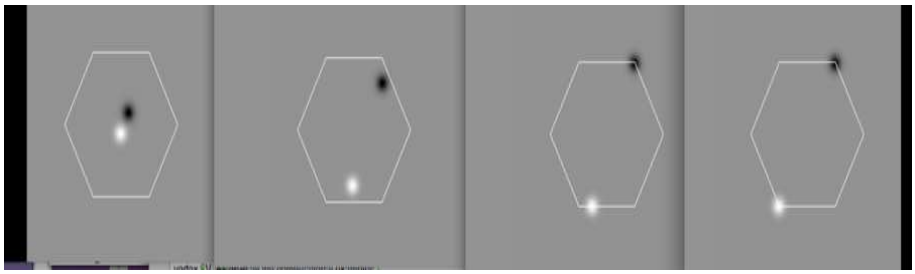

Figure 3.36: *Snapshots for the case where the initial tilt angle between the positive and the negative polarity is* 61° *so that the negative moves towards the side V_3V_2 and eventually reaches the vertex V_2.*

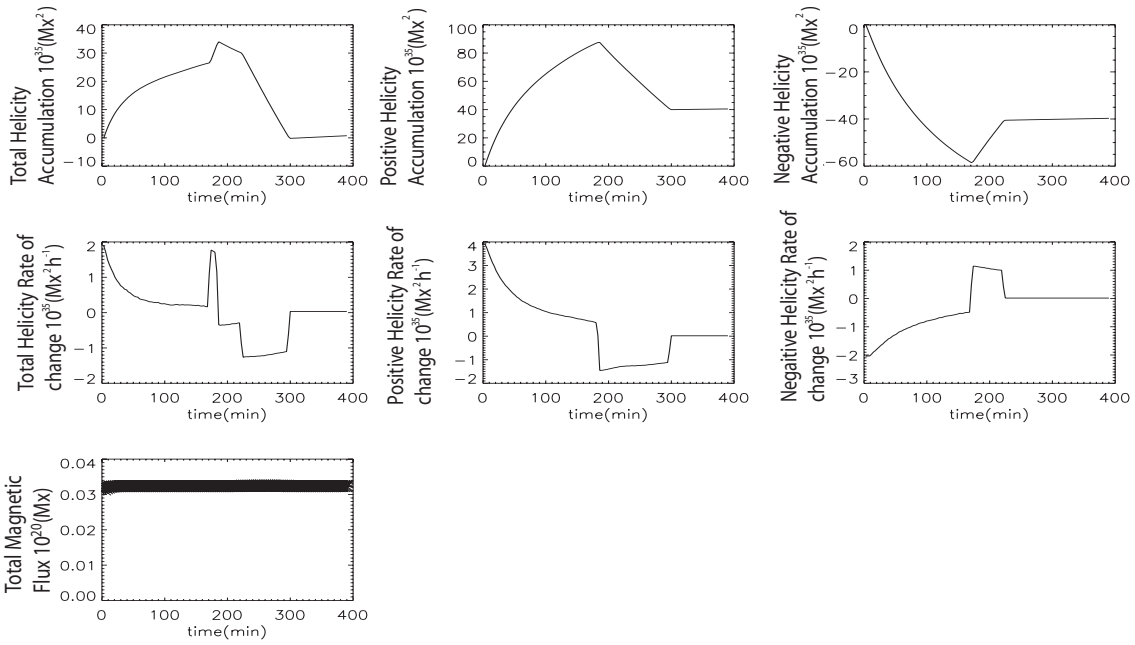

Figure 3.37: *Same parameters as in Figure 3.22. In this case the initial position of the negative polarity leads it towards the side V_3V_2 from where it reaches the vertex V_2. The positive polarity reaches the vertex V_5.*

The results are shown in Figure 3.37. We note that the graphs for the helicity flux resemble to the graphs obtained for the case 3.4.4(a). In both cases the trend of total, positive and negative magnetic helicity accumulation are very similar. Here again, we note that all of the three plots that describe the total accumulated magnetic helicity, are changing at the moment that each polarity is reaching a hexagonal side. Discontinuities are observed in the plots that describe the rate of change of magnetic helicity and they are also connected to the fact that the magnetic concentrations are changing direction of motion and so they influence the sign of the produced magnetic helicity.

However, it is important to mention that there are two basic differences:

(i) In the case described in 3.4.4(a) we obtained much larger values for the peak and the final amount of the total, positive and negative accumulated helicity (H_{iMax} $\sim 153 \times 10^{35}$ Mx^2, $H_{i+Max} \sim 320 \times 10^{35}$ Mx^2, $H_{i-Min} \sim -185 \times 10^{35}$ Mx^2) than

in this case, where the value for total helicity accumulated by the end of the run is found to be 0.75×10^{35} Mx^2.

(ii) The decrease that the positive and total magnetic helicity show when both polarities move along the hexagonal borders, is larger than in the case discussed in 3.4.4(a). In this new case the two concentrations touch almost simultaneously the hexagonal borders in contrast with the case 3.4.4(a), where the negative feature reaches the corner V_3 while the positive is still moving inside the cell. Thus, the positive polarity was affecting the trend of the total accumulated magnetic helicity. Moreover, we note that in this current example the positive polarity accumulates much less helicity (H_{i+}) during its motion along the hexagonal sides than in the case described in 3.4.4(a) and it shows an important decrease which affects the plot of the total accumulation of helicity(H_i). A reason that could explain why in this case the polarities accumulate lower helicity, is that in this computational run the two opposite magnetic polarities are moving along hexagonal sides that are far from each other (i.e. the positive polarity is moving along the side V_4V_5, whereas the negative one is moving along the side V_3V_2), in contrast to the case described in 3.4.4(a). This is related to the fact that a shorter distance between two magnetic features (as in the case 3.4.4(a)) results in a higher generation of magnetic helicity. The higher the separation distance between two polarities, during their motion along the hexagonal sides, the lower is the resultant accumulated magnetic helicity.

3.4.6 WHEN THE NEGATIVE POLARITY ENDS AT V_1

Here we consider the case that the negative concentration is initially located at (0.46,0.53) and is moving along V_6V_1 and eventually reaches the point V_1 earlier than the positive reaches the vertex V_5, as shown in the Figure 3.38. Here the initial tilt angle between the two polarities is -60° (i.e the opposite than in the previous case 3.4.5), their separation distance is $d = 0.07$ whereas their velocity vectors along the hexagonal sides form an angle 120°. The other possible motion along the V_2V_1 side has already been presented in section

3.4.1.

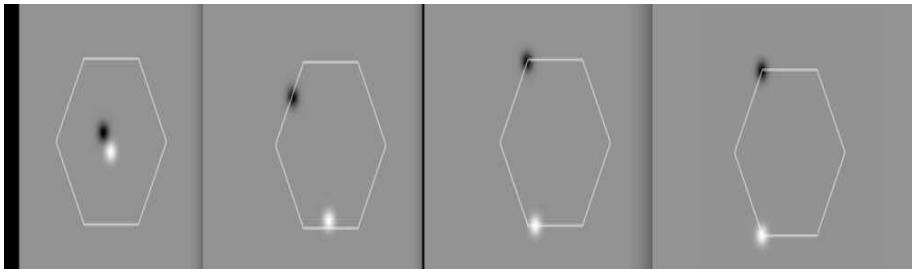

Figure 3.38: *Snapshots for the case where the initial tilt angle between the positive and the negative polarity is* -60° *so that the negative moves towards the side* V_6V_1 *and eventually reaches the vertex* V_1*, some time steps earlier than the positive one reaches the* V_5*.*

The results for magnetic helicity and total magnetic flux can be seen in the Figure 3.39. Once more the trend of total magnetic helicity seems to be following the plot obtained for the positive polarity, decreasing throughout the whole computational run. It is possible that this result is connected to the fact that the negative polarity is faster to arrive both on the hexagonal side V_6V_1 and on the vertex V_1 than the positive. Until both the concentrations reach the hexagonal lanes, the total accumulated helicity is not very large ($\sim 60 \times 10^{35}$ Mx^2). Once again, we note that the plots that provide the total accumulated magnetic helicity (total, positive and negative) change behavior at the moment that each polarity is arriving at an edge. Since the positive polarity is traveling for a longer period inside and along the border of the hexagonal cell, its magnetic helicity can reach higher values for longer period (compared to the magnetic helicity produced by the negative polarity) and hence it affects primarily the total accumulated magnetic helicity (compared to the contribution to the total magnetic helicity by the negative concentration that arrives faster at the hexagonal edge and vertex V_1).

When a magnetic feature changes direction, i.e. from a radial motion inside the cell to a motion along the borders, the sign of magnetic helicity is affected. This can be observed in each of the three plots that describe the rate of change of magnetic helicity as a discontinuity, that starts when a polarity is reaching the hexagonal side and ends when the polarity reaches a vertex and hence has zero velocity.

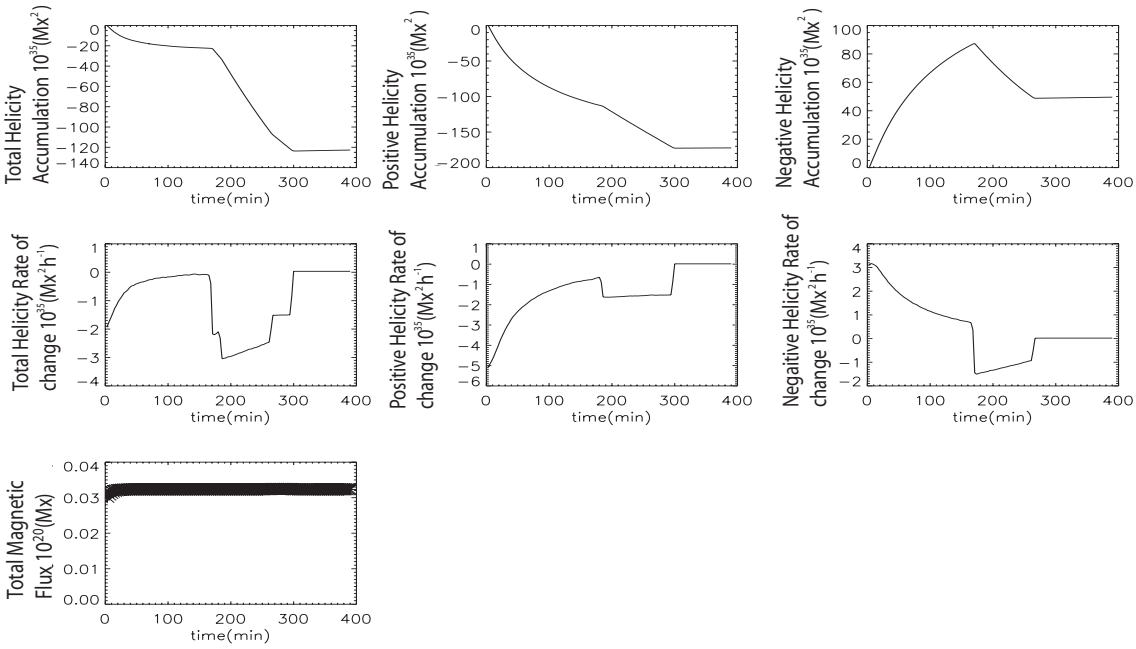

Figure 3.39: *Same parameters as in Figure 3.22. In this case the negative polarity is initially located at (0.46,0.53) and so directed towards the side V_6V_1 from where it goes to the vertex V_1.*

There is a slight increase at the start in the plot that describes the total unsigned magnetic flux. This is connected to the fact that initially the two polarities are close to each other and their fluxes are overlapping by a small amount. Hence, a partial emergence is taking place at the beginning of the computation.

3.4.7 WHEN THE NEGATIVE POLARITY ENDS AT V_6

We now change the location of the negative concentration so that it ends up on the V_6 vertex of the hexagonal cell. Again there are two different ways by which this can be achieved :

(a) The negative polarity moves along the V_1V_6 side creating an angle $-60°$ with the positive that moves along the side V_4V_5. This can happen if for example the negative feature starts from the point (0.44, 0.52) and so is at an initial tilt angle of $-40.3°$

with the positive polarity, and their distance is $d = 0.08$. We can see some snapshots of this computational run in Figure 3.40.

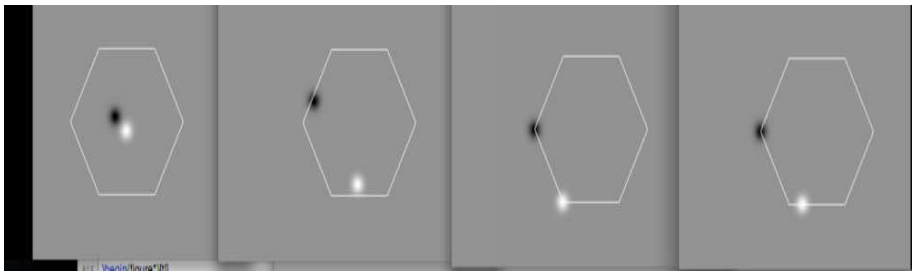

Figure 3.40: *Snapshots for the case where the negative polarity reaches the vertex* V_6 *being initially located at (0.44, 0.52) and moving later along the hexagonal side* V_1V_6.

The results of our computation are shown in Figure 3.41. We find that the total accumulated helicity (H_i) is rather small ($\sim -30 \times 10^{35}$ Mx^2) until the moment that both the polarities reach the border of the hexagonal cell. Moreover, initially the total magnetic helicity is influenced by the trend of the higher accumulated helicity due to the positive concentration inside the cell (i.e is influenced by H_{i+}). However, we notice a change in the evolution of the total magnetic helicity when the negative fragment hits the hexagonal lane ($t_2 = 243$ min) and a more important change when also the positive feature starts its motion along the borders ($t_1 = 300$ min). The evolution of the two plots for the positive and negative fluxes are opposite and so we expect them to cancel each other and to give a rather small value for the final accumulated helicity (-76×10^{35} Mx^2). Since the positive feature is moving for a longer time along the hexagonal side (see also Figure 3.40), it can get higher values for longer periods and affects primarily the final value of the total magnetic helicity.

The plots that describe the rate of change of magnetic helicity due to the positive and the negative polarities, show a sudden reversal that lasts for the time period that a concentration reaches the hexagonal edge until it ends at a vertex, where it obtains zero velocity. This affects the plot that describe the total rate of change of magnetic helicity, where we also observe a turnover that starts when the first concentration (the negative) reaches the hexagonal side V_1V_6 and ends when the second concentration

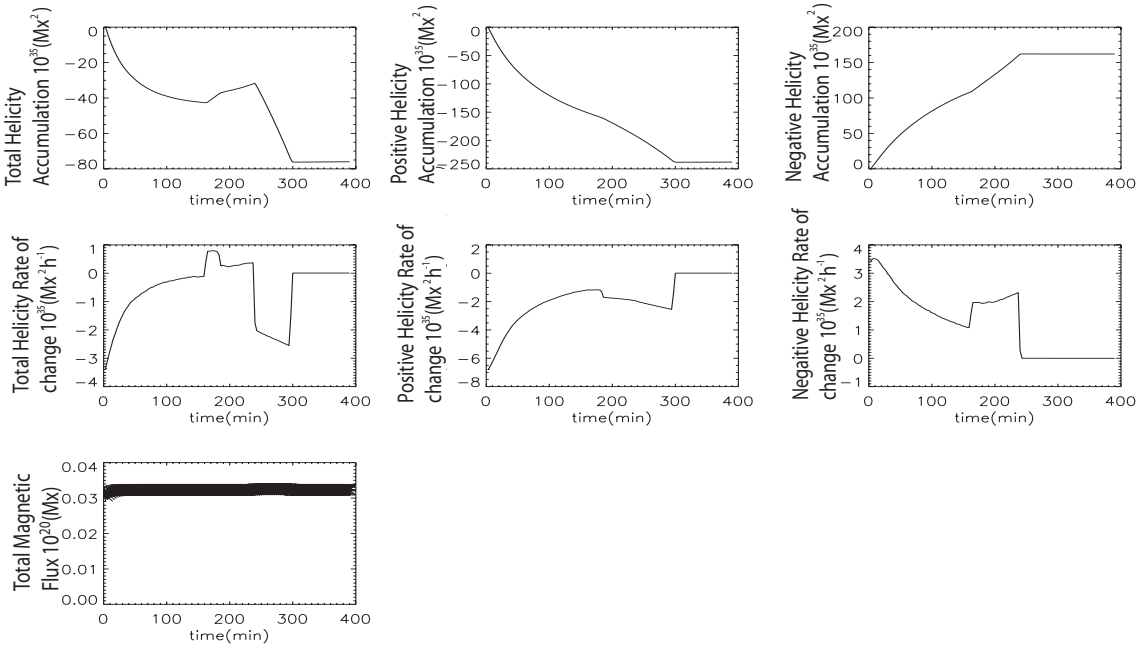

Figure 3.41: *Same parameters as in Figure 3.22. In this case the negative polarity is directed towards the side V_1V_6 from where it goes to the vertex V_6.*

(the positive) arrives at the vertex V_5.

There is initially partial emergence of the two polarities, in the sense that their magnetic fluxes are overlapping and hence a slight initial increase is observed in the plot that describes the absolute total magnetic flux.

(b) The initial location given for the negative polarity is (0.44, 0.47) and so its tilt angle with the positive polarity is 0° and their separation distance is $d = 0.06$. The negative polarity reaches the V_5V_6 side, and moves towards the V_6 vertex creating an angle of 60° with the velocity vector of the positive magnetic concentration. The computational run is shown in the Figure 3.42 where we observe that in this case too, the negative polarity reaches sooner both the hexagonal side and the hexagonal vertex than the positive one.

We note in Figure 3.42 that the plots that describe the accumulated magnetic helicity for the positive and the negative magnetic concentrations show very high values: for

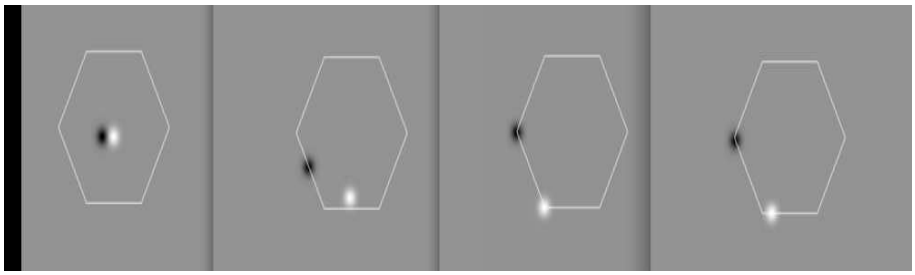

Figure 3.42: *Snapshots for the case where the negative fragment arrives to the vertex* V_6 *moving along the hexagonal side* V_5V_6 *and forming initially a* $0°$ *tilt angle with the positive.*

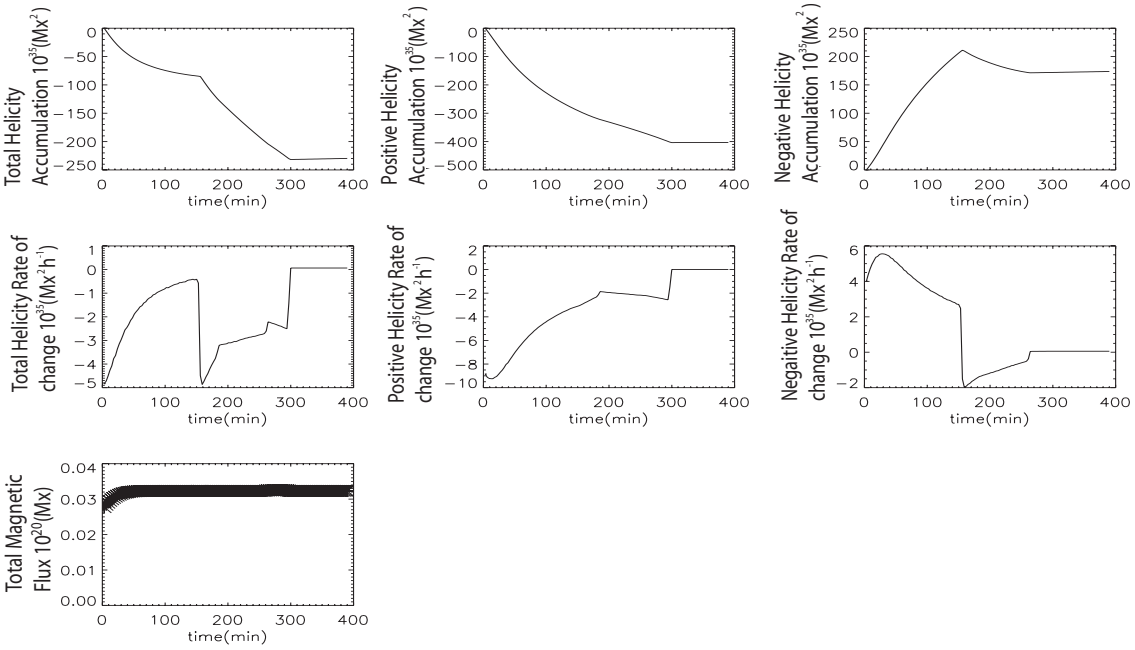

Figure 3.43: *Same parameters as in Figure 3.22. In this case the initial position the negative polarity is (0.44, 0.47) and so is directed towards the side* V_5V_6 *and ends on the vertex* V_6*.*

the positive polarity the maximum absolute value is 403×10^{35} Mx^2 and for the negative one it is 211×10^{35} Mx^2. This can be connected to the fact that the distance between the two polarities is the shortest, since they are moving in adjacent hexagonal borders in contrast to other cases where for instance the positive polarity travels along V_5V_4 and the negative in a further hexagonal side (as the previously analyzed case

(a)). Similar was the case described in 3.4.4(a) where the relative motion of the two polarities was along neighboring hexagonal borders. There we also observed high amount of magnetic helicity accumulation for the positive and the negative polarities. The amount of accumulated helicity due to the positive concentration is a bit higher than the other one due to the negative, because the first (the positive) is moving along the V_4V_5 for a longer period and thus generates higher magnetic helicity. As a result, we can conclude that when the relative motion between two polarities is along neighboring hexagonal sides, they are contributing to a high accumulation of magnetic helicity.

Moreover, we see again that the magnetic helicity depends on the orientation of the relative motion of the two magnetic polarities : discontinuities are observed in all the plots that describe the rate of change of magnetic helicity for the period that a polarity changes the direction of its motion and from a radial motion inside the cell it ends up on moving along a hexagonal side.

Once again there is a partial emergence of magnetic flux, in the sense that the two polarities are initially located at close positions and hence their magnetic fluxes are overlapping. That is the reason why we observe a slight increase in the unsigned total magnetic flux at the beginning of the computational run.

3.5 DISCUSSION OF THE SIMPLE BIPOLE CASE

We have demonstrated that the flow of a bipole inside a hexagonal cell can provide different trends and values of magnetic helicity accumulation, depending on the initial position, the time and the location at which the polarities reach the hexagonal cell borders (i.e. when and where a polarity will reach the hexagonal edge related to the time and location when the opposite polarity will reach another border). These are mainly a function of the initial tilt angle which defines the velocity fields for each feature. We note that as long as one polarity keeps on **moving inside the cell**, it attains higher absolute values of magnetic helicity than the other polarity that is arriving earlier at the hexagonal borders, and

consequently the total injection of helicity will be a result of the first magnetic element. This is obvious in the computational run shown in Section 3.4.4(a). There the positive fragment hits the hexagonal side later than the opposite flux and it yields high values of helicity flux (320×10^{35} Mx^2 at a time $t_1 = 186$ min. In contrast, the negative concentration reaches the V_2V_3 side on a time $t_2 = 150$ min and gets lower absolute value for magnetic helicity (185×10^{35} Mx^2). As a result, the values for the total accumulated helicity reached up to 153×10^{35} Mx^2. In the cases where the two polarities reach almost simultaneously the sides of the hexagon we do not get so high values for the total accumulated helicity, as seen in the examples 3.3.5 and 3.3.6. At the moment when both polarities touch the hexagonal borders we get a total absolute value for helicity $\sim 60\times10^{35}$ Mx^2. Thus, **we understand that significant injection of magnetic helicity can indeed be provoked when one polarity moves inside the hexagonal cell and hence gets higher values of magnetic helicity and the other is moving along the hexagonal sides** .

It is important to notice that the trend of the accumulated magnetic helicity is changing as soon as a polarity reaches a hexagonal edge. This can be observed for all the described cases for the plot of the total accumulated magnetic helicity: the plot has an initial evolution during the motion of both polarities inside the hexagon and this evolution changes when the polarities reach the hexagonal borders. **The relative movement of magnetic sources, i.e. whether they move inside or along the hexagonal borders, is the key element in the build up of magnetic helicity**.

This can also be justified from the plots that describe the rate of change of magnetic helicity. For each polarity, these plots show sudden turnovers that last from the moment that the polarity reaches a hexagonal side and end as soon as the polarity reaches a vertex, where has zero velocity. Both the plots of the rate of change of magnetic helicity due to the positive and negative polarities show these discontinuities and hence result in an observed turnover in the graph that describes the total rate of change of magnetic helicity.

Additionally, when the initial tilt angle between the two magnetic features is $\sim 90^\circ$ we note that there is no accumulation of magnetic helicity since there is no shear between the two polarities.

Moreover, we would like to comment that there are two cases (3.4.7(b) and 3.4.4(a) where the two magnetic concentrations are moving along neighboring hexagonal lanes. In these cases, we observe that the absolute maximum and final amount of accumulated magnetic helicity (for the total, the positive and the negative polarities contribution) reaches very high values. It is mainly the accumulated helicity due to the polarity that travels for longer period inside and along the hexagonal cell boundaries (which in our examples was the positive concentration) that is producing very high magnetic helicity and thus affects the total accumulated magnetic helicity. This can be explained by the fact that in these cases the two polarities are close to each other and hence, as we have already seen in Section 3.3.3, the shorter the distance between the two polarities during their motion, the higher the shear and hence the higher the amount of total accumulated magnetic helicity. As a result, we conclude that the highest production of magnetic helicity occurs in the "junctions" between neighboring borders of the supergranular cell. This may indicate an enhanced occurrence likelihood of eruptive events in the corona above these 'junction' points.

3.6 RANDOM GENERATION OF BIPOLES INSIDE A HEXAGONAL CELL

In this section we focus on the random generation of multiple opposite polarity magnetic concentrations at the centre of the hexagonal cell, their relative flows along its boundaries and the subsequent magnetic flux interactions that can occur between them. Multiple processes will take place. Some of them are sufficiently complex to produce magnetic helicity.

We initially work with two bipoles and then we gradually insert more bipolar flux regions reaching a maximum number of five. The insertion of bipolar pairs is carried out :

1. **Simultaneously.** In an attempt to make the computation as simple as possible, we assume that the emergence of all the bipoles is happening simultaneously in the first snapshot. However, we should keep in mind that real observational data of

supergranular flows, such as images obtained from MDI on board SOHO or SOT on board HINODE, reveal a continuous emergence of bipoles at the centre of each cell as well as motions and interactions of different kinds between the new emerging and the pre-existing flux sources at any point of the cell with highest probability along the boundaries (see in Dere et al. (1991) or Aiouaz (2008)). Thus, in a future work we should insert the bipolar pairs at different time steps, so as to obtain a more realistic computation of the supergranular flows that can be compared with observations.

2. **Randomly** In contrast with the analysis performed in the previous sections where the initial coordinates of the magnetic concentrations were well-known, we now consider random spatial insertion of the bipolar flux features. The random locations (x_1, y_1) and (x_2, y_2) for the positive and the negative polarities of each bipolar pair, at the beginning of the computational run can be defined as:

IDL> $x_1 = rand(i * 4 + 0) * Lb + x_{h0} - L_{b/2}$
IDL> $y_1 = rand(i * 4 + 1) * Lb + y_{h0} - L_{b/2}$
IDL> $x_2 = rand(i * 4 + 2) * Lb + x_{h0} - L_{b/2}$
IDL> $y_2 = rand(i * 4 + 3) * Lb + y_{h0} - L_{b/2}$

where the index i describes the number of bipoles (i.e $i = 0$ for 1 bipole, $i = 1$ for 2 bipoles , $i = nbi - 1$ for a nbi number of bipoles), (x_{h0}, y_{h0}) is the centre of the emergence box (and so the centre of the hexagonal cell according to the model set up as presented in Section 3.2). It has lenght L_b, and " **rand**" generates 4 random numbers for nbi bipoles with the help of the function :

IDL> $rand = randomu(seed, 4 * nbi)$

This indicates that when the " **seed**" number changes, the initial location of the magnetic polarities changes and so their relative motion changes leading to different results. Without loss of generality, we choose to work initially with the same "seed"

number for all the cases examined, so as to ensure consistency in the graphs obtained for different numbers of emerging bipoles. For the most complex case, that of the evolution of five bipoles, we will run different computations that correspond to different seed numbers (i.e $seed = 12$, $seed = 10$, $seed = 14$) in order to cover a large variety of possible flows and interactions that can occur between many polarities of mixed sign and to be able to distinguish one that lead to a similar evolution from other that produce a different build-up of magnetic helicity.

The rest of the computation is carried out following the steps described in Section 3.2 and the procedures described for the single bipole evolution in Section 3.3. Once again we are dealing with circular magnetic features that are characterized by magnetic fields with Gaussian profiles and peak strength of 100 G. However, since the exact position of each flux concentration is unknown, we cannot estimate either the initial tilt angle nor the separation distance between the polarities of the bipoles. Consequently, we restrict our analysis to calculating just the amount of accumulated magnetic helicity, the rate of helicity transport and the evolution of the total unsigned magnetic flux due to the supergranular motions and the interactions of mixed polarity concentrations.

3.7 DISCUSSIONS ON THE MOTION OF MULTIPLE BIPOLES INSIDE A HEXAGONAL CELL

In Figure 3.44, 3.45 we present some snapshots for each computational run (i.e. emergence of two, three, four and five bipoles) where we can see we can see that different processes can occur depending on the orientation of the bipoles. These processes lead to different number of bipoles at the end of each computational run. The resultant accumulated helicity is connected to both parameters : relative motion of magnetic concentrations and hence shearing, and number of magnetic features by the end of the computation. The total accumulated magnetic helicity for each computational run, is shown in the last panel of Figure 3.44.

The results obtained for the accumulated helicity (H_{ifinal}) for different number of

emerging bipoles indicate that the final amount of accumulated helicity is not representative of the number of bipoles that are inserted inside the hexagonal cell. However, it can indicate the number of polarities that exist when the computational run ends. More specifically, this was observed for the case that we emerged two and four bipolar pairs and at the end of the computational run, there remained just two polarities. The "loss" of magnetic concentrations was due to events such as cancellation or coalescence. The final amount of total accumulated helicity was rather small, i.e for the case of an initial emergence of 8 polarities, we ended with an accumulated helicity 106×10^{35} Mx^2. On the contrary, when we emerged five bipoles with $seed = 12$, at the end of the computational run, there were five polarities placed at the vertices. Consequently, the final amount of accumulated helicity in this case was higher, i.e. 258×10^{35} Mx^2.

The initial trend of accumulated helicity for all the cases of different number of emerging bipoles, depends on the initial relative motion of the polarities that have the smallest separation distance. This is in accordance with the results studied in the previous Sections 3.3 and 3.4, where we observed that the shortest the distance between two polarities, the higher is the shear and hence the largest is the magnetic helicity. As a result, when inside the hexagon there is a large polarity that is initially composed by 2 or more concentrations closely separated, its motion is going to affect more than any other polarity the initial build up of magnetic helicity. When this polarity is splitted in 2 or more completely isolated smaller magnetic fragments, its influence on the magnetic helicity accumulation is not as dominant as at the beginning.

There is a wide variety of trends of accumulated helicity that we can obtain depending on the random motions of the polarities inside the hexagon. In other words, there is not a unique trend in the behavior of magnetic helicity. Different interactions between mixed sign polarities, such as cancellation, advection, coalescence and fragmentation, lead to different results. The resultant accumulated helicity obtained from each process depends on the orientation that describes the relative motion of the interacting polarities.

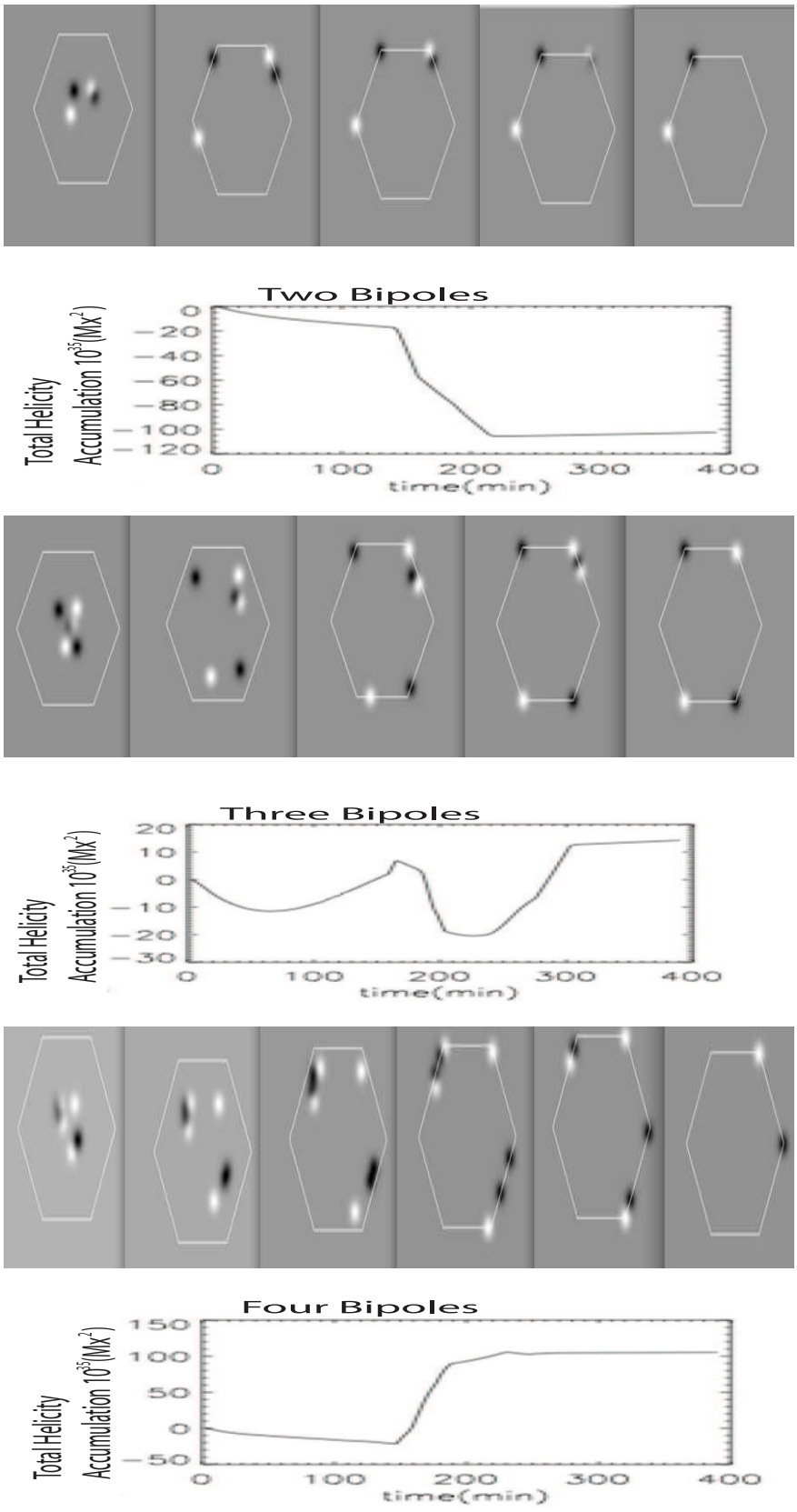

Figure 3.44: *From top to bottom : the first, third and fifth panels show the random generation of 2, 3 and 4 bipoles inside the hexagonal cell when choosing seed* $= 12$*, the second, fourth and sixth panels show the total accumulated magnetic helicity for each case.*

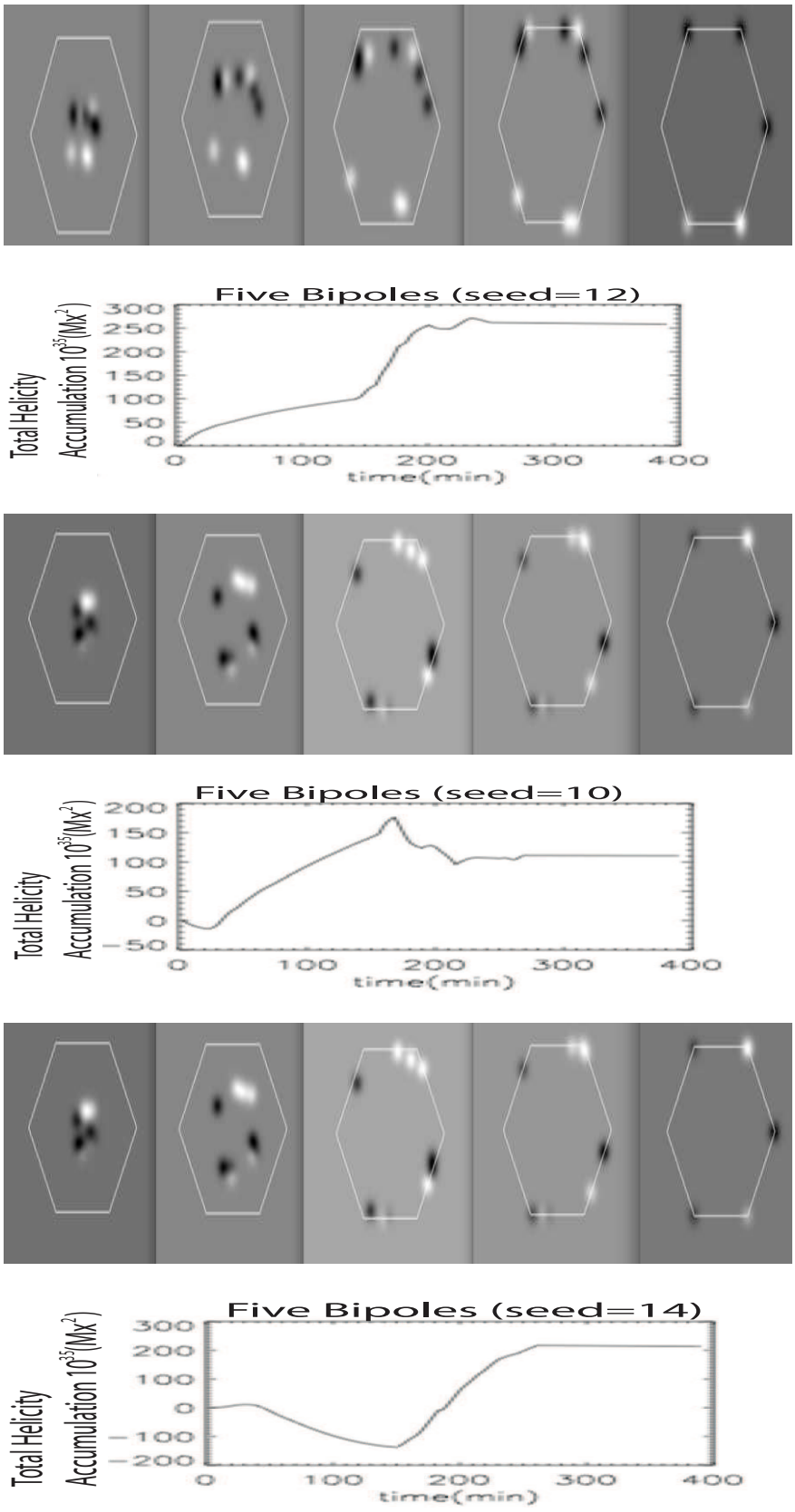

Figure 3.45: *the first, third and fifth panels show the random generation of 5 bipoles inside the hexagonal cell when choosing seed = 12, seed = 10 and seed = 14 respectively. The second, fourth and sixth panels show the total accumulated magnetic helicity for each case.*

Chapter 4

Conclusions and Future Work

"Ithaca has given you the beautiful voyage.
Without her you would have never set out on the road.
She has nothing more to give you.
And if you find her poor, Ithaca has not deceived you.
Wise as you have become, with so much experience,
you must already have understood what Ithacas mean."
Konstantinos P. Kavafis, **"Ithaca"** (1911)

4.1 Conclusions

In this thesis we have investigated the trend of magnetic helicity injection on the Sun both observationally and theoretically.

Firstly, as described in the second chapter, we have performed an observational analysis of EIT/SOHO and MDI/SOHO images for a sample of active regions during the period February 2000 - June 2003. The purpose of this research was initially to be able to recognize the regions that are the most probable (halo) CME initiation sites. This was achieved by computing the difference between EUV images, using always as pivot image the one that was closest to the time occurrence of the CME. These difference images were carried out for every active region of our sample on time intervals of 6 hrs (working with data acquired at

171 Å, 284 Å and 304 Å for a period of a day) or 12 min (as in the case of images acquired by EIT at 195 Å for a period of a few hours). The active region that in the difference images showed significant variations in intensity and size (of brightest and darkest area) at the time of the halo CME, indicated the occurrence of a dynamic event. In contrast, the other active regions observed on the solar disk during the same period, showed an almost constant profile in intensity when analyzed both for short periods (few hours before or after the event) and for longer periods (like a day before and after the eruption). Moreover, a comparison between the eruptive event registered in the NOAA report and this brightness variation provided us a further indication about the active region that was the site of the initiation of the halo CME.

With this choice, we limited our analysis to 10 active regions and then we investigated the behavior of magnetic helicity accumulation in these sites, in order to determine whether and how changes in magnetic helicity accumulation can be temporally correlated with CME occurrence. More specifically, we distinguished two classes of CMEs (gradual and impulsive) and we examined the temporal variation of magnetic helicity and magnetic flux over a period of 2 days for each of the selected ARs. For this reason we have used a code developed by Chae (2001) and Pariat (2004). Our results demonstrated that as far as the classification between gradual and impulsive CMEs is concerned, the total unsigned magnetic flux remains almost constant for gradual CMEs, while it decreases or increases significantly for ARs related to impulsive events. Moreover, for the impulsive group of CMEs, the magnetic helicity shows more significant variations than for the gradual ones. Eighty percent of the ARs generating gradual CMEs follow the hemispheric helicity rule, while 60% of the impulsive CMEs seems to be related with an exception to this rule. Additionally, the plotted magnetic helicity flux shows a sudden change in its trend before the CME in 1/3 of the examined active regions. These regions interestingly are connected to the occurrence of X-class flares and after the CME in 1/3 of the active regions.

This can be considered as an interesting finding since the first case underlines the major role of phenomena such as new flux emergence or shearing/twisting of the magnetic field lines from subphotospheric layers through turbulent convective motions, in destabilizing

the coronal magnetic configuration, leading to a significant production of magnetic helicity and providing the triggering mechanisms for eruptive events.

The second case is connected to changes in magnetic helicity that happen after the CME, and hence may be connected to a lack of torque balance between the subphotospheric part of a flux rope and the coronal field that has just lost some stress via the CME launch.

Secondly, as described in the third chapter, we have performed a number of computations that provided us the information on the evolution of magnetic helicity due to different motions of magnetic features (i.e. bipoles) initially inside a square box and later inside a convective hexagonal cell. Once again, we made use of the code that was developed by Chae (2001) in order to calculate the magnetic helicity trend. Processes of advection, cancellation, emergence, coalescence and fragmentation were computed and their influence on the production of magnetic helicity studied. The final amount of accumulated helicity at the end of each computational run is higher for the case of advection ('fly-by') and more specifically when the separation distance between the two polarities is small. This demonstrates that the stronger the shearing motion the larger the helicity injection. The direction of magnetic helicity (i.e. its sign) depends on the orientation of the motion of magnetic features. Additionally, we note that we can distinguish two components of velocity during the motion of two polarities: one perpendicular to and one parallel to the line that is joining their centers. When the two polarities are moving relative to one another without any interaction ("fly-by" case), both of the components of velocity are present and the perpendicular one gets its maximum value when the two magnetic features are at the centre of the box (one lies above the other). The complete absence of this perpendicular component in the other computed process, such as cancellation and emergence, leads to a much lower production of magnetic helicity.

Moreover, we have simulated the emergence of a bipole inside a hexagonal cell and its motion from the centre of the cell towards its sides and its vertices, where the magnetic elements are located at downflows. Multiple bipoles were also considered and hence the above mentioned processes were examined once more (Smyrli et al. (2011)).

Our results highlighted the importance of shearing motions between magnetic frag-

ments in the build up of magnetic helicity. When the tilt angle between two polarities is $\sim 90^{\circ}$ there is no production of magnetic helicity. In contrast, a close emergence of some magnetic concentrations or a 'fly-by' process along the hexagonal sides can be important factors in the generation and build up of magnetic helicity. More importantly, large amounts of accumulated helicity were obtained at the junctions of neighboring supergranular lanes. This can be connected to the fact that above these points there are commonly observed eruptive phenomena, such as micro-flares and/or mini-CMEs that recently have been proposed as possible mechanisms for coronal heating (Innes et al. (2008); Innes et al. (2009) and Innes et al. (2010)).

4.2 Future Work

In future we plan to extend our computational work to more than one supergranular cell, so that we may describe the whole magnetic carpet configuration. Initially, this will be carried out in 2-D computations and later in 3-D, where we will be able to include a range of heights in the solar atmosphere where different energy release processes are occurring. These processes may lead to a possible conversion of magnetic energy into heat and bulk plasma motion (as proposed for example by Sakurai (1989); Parker (1996) and Chen & Shibata (2000).) To do so, the low level of the horizontal domain will be presented by a larger number of supergranular cells with many bipoles. In this way we are attempting to:

(i) once again study the emergence and continuous motion of footpoints (i.e magnetic bipoles) of field lines inside and along the supergranular cells that compose the magnetic carpet configuration.

(ii) study the field lines connecting these footpoints at higher levels and the processes that can possibly occur from their interaction and relative shearing such as

- the formation of current sheets at the interface between new and pre-existing flux systems. We note that the emergence of each bipolar pair is going to happen at different times so that field lines of the bipoles that have already emerged can interact with new emerging polarities,

- magnetic field line reconnection and
- loss of equilibrium in such a level that can provoke the energy release and maybe a possible heating mechanism for the low corona.

Ideally we can represent the above events with the help of a code that not only can solve the magnetohydrodynamic equations but also takes into account the effects of compressibility, radiative transfer and partial ionization in the equation of state that are necessary ingredients of the problem of magnetic flux emergence (as is shown by (Cheung et al. 2007))

Such a tool can provide information on which flows provoke loss of equilibrium in higher levels of the solar atmosphere. Our ultimate scientific goal is to construct a powerful and physically meaningful computational code that can represent the variety of levels through which magnetic helicity is produced from the convection zone, to the transport through the intermediate layers of the atmosphere and finally accumulated in the corona. With this the release of magnetic energy may provide an answer to the small scale heating of the corona as suggested by Potts et al. (2007) and later Innes et al. (2009) or to the occurrence of dynamic eruptive events. In that way the problem of the identification of initiation sites of CMEs in the solar corona can be achievable and even then the prediction of such dynamic phenomena can be also considered by investigating the buildup of magnetic helicity from the small scale magnetic carpet to the large scale corona.

Of course such a research needs to be supported by high quality observational data. It is therefore important to work with the highest image resolution so as to be able to recognize the smallest flows which nevertheless can change the magnetic structures in a slow but continuous way.

A first approach into this topic can be achieved by working with data from the Helioseismic and Magnetic Imager (HMI) onboard SDO that can provide images similar to MDI but with higher resolution. In this way the problem of the identification of initiation sites of CMEs in the solar corona may be achievable and then even the prediction of such dynamic phenomena can be a visible possibility.

...

Acknowledgements

It is a honor for me to thank those who have made this thesis possible, through their support in every possible way. They are numerous, and may I be forgiven in case I forget someone.

Most importantly, I want to thank my family. My parents Nikos and Sasa for teaching me the most important lessons since I was a child, the most important values in life (that I try to follow even though sometimes it is hard) and for being so supportive, full of respect and encouragement for my efforts. My brother Vasilis who is very relaxed and full of passion for life, characteristics that inspire me, help me to calm down and "take it easy" in moments of "panicking". Vasilis, my grandfather for everything.

II would specifically and deeply from my heart would like to thank my supervisor Prof Francesca Zuccarello who was continuously next to me. Her support, dedication to her work, continuous presence were inspiring me to keep on. Her help, positive attitude and every day supervision contributed importantly to this thesis

Also, I would like to thank my supervisor Dr. Duncan Mackay whose supervision and his useful comments on my work and thesis, always motivated me to work as hard as possible in order to improve and fully understand the theoretical part of my work.

Moreover, I am grateful to my co-supervisor Dr Daniele Spadaro for his interest in my work and support.

This work would not have been possible without the financial support of the **SOLAIRE Network**. Many thanks to the coordinator of this program Fernando Moreno Insertis. Thanks to him and the SOLAIRE Network, I had the opportunity to participate in a large number of conferences, schools and workshops, where I met numerous interesting

scientists and I gained important experience for my PhD.

From the Observatory of Catania, I would like to thank Dr Paolo Romano for taking time and interest in explaining to me my questions. I more than appreciate all his advice during my studies that proved to be useful. The director of the Observatory of Catania, Prof. Gianni Strazzulla, for making me feel more than welcome and comfortable in the work environment.

Also, I would like to extend my thanks to Francesco Zuccarello who, every time that was visiting Catania, spent many hours with me, having chats about our common topics. I have really enjoyed our collaboration.

From the University of St Andrews, I am grateful to Prof. Eric Priest for being so helpful with me, in the moments I really needed a help, for making me feel welcome in the department and in the solar group and for showing a lot of interest on my work. I would like also to thank Dr Scott for his very interesting lectures on fluid dynamics.

I am grateful to my supervisor during my undergraduate studies in the University of Athens, Prof. Panagiotis Niarchos for introducing me into the field of astrophysics, helping me during the whole period I was writing my thesis and supporting me to continue my studies

My thanks to the very helpful segn.ra Rapicavoli.

David for his love and mainly for who he is, a very special person.

Last but not least my friends!!! :

* from Greece : Nikos, Olga, Manos for just holding me up when needed.
* from St Andrews : Nabeelah for being such a good friend always, John the best housemate I could ever have (since he was washing my dishes always), Simon for teaching me the celtic harp and philosophy in dark winter evenings.
* all my SOLAIRE co-phd students!
* from Catania : my JiuJitsu (“DaiKi Dojo”) team, and my maestro Giovanni who taught the importance of discipline, continuous effort, respect and not to be afraid. My co-corridor friends : Zuzana, Francesco, Stavro for taking care of me every day.

My friends of “CUS”, for having nice healthy running breaks where I could take all the stress out.

* my best friends B. and T.

Bibliography

Aiouaz, T. 2008, ApJ, 674, 1144

Antiochos, S. K., DeVore, C. R., & Klimchuk, J. A. 1999, ApJ, 510, 485

Archontis, V. & Török, T. 2008, A&A, 492, L35

Attrill, G., Nakwacki, M. S., Harra, L. K., et al. 2006, Sol. Phys., 238, 117

Berger, M. A. 1999, Plasma Physics and Controlled Fusion, 41, 167

Berger, M. A. & Field, G. B. 1984, Journal of Fluid Mechanics, 147, 133

Bothmer, V. & Daglis, I. A. 2007, Space Weather – Physics and Effects, ed. Bothmer, V. & Daglis, I. A. (Praxis Publishing)

Brandenburg, A. 2001, ApJ, 550, 824

Brandenburg, A. 2005, ApJ, 625, 539

Brandenburg, A. 2009, Plasma Physics and Controlled Fusion, 51, 124043

Canfield, R. C., Hudson, H. S., & McKenzie, D. E. 1999, Geophys. Res. Letters, 26, 627

Chae, J. 2001, ApJ, 560, L95

Chae, J. 2003, ApJ, 584, 1084

Chae, J. & Jeong, H. 2005, Journal of Korean Astronomical Society, 38, 295

Chae, J., Moon, Y., & Park, Y. 2004, Sol. Phys., 223, 39

BIBLIOGRAPHY

Chae, J., Moon, Y., Rust, D. M., Wang, H., & Goode, P. R. 2003, Journal of Korean Astronomical Society, 36, 33

Chandra, R., Pariat, E., Schmieder, B., Mandrini, C. H., & Uddin, W. 2010, Sol. Phys., 261, 127

Chen, A. Q., Chen, P. F., & Fang, C. 2006, A&A, 456, 1153

Chen, J. 1989, ApJ, 338, 453

Chen, J. & Krall, J. 2003, Journal of Geophysical Research (Space Physics), 108, 1410

Chen, P. F. & Shibata, K. 2000, ApJ, 545, 524

Cheung, M. C. M., Schüssler, M., & Moreno-Insertis, F. 2007, A&A, 467, 703

Chou, D., Labonte, B. J., Braun, D. C., & Duvall, Jr., T. L. 1991, ApJ, 372, 314

Christensen-Dalsgaard, J., Gough, D. O., & Thompson, M. J. 1991, ApJ, 378, 413

Clark, Jr., A. & Johnson, H. K. 1967, Sol. Phys., 2, 433

Cook, G. R., Mackay, D. H., & Nandy, D. 2009, ApJ, 704, 1021

Cremades, H. & Bothmer, V. 2004, A&A, 422, 307

Dasso, S., Mandrini, C. H., Démoulin, P., & Luoni, M. L. 2006, A&A, 455, 349

De Rosa, M. L. & Toomre, J. 2004, ApJ, 616, 1242

Delaboudinière, J., Artzner, G. E., Brunaud, J., et al. 1995, Sol. Phys., 162, 291

Démoulin, P. 2007, Advances in Space Research, 39, 1674

Démoulin, P. 2008, Annales Geophysicae, 26, 3113

Démoulin, P. & Berger, M. A. 2003, Sol. Phys., 215, 203

Démoulin, P., Mandrini, C. H., van Driel-Gesztelyi, L., et al. 2002, A&A, 382, 650

Démoulin, P. & Pariat, E. 2009, Advances in Space Research, 43, 1013

den, O. G. 2008, Astronomy Reports, 52, 931

Dere, K. P., Bartoe, J., Brueckner, G. E., Ewing, J., & Lund, P. 1991, J. Geophys. Res., 96, 9399

Dmitriev, A. V., Crosby, N. B., & Chao, J. 2005, Space Weather, 3, 3001

Duvall, Jr., T. L. & Birch, A. C. 2010, ApJ, 725, L47

Elsasser, W. M. 1956, Rev. Mod. Phys., 28, 135

Forbes, T. G., Linker, J. A., Chen, J., et al. 2006, Space Sci. Rev., 123, 251

Forbes, T. G. & Priest, E. R. 1995, ApJ, 446, 377

Giovanelli, R. G. 1980, Sol. Phys., 67, 211

Gopalswamy, N. 2003, Advances in Space Research, 31, 869

Gopalswamy, N., Lara, A., Yashiro, S., Nunes, S., & Howard, R. A. 2003a, in ESA Special Publication, Vol. 535, Solar Variability as an Input to the Earth's Environment, ed. A. Wilson, 403–414

Gopalswamy, N., Shimojo, M., Lu, W., et al. 2003b, ApJ, 586, 562

Gopalswamy, N., Yashiro, S., & Akiyama, S. 2007, Journal of Geophysical Research (Space Physics), 112, 6112

Gosling, J. T., Hildner, E., MacQueen, R. M., et al. 1976, Sol. Phys., 48, 389

Green, L. M., López fuentes, M. C., Mandrini, C. H., et al. 2002, Sol. Phys., 208, 43

Hagenaar, H. J. 2001, ApJ, 555, 448

Hagenaar, H. J., Schrijver, C. J., Title, A. M., & Shine, R. A. 1999, ApJ, 511, 932

Hartkorn, K. & Wang, H. 2004, Sol. Phys., 225, 311

Harvey, J. 1971, PASP, 83, 539

Hathaway, D. 2004, in COSPAR, Plenary Meeting, Vol. 35, 35th COSPAR Scientific Assembly, 2016–+

Hathaway, D. H., Beck, J. G., Bogart, R. S., et al. 2000, Sol. Phys., 193, 299

Hathaway, D. H., Beck, J. G., Han, S., & Raymond, J. 2002, Sol. Phys., 205, 25

Heyvaerts, J. & Priest, E. R. 1984, A&A, 137, 63

Hirzberger, J., Gizon, L., Solanki, S. K., & Duvall, T. L. 2008, Sol. Phys., 251, 417

Howard, R. A., Michels, D. J., Sheeley, Jr., N. R., & Koomen, M. J. 1982, ApJ, 263, L101

Howard, R. F., Harvey, J. W., & Forgach, S. 1990, Sol. Phys., 130, 295

Hudson, H. S., Acton, L. W., & Freeland, S. L. 1996, ApJ, 470, 629

Hundhausen, A. J. 1993, J. Geophys. Res., 98, 13177

Illing, R. M. E. & Hundhausen, A. J. 1985, J. Geophys. Res., 90, 275

Innes, D., Genetelli, A., Attie, R., & Potts, H. 2008, 12th European Solar Physics Meeting, Freiburg, Germany, held September, 8-12, 2008. Online at ¡A href=”http://espm.kis.uni-freiburg.de/”¿http://espm.kis.uni-freiburg.de/¡/A¿, p.2.86, 12, 2

Innes, D. E., Genetelli, A., Attie, R., & Potts, H. E. 2009, A&A, 495, 319

Innes, D. E., McIntosh, S. W., & Pietarila, A. 2010, A&A, 517, L7+

Jackson, B. V. & Howard, R. A. 1993, Sol. Phys., 148, 359

Jeong, H., Chae, J., & Moon, Y. 2009, Journal of Korean Astronomical Society, 42, 9

Jing, J., Yurchyshyn, V. B., Yang, G., Xu, Y., & Wang, H. 2004, ApJ, 614, 1054

Khan, J. I. & Hudson, H. S. 2000, Geophys. Res. Letters, 27, 1083

Kim, R., Cho, K., Moon, Y., et al. 2005, Journal of Geophysical Research (Space Physics), 110, 11104

Koskinen, H. E. J. & Huttunen, K. E. J. 2006, Space Sci. Rev., 124, 169

Krall, J. 2007, ApJ, 657, 559

Kubo, M., Low, B. C., & Lites, B. W. 2010, ApJ, 712, 1321

LaBonte, B. J., Georgoulis, M. K., & Rust, D. M. 2007, ApJ, 671, 955

Leighton, R. B. 1964, ApJ, 140, 1547

Leighton, R. B., Noyes, R. W., & Simon, G. W. 1962, ApJ, 135, 474

Li, K. J., Gao, P. X., Li, Q. X., Mu, J., & Su, T. W. 2009, Sol. Phys., 257, 149

Lin, H. 1995, ApJ, 446, 421

Lites, B. W., Kubo, M., Socas-Navarro, H., et al. 2008, ApJ, 672, 1237

Livi, S. H. B., Wang, J., & Martin, S. F. 1985, Australian Journal of Physics, 38, 855

Longcope, D., Beveridge, C., Qiu, J., et al. 2007, Sol. Phys., 244, 45

Longcope, D. W. & Welsch, B. T. 2000, ApJ, 545, 1089

Low, B. C. 1996, Sol. Phys., 167, 217

Luoni, M. L., Mandrini, C. H., Dasso, S., van Driel-Gesztelyi, L., & Démoulin, P. 2005, Journal of Atmospheric and Solar-Terrestrial Physics, 67, 1734

Mackay, D. H. & Gaizauskas, V. 2003, Sol. Phys., 216, 121

Mackay, D. H., Priest, E. R., & Lockwood, M. 2002, Sol. Phys., 207, 291

Mackay, D. H. & van Ballegooijen, A. A. 2006, ApJ, 641, 577

MacQueen, R. M. & Fisher, R. R. 1983, Sol. Phys., 89, 89

BIBLIOGRAPHY

Mandrini, C. H., Pohjolainen, S., Dasso, S., et al. 2005, A&A, 434, 725

Martin, S. F., Livi, S. H. B., & Wang, J. 1985, Australian Journal of Physics, 38, 929

Michalek, G. 2009, A&A, 494, 263

Mishra, A. P. & Tripathi, R. 2006, in Proceedings of the ILWS Workshop, ed. N. Gopalswamy & A. Bhattacharyya, 91–+

Moffatt, H. K. 1969, Journal of Fluid Mechanics, 35, 117

Moffatt, H. K. 1976, Fluid Dynamics Transactions, 8, 99

Moffatt, H. K. 1978, Magnetic field generation in electrically conducting fluids, ed. Moffatt, H. K.

Moffatt, H. K. & Proctor, M. R. E. 1982, Geophysical and Astrophysical Fluid Dynamics, 21, 265

Moffatt, H. K. & Ricca, R. L. 1992, Royal Society of London Proceedings Series A, 439, 411

Moffatt, H. K. & Tsinober, A. 1992, Annual Review of Fluid Mechanics, 24, 281

Moon, Y., Chae, J., Wang, H., Choe, G. S., & Park, Y. D. 2002, ApJ, 580, 528

Moon, Y., Cho, K. S., Smith, Z., et al. 2004, ApJ, 615, 1011

Moon, Y., Choe, G. S., Wang, H., Park, Y. D., & Cheng, C. Z. 2003, Journal of Korean Astronomical Society, 36, 61

Moore, R. L., Sterling, A. C., & Suess, S. T. 2007, ApJ, 668, 1221

Nindos, A. & Andrews, M. D. 2004, ApJ, 616, L175

Nindos, A., Zhang, J., & Zhang, H. 2003, ApJ, 594, 1033

Nisenson, P., van Ballegooijen, A. A., de Wijn, A. G., & Sütterlin, P. 2003, ApJ, 587, 458

November, L. J. 1989, ApJ, 344, 494

November, L. J. & Simon, G. W. 1988, ApJ, 333, 427

Pariat, E., Démoulin, P., & Berger, M. A. 2005, A&A, 439, 1191

Park, S., Lee, J., Choe, G., et al. 2010, ArXiv e-prints

Parker, E. N. 1963, ApJ, 138, 552

Parker, E. N. 1975, ApJ, 201, 494

Parker, E. N. 1996, ApJ, 471, 489

Parnell, C. E. 2001, Sol. Phys., 200, 23

Pevtsov, A. A. & Balasubramaniam, K. S. 2003, Advances in Space Research, 32, 1867

Pevtsov, A. A., Canfield, R. C., & Metcalf, T. R. 1995, ApJ, 440, L109

Pevtsov, A. A., Canfield, R. C., Sakurai, T., & Hagino, M. 2008, ApJ, 677, 719

Pevtsov, A. A., Maleev, V. M., & Longcope, D. W. 2003, ApJ, 593, 1217

Phillips, A. D., MacNeice, P. J., & Antiochos, S. K. 2005, ApJ, 624, L129

Potts, H. E., Barrett, R. K., & Diver, D. A. 2003, Sol. Phys., 217, 69

Potts, H. E., Khan, J. I., & Diver, D. A. 2007, Sol. Phys., 245, 55

Priest, E. R. & Forbes, T. G. 1990, Sol. Phys., 126, 319

Priest, E. R., Heyvaerts, J. F., & Title, A. M. 2002, ApJ, 576, 533

Qiu, J., Hu, Q., Howard, T. A., & Yurchyshyn, V. B. 2007, ApJ, 659, 758

Qiu, J. & Yurchyshyn, V. B. 2005, ApJ, 634, L121

Reinard, A. A. & Biesecker, D. A. 2008, ApJ, 674, 576

Rieutord, M. & Rincon, F. 2010, Living Reviews in Solar Physics, 7, 2

Riley, P., Lionello, R., Mikić, Z., & Linker, J. 2008, ApJ, 672, 1221

Romano, P., Contarino, L., & Zuccarello, F. 2003, Sol. Phys., 218, 137

Romano, P., Contarino, L., & Zuccarello, F. 2005, A&A, 433, 683

Romano, P., Zuccarello, F., Poedts, S., Soenen, A., & Zuccarello, F. P. 2009, A&A, 506, 895

Sakurai, T. 1989, Sol. Phys., 121, 347

Sánchez Almeida, J., Márquez, I., Bonet, J. A., Domínguez Cerdeña, I., & Muller, R. 2004, ApJ, 609, L91

Scherrer, P. H., Bogart, R. S., Bush, R. I., et al. 1995, Sol. Phys., 162, 129

Schmieder, B. 2006, Journal of Astrophysics and Astronomy, 27, 139

Schmieder, B., Mandrini, C. H., Démoulin, P., et al. 2006, Advances in Space Research, 37, 1313

Schrijver, C. J., Hagenaar, H. J., & Title, A. M. 1997, ApJ, 475, 328

Seehafer, N. 1990, Sol. Phys., 125, 219

Seehafer, N., Gellert, M., Kuzanyan, K. M., & Pipin, V. V. 2003, Advances in Space Research, 32, 1819

Shine, R. A., Simon, G. W., & Hurlburt, N. E. 2000, Sol. Phys., 193, 313

Simon, G. W., Brandt, P. N., November, L. J., Scharmer, G. B., & Shine, R. A. 1994, in Solar Surface Magnetism, ed. R. J. Rutten & C. J. Schrijver, 261–+

Simon, G. W. & Leighton, R. B. 1964, ApJ, 140, 1120

Simon, G. W., Title, A. M., & Weiss, N. O. 2001a, ApJ, 561, 427

Simon, G. W., Title, A. M., & Weiss, N. O. 2001b, ApJ, 561, 427

Smyrli, A., Zuccarello, F., & Mackay, D. 2011

Smyrli, A., Zuccarello, F., Romano, P., et al. 2010, A&A, 521, A56+

Srivastava, N. 2010, in Magnetic Coupling between the Interior and Atmosphere of the Sun, ed. S. S. Hasan & R. J. Rutten, 308–317

St. Cyr, O. C., Plunkett, S. P., Michels, D. J., et al. 2000, J. Geophys. Res., 105, 18169

Steenbeck, M. & Krause, F. 1966, Zeitschrift Naturforschung Teil A, 21, 1285

Sterling, A. C. & Hudson, H. S. 1997, ApJ, 491, L55+

Tarbell, T. D., Ryutova, M., & Shine, R. 2000, Sol. Phys., 193, 195

Taylor, J. B. 1974, Physical Review Letters, 33, 1139

Temmer, M., Veronig, A. M., Vršnak, B., et al. 2008, ApJ, 673, L95

Thernisien, A., Vourlidas, A., & Howard, R. A. 2009, Sol. Phys., 256, 111

Thompson, B. J., Cliver, E. W., Nitta, N., Delannée, C., & Delaboudinière, J. 2000, Geophys. Res. Letters, 27, 1431

Thompson, B. J., Plunkett, S. P., Gurman, J. B., et al. 1998, Geophys. Res. Letters, 25, 2465

Tian, L., Alexander, D., & Nightingale, R. 2008, ApJ, 684, 747

Tousey, R. 1973, in Space Research, ed. M. J. Rycroft & S. K. Runcorn, 713–730

Trujillo Bueno, J. 2010, in Magnetic Coupling between the Interior and Atmosphere of the Sun, ed. S. S. Hasan & R. J. Rutten, 118–+

Usoskin, I. G. 2008, Living Reviews in Solar Physics, 5, 3

van Driel-Gesztelyi, L. & Culhane, J. L. 2009, Space Sci. Rev., 144, 351

van Driel-Gesztelyi, L., Démoulin, P., Mandrini, C. H., et al. 2002a, in Multi-Wavelength Observations of Coronal Structure and Dynamics, ed. P. C. H. Martens & D. Cauffman, 143–+

van Driel-Gesztelyi, L., Schmieder, B., & Poedts, S. 2002b, in ESA Special Publication, Vol. 477, Solspa 2001, Proceedings of the Second Solar Cycle and Space Weather Euroconference, ed. H. Sawaya-Lacoste, 47–54

Vishniac, E. T. & Brandenburg, A. 1997, ApJ, 475, 263

Vourlidas, A., Buzasi, D., Howard, R. A., & Esfandiari, E. 2002, in ESA Special Publication, Vol. 506, Solar Variability: From Core to Outer Frontiers, ed. A. Wilson, 91–94

Vourlidas, A., Subramanian, P., Dere, K. P., & Howard, R. A. 2000, ApJ, 534, 456

Vršnak, B., Ruždjak, D., Sudar, D., & Gopalswamy, N. 2004, A&A, 423, 717

Wang, H. & Zirin, H. 1988, Sol. Phys., 115, 205

Wang, Y., Nash, A. G., & Sheeley, Jr., N. R. 1989, Science, 245, 712

Webb, D. F., Lepping, R. P., Burlaga, L. F., et al. 2000, J. Geophys. Res., 105, 27251

Wild, J. P. & McCready, L. L. 1950, Australian Journal of Scientific Research A Physical Sciences, 3, 387

Woltjer, L. 1958, Proceedings of the National Academy of Science, 44, 489

Wood, B. E. & Howard, R. A. 2009, ApJ, 702, 901

Yang, S., Büchner, J., & Zhang, H. 2009, ApJ, 695, L25

Yashiro, S., Gopalswamy, N., Michalek, G., et al. 2004, Journal of Geophysical Research (Space Physics), 109, 7105

Yeates, A. R. & Mackay, D. H. 2009, ApJ, 699, 1024

Yurchyshyn, V., Yashiro, S., Abramenko, V., Wang, H., & Gopalswamy, N. 2005, ApJ, 619, 599

Zarro, D. M., Sterling, A. C., Thompson, B. J., Hudson, H. S., & Nitta, N. 1999, ApJ, 520, L139

Zeldovich, Y. B. 1983, Magnetic fields in astrophysics, ed. Zeldovich, Y. B.

Zhang, J., Dere, K. P., Howard, R. A., & Bothmer, V. 2003, ApJ, 582, 520

Zhang, M., Flyer, N., & Low, B. C. 2006, ApJ, 644, 575

Zhao, X. P. & Webb, D. F. 2003, Journal of Geophysical Research (Space Physics), 108, 1234

Zhou, G., Wang, J., & Cao, Z. 2003, A&A, 397, 1057

Zhou, G. P., Wang, J. X., & Zhang, J. 2006, A&A, 445, 1133

Zuccarello, F., Romano, P., Farnik, F., et al. 2009, A&A, 493, 629

Zuccarello, F. P., Soenen, A., Poedts, S., Zuccarello, F., & Jacobs, C. 2008, ApJ, 689, L157

Zwaan, C. 1978, Sol. Phys., 60, 213